



12-2003

# Numerical investigation of a pitching airfoil and resulting flow field effects on a flexible test cell wall

Nicholas Martin Holland

---

## Recommended Citation

Holland, Nicholas Martin, "Numerical investigation of a pitching airfoil and resulting flow field effects on a flexible test cell wall. " Master's Thesis, University of Tennessee, 2003.  
[https://trace.tennessee.edu/utk\\_gradthes/5238](https://trace.tennessee.edu/utk_gradthes/5238)

This Thesis is brought to you for free and open access by the Graduate School at Trace: Tennessee Research and Creative Exchange. It has been accepted for inclusion in Masters Theses by an authorized administrator of Trace: Tennessee Research and Creative Exchange. For more information, please contact [trace@utk.edu](mailto:trace@utk.edu).

To the Graduate Council:

I am submitting herewith a thesis written by Nicholas Martin Holland entitled "Numerical investigation of a pitching airfoil and resulting flow field effects on a flexible test cell wall." I have examined the final electronic copy of this thesis for form and content and recommend that it be accepted in partial fulfillment of the requirements for the degree of Master of Science, with a major in Aerospace Engineering.

Lou Deken, Major Professor

We have read this thesis and recommend its acceptance:

Accepted for the Council:  
Carolyn R. Hodges

Vice Provost and Dean of the Graduate School

(Original signatures are on file with official student records.)

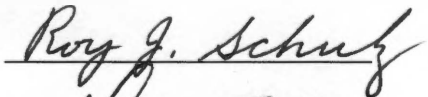

---

To the Graduate Council:

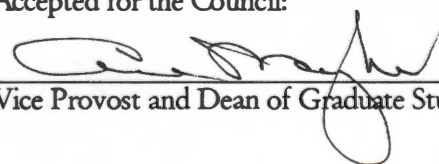
I am submitting herewith a thesis written by Nicholas Martin Holland entitled "Numerical Investigation of a Pitching Airfoil and Resulting Flow Field Effects on a Flexible Test Cell Wall." I have examined the final paper copy of this thesis for form and content and recommend that it be accepted in partial fulfillment of the requirements for the degree of Master of Science, with a major in Aerospace Engineering.

  
Lou Deken, Major Professor

We have read this thesis  
and recommend its acceptance:

Accepted for the Council:

  
Vice Provost and Dean of Graduate Studies

# NUMERICAL INVESTIGATION OF A PITCHING AIRFOIL

---

AND RESULTING FLOW FIELD EFFECTS ON  
A FLEXIBLE TEST CELL WALL

A Thesis

Presented for the  
Master of Science  
Degree

The University of Tennessee, Knoxville

Nicholas Martin Holland

December 2003

Copyright © 2003 by Nicholas Holland  
All rights reserved.

Thesis  
2003  
.H65

## DEDICATION

---

This thesis is dedicated to my grandfather Doctor James Samuel Martin. Papa consistently taught me that my education was the only thing no one could take from me, and encouraged my studies at every opportunity. His principled ways will always remain in my heart.

I would also like to dedicate this thesis to my parents Ron and Betty Holland for giving me the strength to persist when I doubted myself. I can never forget their guidance from my earliest memories until now. They built the foundation of knowledge on which I constructed my higher education. The academic discipline and work ethic I learned in their home provided the necessary ingredients to complete this endeavor.

Each member of my family, as well as my dear friends, has played an important role in my success thus far. I dedicate this thesis to all their contributions, great and small. Thank you all.

Finally, I dedicate this thesis to my wife Kristi Dianne Holland. She has endured countless struggles with me as we worked together to finish our Master's of Science degrees. I thank her for staying by my side through the good and bad, and for her understanding heart. I love you Kristi.

## ACKNOWLEDGEMENTS

---

Lou Deken, Roy Schulz, and Gary Flandro served as committee members. Both Lou Deken and Gary Flandro instructed classes during my Master's program, and all three men proved to have valuable insight during the process of completing this work. Thank you, gentlemen.

Without Russ Groff and Lynn Sebourm I may have never been able to start – much less complete – this work. Russ is an expert on structural finite element analysis, especially ANSYS®. Russ, thank you for answering countless questions. Lynn is a local CFD expert. Lynn, thank you for learning about FLOTRAN® and taking interest in my work. I appreciate you reviewing numerous “colorful” fluid dynamic plots.

Special thanks goes to Tom Tibbals for his experimental data collection and consolidation expertise. He and his team of researchers provided valuable input to this work.

Dawn Goodwin, and her software support team, whose selfless devotion to customers like myself has proved invaluable at times.

I would be amiss if I didn't recognize Ahmad Vakili and Bill Lawrence for their patience and guidance while I learned about wind tunnels and fluid dynamics, both of which relatively new to me in the beginning of this work. They both spent time examining this project and discussing reasonable approaches and expectations.

## ABSTRACT

---

This thesis considers a fluid-structure interaction problem wherein an oscillating airfoil creates pressure gradients along the flexible walls in a wind tunnel test cell. The walls are constructed of a clear acrylic material with relatively low stiffness characteristics, potentially causing adverse effects in the flow field and affecting data collection from instrumentation on the walls and in the flow stream. The objective is to explore effects of varying pressure distributions along the walls using numerical methods for determining the pressure profiles, and to quantify the deflection resulting from this pressure loading. A two-dimensional model of the problem reduces computational difficulties, although the material properties must be adjusted to maintain structural equivalency in two-dimensions. Numerical methods for obtaining both static and dynamic data for structural and fluid problems are explored, and the results are compared to experimental data for validation. Static CFD analyses conducted for fixed airfoil pitch angles are followed by static structural analyses with pressure loads from the CFD solutions. ANSYS® and FLOTRAN® software will be used to perform finite element analyses. This effort does not seek to provide further understanding of unsteady aerodynamic phenomena surrounding an oscillating airfoil, or to study the airfoil's structural response to the fluid dynamics.



## TABLE OF CONTENTS

---

| Chapter   | Page |
|---|------|
| I. INTRODUCTION .....   | 1    |
| II. LITERATURE REVIEW .....                                     | 3    |
| Fluid-structure <b>Interaction</b> .....                        | 3    |
| Wall Interference <b>Correction</b> .....                       | 3    |
| Flexible-Wall Wind Tunnels .....                                | 4    |
| ANSYS® and FLOTRAN® as a General Purpose Software for FSI ..... | 4    |
| Aerodynamics of Oscillating Airfoils .....                      | 4    |
| III. <b>APPROACH</b> .....                                      | 5    |
| Structural Problem Setup and Assumptions .....                  | 5    |
| Determination of Equivalent Stiffness .....                     | 8    |
| Structural Dynamic Equivalency .....                            | 12   |
| Fluid Problem Setup and Assumptions .....                       | 15   |
| FSI Setup and Assumptions .....                                 | 16   |
| IV. RESULTS & DISCUSSION .....                                  | 19   |
| Steady State CFD Analysis .....                                 | 19   |
| Steady State Structural <b>Analysis</b> .....                   | 20   |
| Transient Experimental Analysis .....                           | 21   |
| V. CONCLUSION .....   | 23   |
| Conclusions .....   | 23   |
| Recommendations .....   | 24   |
| LIST OF REFERENCES .....  | 25   |
| APPENDICES .....  | 29   |
| VITA .....  | 85   |

## LIST OF TABLES

---

| Table  | Page |
|--|------|
| Table 1: Mechanical Properties of Acrylite® FF.....  | 6    |
| Table 2. Comparison of Maximum Deflection in a Simply Supported Plate and Beam.....            | 9    |
| Table 3: Nodal Results, Two Mesh Refinements.....  | 10   |
| Table 4: Material Properties of Acrylic for FSI Analysis.....                                  | 12   |
| Table 5. Plate Modal Analysis Frequencies in Hertz.....  | 13   |
| Table 6. <b>Summary</b> of Analysis Success.....   | 19   |
| Table B.1. Density, Viscosity and Kinematic Viscosity of Three Fluids at 14.7psi and 68°F..... | 38   |
| Table B.2. Approximate Turbulence <b>Regions</b> .....   | 38   |
| Table B.3. Shape Functions for FLUID141 DOF.....   | 44   |
| Table B.4. ANSYS® Structural Solvers and Applications.....                                     | 48   |
| Table B.5. Shape Functions for BEAM3 DOF.....  | 50   |
| Table D.1: 0-Degree CFD Results <b>Summary</b> .....   | 67   |
| Table D.2: 4-Degree CFD Results <b>Summary</b> .....   | 67   |
| Table D.3: 8-Degree CFD Results <b>Summary</b> .....   | 68   |
| Table D.4: 12-Degree CFD Results <b>Summary</b> .....  | 68   |
| Table D.5: 16-Degree CFD Results <b>Summary</b> .....  | 69   |
| Table D.6: 20-Degree CFD Results <b>Summary</b> .....  | 69   |
| Table E.1: 0-Degree Reaction Solution.....   | 71   |
| Table E.2: 4-Degree Reaction Solution.....   | 71   |
| Table E.3: 8-Degree Reaction Solution.....   | 71   |
| Table E.4: 12-Degree Reaction Solution.....  | 71   |
| Table E.5: 16-Degree Reaction Solution.....  | 72   |
| Table E.6: 20-Degree Reaction Solution.....  | 72   |
| Table F.1: Experimental Test Conditions.....   | 81   |
| Table F.2: Experimental and Numerical Absolute Pressure Comparison.....                        | 81   |

LIST OF FIGURES

| Figure   | Page |
|--|------|
| Figure 1: Photograph of Test Cell with Airfoil at 0-Degree Pitch .....                   | 6    |
| Figure 2: Depiction of Test Cell and Cross Sections for Stiffness Analysis .....         | 9    |
| Figure 3. Fixed Plate Deflection Constant $\beta$ vs. Ratio $a/b$ .....                  | 9    |
| Figure 4: Section A-A, Nodes with Uniform Load.....                                      | 10   |
| Figure 5: Section A-A, Deformed and Undeformed Shape .....                               | 11   |
| Figure 6: First Nine Fundamental Mode Deflections of Test Cell Wall .....                | 14   |
| Figure 7: First Three Fundamental Mode Deflections of Beam Model.....                    | 14   |
| Figure A.1: Sequentially-Coupled Physics Analysis Procedure for FSI Analysis .....       | 33   |
| Figure B.1: FLUID141 and FLUID142 Fluid/Thermal Elements .....                           | 40   |
| Figure B.2: 2-D, 4-Node Quadrilateral FLUID141 Element.....                              | 44   |
| Figure B.3: BEAM3 Element .....  | 47   |
| Figure B.4: 2-D, 2-node BEAM3 Element .....  | 49   |
| Figure D.1: FLUID141 FEM Around Airfoil at 4 Degrees Pitch.....                          | 57   |
| Figure D.2: FLUID141 FEM Detail Around Airfoil Nose, 4-Degree Pitch.....                 | 58   |
| Figure D.3: 4-Degree, Average Velocity Contours Around Airfoil Nose.....                 | 58   |
| Figure D.4: FLUID141 FEM Detail Near Wall.....   | 59   |
| Figure D.5: 4-Degree, Average Velocity Contours Near Wall.....                           | 59   |
| Figure D.6: 0-Degree, Average Velocity Contours, Max = 2461 in/sec.....                  | 60   |
| Figure D.7: 4-Degree, Average Velocity Contours, Max = 2574 in/sec.....                  | 60   |
| Figure D.8: 8-Degree, Average Velocity Contours, Max = 2997 in/sec.....                  | 61   |
| Figure D.9: 12-Degree, Average Velocity Contours, Max = 3572 in/sec.....                 | 61   |
| Figure D.10: 16-Degree, Average Velocity Contours, Max = 4087 in/sec .....               | 62   |
| Figure D.11: 20-Degree, Average Velocity Contours, Max = 4334 in/sec .....               | 62   |
| Figure D.12: 0-Degree, Relative Pressure, Max = 0.244 psi, Min = -0.114 psi.....         | 63   |
| Figure D.13: 4-Degree, Relative Pressure, Max = 0.245 psi, Min = -0.172 psi.....         | 63   |
| Figure D.14: 8-Degree, Relative Pressure, Max = 0.241 psi, Min = -0.413 psi.....         | 64   |
| Figure D.15: 12-Degree, Relative Pressure, Max = 0.239 psi, Min = -0.746 psi.....        | 64   |
| Figure D.16: 16-Degree, Relative Pressure, Max = 0.241 psi, Min = -1.08 psi.....         | 65   |
| Figure D.17: 20-Degree, Relative Pressure, Max = 0.244 psi, Min = -1.26 psi.....         | 65   |
| Figure D.18: 4-Degree, Relative Pressure Contours Around Airfoil Nose .....              | 66   |
| Figure E.1: Combination Predicted Pressure and Displacement .....                        | 73   |
| Figure E.2: 0-Degree, Wall AA, Predicted Displacement and Pressure vs. Wall Length.....  | 74   |
| Figure E.3: 4-Degree, Wall AA, Predicted Displacement and Pressure vs. Wall Length.....  | 74   |
| Figure E.4: 8-Degree, Wall AA, Predicted Displacement and Pressure vs. Wall Length ..... | 75   |
| Figure E.5: 12-Degree, Wall AA, Predicted Displacement and Pressure vs. Wall Length..... | 75   |
| Figure E.6: 16-Degree, Wall AA, Predicted Displacement and Pressure vs. Wall Length..... | 76   |
| Figure E.7: 20-Degree, Wall AA, Predicted Displacement and Pressure vs. Wall Length..... | 76   |

|  |    |
|--|----|
| Figure E.8: 0-Degree, Wall BB, Predicted Displacement and Pressure vs. Wall Length.....    | 77 |
| Figure E.9: 4-Degree, Wall BB, Predicted Displacement and Pressure vs. Wall Length.....    | 77 |
| Figure E.10: 8-Degree, Wall BB, Predicted Displacement and Pressure vs. Wall Length .....  | 78 |
| Figure E.11: 12-Degree, Wall BB, Predicted Displacement and Pressure vs. Wall Length ..... | 78 |
| Figure E.12: 16-Degree, Wall BB, Predicted Displacement and Pressure vs. Wall Length ..... | 79 |
| Figure E.13: 20-Degree, Wall BB, Predicted Displacement and Pressure vs. Wall Length ..... | 79 |
| Figure F.1: Wall AA, Ps-5, $p_{abs}$ vs. Pitch Angle .....                                 | 82 |
| Figure F.2: Wall AA, Ps-10, $p_{abs}$ vs. Pitch Angle.....                                 | 82 |
| Figure F.3: Wall BB, Ps-5, $p_{abs}$ vs. Pitch Angle.....                                  | 83 |
| Figure F.4: Wall BB, Ps-10, $p_{abs}$ vs. Pitch Angle.....                                 | 83 |
| Figure F.5: Spectral Plot of Static Pressure at Ps-5.....                                  | 84 |
| Figure F.6: Spectral Plot of Static Pressure at Ps-10.....                                 | 84 |

## NOMENCLATURE

---

### VARIABLES

The following nomenclature applies throughout this paper unless otherwise noted locally:

|                     |   |
|---------------------|---|
| $a$                 | speed of sound  |
| $abs$               | denotes absolute value as subscript   |
| $ac$                | denotes acceleration as subscript   |
| $e$                 | denotes element as subscript  |
| $err$               | energy error  |
| $f$                 | frequency   |
| $k$                 | kinetic energy  |
| $n$                 | number of elements  |
| $nd$                | denotes node as subscript   |
| $p$                 | fluid pressure  |
| $pr$                | denotes pressure as subscript   |
| $r$                 | denotes reaction as subscript   |
| $s,t$               | unit directions for elemental shape functions, Tables 2 and 5               |
| $t$                 | time  |
| $u$                 | nodal displacement in X-direction   |
| $u_i$               | nodal displacement vector   |
| $\dot{u}, \ddot{u}$ | nodal displacement derivatives (velocity, acceleration)                     |
| $v$                 | nodal displacement in Y-direction or fluid specific volume (usage dictates) |
| $vol$               | denotes volume as subscript   |
| $w$                 | general point displacement  |
| $A$                 | area  |
| $C$                 | damping coefficient   |
| $C_p$               | constant pressure specific heat   |
| $C_v$               | constant volume specific heat   |
| $D$                 | characteristic diameter   |
| $E$                 | modulus of elasticity   |
| $Err$               | normalized energy error   |
| $F$                 | force   |
| I to P              | node identifiers on elements  |
| $K$                 | stiffness   |
| $L$                 | length  |
| $M$                 | mass  |
| $Ma$                | Mach number   |
| $N$                 | element shape function  |
| $R$                 | gas-specific constant   |
| $Re$                | Reynolds number   |
| $St$                | Strouhal number   |
| $T$                 | fluid temperature   |
| $T_i$               | viscous loss term, $i = x, y, z$  |
| $T_0$               | total, or stagnation, temperature   |
| $U$                 | velocity  |
| $\alpha$            | pitch angle or transient integration parameter (usage dictates)             |
| $\beta$             | coefficient for maximum plate deflection                                    |

|               |  |
|---------------|--|
| $\delta$      | virtual operator or transient integration parameter (usage dictates) |
| $\varepsilon$ | structural strain or fluid dissipation rate (usage dictates)         |
| $\gamma$      | ratio of specific heats  |
| $\mu$         | coefficient of viscosity   |
| $\mu_e$       | effective viscosity  |
| $\mu_t$       | turbulent viscosity  |
| $\nu$         | kinematic viscosity  |
| $\theta_z$    | rotation about Z-axis  |
| $\rho$        | fluid density  |
| $\tau$        | shear stress   |
| $\omega$      | natural frequency  |
| $\xi$         | generic DOF variable   |
| $Y$           | strain energy, or internal work                                      |
| $\zeta$       | external work  |
| $\Psi$        | mode shape   |

#### ABBREVIATIONS AND ACRONYMS

|      |   |
|------|---|
| AIAA | American Institute of Aeronautics and Astronautics                    |
| AHS  | American Helicopter Society   |
| ASCE | American Society of Civil Engineers                                   |
| ASME | American Society of Mechanical Engineers                              |
| CFD  | Computational Fluid Dynamics  |
| DOF  | Degrees of Freedom  |
| ENDS | Turbulence dissipation rate output variable for FLUID141              |
| ENKE | Turbulent kinetic energy output variable for FLUID141                 |
| FEM  | Finite Element Mesh   |
| FFT  | Fast Fourier Transform  |
| FSI  | Fluid-structure Interaction   |
| PRES | Pressure DOF variable, Relative Pressure output variable for FLUID141 |
| RELX | Relaxation Factor   |
| ROTZ | Rotation variable about the Z-axis                                    |
| TEMP | Temperature output variable for FLUID141                              |
| UX   | Displacement variable, X-direction                                    |
| UY   | Displacement variable, Y-direction                                    |
| VX   | Velocity variable, X-direction  |
| VY   | Velocity variable, Y-direction  |

## CHAPTER I

### INTRODUCTION

---

Complex engineering problems are now routinely solved using computational finite element theories. By discretizing a problem with a Finite Element Mesh (FEM), a computer coded with appropriate theoretical formulas and solution algorithms can solve complex problems that in the past involved engineering judgment along with large simplification and assumptions. However, finite element analysis has not removed all assumptions and judgment from these problems. Engineers must now ensure the proper technique, theory, and models are used when performing analysis. Without caution and care, the results can be drastically different from reality.

Both structural and fluid problems can be solved using finite element methods. These problems are commonly solved independently. Structures in a flow field are solved as though they were contained in a vacuum, free from the damping or other effects of the fluid. Fluid flow problems are solved using Computational Fluid Dynamics (CFD) codes and are often assumed to behave independent of the deformations in neighboring structures. Recently, methods have been developed to consider these problems in tandem. This development has been driven by the need to gain insight into the implications of these assumptions and in other instances by problems that fundamentally depend on these interactions. This combined computation is known as a fluid-structure interaction (FSI) problem.

The objective of this work is to explore the effects of varying pressure distributions along the walls of a wind tunnel test cell on resulting wall displacement and vibration. The pressure varies along the walls as a result of a pitching airfoil. As the airfoil oscillates, the blockage in the cell is altered thereby changing the fluid flow regime's characteristics. The proximity of the test article and flow property measurement devices near a tunnel's walls may affect the data collected. If these walls are flexible and have significant motion, the effect may become coupled with the adjoining flow field. The scope of this work is to compare a numerical method for determining the pressure profile along the tunnel walls, and quantify the wall deflection resulting from this pressure loading. The experimental set-up includes tunnel walls constructed of a flexible acrylic material. The tunnel should be modeled in three-dimensions since the airfoil does not travel across the flow field and a significant tip effect is present; however, a two-dimensional model of the problem will be developed to simplify the CFD problem as a starting point. This simplification introduces difficulties into the structural problem since the walls along the length of the test cell are modeled as beam elements that replicate the characteristics of three-dimensional test cell walls. The acrylic properties in the two-dimensional model must be modified until the beam element results simulate three-dimensional plate deflections, both static and dynamic. Aerodynamic theory defines the fluid conditions, and modal analysis defines the vibration characteristics of the test cell walls. ANSYS®, a structural modeling software, and FLOTRAN®, a fluid flow solver, will be used to perform the analyses of the interaction of an airfoil disturbance flow field on the wall of an acrylic wind tunnel model. Methods of obtaining both static and dynamic numerical results are explored, and results are compared to experimental data.

The purpose of this effort is not to provide further understanding of unsteady aerodynamic phenomena surrounding an oscillating airfoil, or to study the airfoil's response to the fluid and the deformed walls. Although some insight may be gained during analysis, results from actual experimentation and other researcher's work on oscillating airfoils will be used to gauge the validity of CFD results in this work.

## CHAPTER II

### LITERATURE REVIEW

---

#### FLUID-STRUCTURE INTERACTION

A review of recent literature from journals like the Journal of Fluids and Structures, Computers and Structures, Journal of Biomechanics, Nuclear Engineering and Design, and numerous other technical journals on finite numerical methods, as well as publications from technical societies like ASME, AIAA, ASCE, AHS, and ASC Structures, revealed many distinctive methods and applications for FSI analysis.

Two general areas of application are structures in fluid and structures containing fluid. Examples of mechanical structures in a fluid include airframes, ships and submarines, breakwaters, buildings, bridges, cables, and submerged drive shafts. Structures containing fluid include pipeline systems and water hammer, blood vessels and the heart, human's inner ear, nuclear reactors, sloshing in storage tanks, and acoustical cavities such as automobiles and aircraft.

Robert Kroyer has studied aerodynamic control surfaces at high Mach numbers in order to determine aeroelastic instability effects in two dimensions [11]. R.J. Zwaan and B.B. Prananta developed a method for fluid-structure application to aircraft in transonic flow, both two- and three-dimensional [21]. Other researchers have developed techniques and for coupling the structure and fluid, meshing alternatives, and theoretical approaches.

Such a wide variety of application has apparently led industry to seek increasingly robust methods for achieving realistic results from simulation. Numerous papers surfaced on the theoretical approaches and computational techniques. Theoretical formulations including Lagrangian-Eulerian, Newtonian, Petrov-Galerkin, Bubnov-Galerkin, and Navier-Stokes methods and equations are among those used to solve fluid-structural problems. Multiple software manufacturers offer commercially available codes that utilize these methods, including ADINA® and ANSYS® [1].

No research directly related to the scope of this thesis surfaced during the literature review; however, papers on the following topics are in some ways related to this study.

#### WALL INTERFERENCE CORRECTION

A well-known drawback to the use of wind tunnels for aerodynamic simulation testing is the affect of wall boundaries on a flow field. This affect varies based on several parameters including the test article blockage ratio and mean fluid velocity [5]. This thesis considers an experiment in which an airfoil oscillates in a wind tunnel, thereby changing the blockage ratio constantly in time. As a result, wall interferences may change in time, too. The scope of the thesis doesn't include making corrections for these interferences, but a literature review was conducted to gain insight from those that have attempted to develop correction factors or formulas.

Joseph Katz and Robert Walters from the San Diego State University studied the effects of large blockages in wind tunnel testing to determine estimations of correction factors when the blockage ratio was as large as twenty percent. They discovered "the changes in aerodynamic coefficients with increasing test-section blockage are gradual and monotonic [9]." Ching-Chyuan Hsing and C. Edward Lan studied this topic at the University of Kansas. By using a thin-layer Navier-Stokes theory in place of the conventional attached flow theory, they developed larger correction factors for



models with strong vortex flow in low-speed flows, Mach 0.3. Their method “shows consistent corrected results for different model sizes,” suggesting the results may be applied to models other than the delta wing used in their experimentation [6]. C.F. Lo also investigated tunnel interference by conducting an analytic assessment of two-dimensional wind-tunnel wall interference. Analytic formulas were derived from solving the Prandtl-Glauert equation for a flow field along two streamwise interfaces in a tunnel [12].

## FLEXIBLE-WALL WIND TUNNELS

In order to minimize the effects of tunnel walls on a model, flexible surfaces in the test cell have been introduced. The acrylic walls of the test cell studied in this thesis are also flexible, but the difference in this tunnel and those discovered in literature review was that deformation in other flexible tunnel walls could be controlled. In one such case, P. Kankainen et al. from the University of Waterloo renovated an open circuit tunnel with an elongated test cell and interchangeable wall and floor surfaces. The flexible wall and floor alter entrance flow quality, and allow models with up to thirty percent blockage to be tested. This concept “provides interference-free data without flow pattern assumptions after a few iterations of the roof and floor shape” according to the authors [8].

## ANSYS® AND FLOTRAN® AS A GENERAL PURPOSE SOFTWARE FOR FSI

The ANSYS® finite element program is capable of evaluating a wide range of fluid-structure problems as shown by P.C. Kohnke and C. Rajakumar [10]. They explored both the pressure-displacement and displacement-displacement approach. Neither of these methods involves a fluid flow. Examples of the pressure-displacement studied by the authors include acoustic pressure distribution in a square room, noise suppression in an automobile cabin, dynamics of a cylindrical shell submerged in water, and an eigenfrequency analysis of a fluid filled cylindrical shell. Examples of the displacement-displacement method include a partially filled spinning tank and an eigenfrequency analysis of a circular canal. The authors found pressure-displacement formulations lead to smaller, albeit unsymmetrical, system matrices. This approach is “more robust in terms of the stability of computed solutions [10].”

Dongwei Shu et al. [15] investigated an application where the fluid was subject to motion. He studied a pipe subjected to axial-symmetric pulse loading, a prelude to “water hammer.” Direct-coupled elements from ANSYS® were used in verification of simplified theoretical models and found ANSYS to have “good agreement” with other models [15]. Other researchers have had similar success using ANSYS® as a tool for fluid-structure interaction as well, thereby affirming the choice of this software code for the oscillating airfoil analysis.

## AERODYNAMICS OF OSCILLATING AIRFOILS

While this thesis includes an oscillating airfoil in two dimensions, the scope does not include an in-depth study of the aerodynamic problem. Experimental work has been performed by Favier et al. [4] in France and by Silcox and Szwarc of the University of Notre Dame [16]. Silcox and Szwarc demonstrated that an NACA 0012 airfoil boundary layer first experiences transition to turbulence and a turbulent wake is formed when an airfoil approaches its stall angle of attack. At the stall angle of attack, a completely turbulent boundary layer formed by the flow remained attached, “indicating that the angle of stall had been affected by [the angular velocity]. This effect was studied at difference conditions of [angular velocity] and in no case did the flow separate from the airfoil [16].” Among their conclusions, Favier et al. also noted the stalling vortex formation on the upper side of a NACA 0012 airfoil depended on the angular velocity [4]. This airfoil is of a kind used for helicopter lift and is similar to the airfoil modeled in this project.

## CHAPTER III

### APPROACH

---

A wind tunnel test cell containing a pitching airfoil will be modeled in a two-dimensional plan view. The airfoil is located directly in the center of a  $42\text{in} \times 14.5\text{in} \times 16\text{in}$  test cell. Inlet velocity is  $2038.4\text{in}/\text{sec}$  at  $0.15Ma$ . The airfoil may be fixed in six pitched positions: 0, 4, 8, 12, 16, and 20 degrees from the centerline of the test cell. The airfoil also may oscillate at these pitch amplitudes up to a maximum frequency,  $f$ , of  $50\text{Hz}$ . Both static and dynamic analyses will be considered. Structural modeling of the tunnel walls will be performed in ANSYS® while FLOTRAN® will be used to perform fluid analyses. These programs work together when performing coupled analyses.

Experimental test data will be collected for all six static airfoil pitch angles at approximately  $0.15Ma$  for use in steady-state CFD validation. Data will also be collected for dynamic pitch oscillations at  $10\text{Hz}$  and 20 degrees amplitude with a free stream velocity of  $2038.4\text{in}/\text{sec}$  for use in validation of dynamic numerical analyses. Static pressure will be recorded at the center of the test section adjacent to the airfoil from Ps-5 at  $L=21\text{in}$ , and 4in behind the airfoil from Ps-10 at  $L=25\text{in}$ , using multiple static pressure ports mounted vertically along one of the walls. Figure 1 shows these positions annotated on a photograph. Total pressure will be recorded with a probe rake from positions immediately behind the airfoil in one-inch increments out to the test cell outlet,  $L=42\text{in}$ .

### STRUCTURAL PROBLEM SETUP AND ASSUMPTIONS

**Airfoil.** The airfoil has a  $4.5\text{in}$  chord, and is symmetrical much like airfoils used for helicopter blades. Although this airfoil is constructed from aluminum and has hollow sections fore and aft, the airfoil will be assumed rigid since airfoil structural deformations or stresses are of no concern in this thesis. The airfoil is anchored to the test cell floor on a pivoting rod directly in the center of the chord. In order to model the airfoil pitch oscillations during dynamic analysis, forced displacement load steps will be input onto the front node of the airfoil model at each time step starting with a zero pitch angle.

**Test Cell Walls.** Flow-induced deformations in test cell walls are the focus of this study. The data collected in this experiment will be used for validation of a fluid-structure interaction simulation code and must be free of all test cell disturbances. Deflections in test cell walls may adversely effect the flow field or data collection from instrumentation located on or near the walls. The pitched, or pitching, airfoil creates transient flow field effects on the walls, and these effects need to be quantified since the walls are flexible. Specifically, how will the pressure along the surface of the walls be altered due to the airfoil position? Tunnel walls are constructed of Acrylite® FF, a clear acrylic material with relatively low stiffness compared to most metals. Mechanical properties of Acrylite® FF are listed in Table 1. The test cell walls act as a plate constrained by heavy flanges on each end of the test cell, and the longitudinal edges are adhered to adjacent top and bottom plates along the length of the test cell. The walls are assumed fixed on the inlet and outlet due to the heavy flanges. Shear deflection is neglected due to the small height-to-length ratio in the beam model. Material properties and real constants are assumed constant throughout the structural model and thermal effects are not considered.

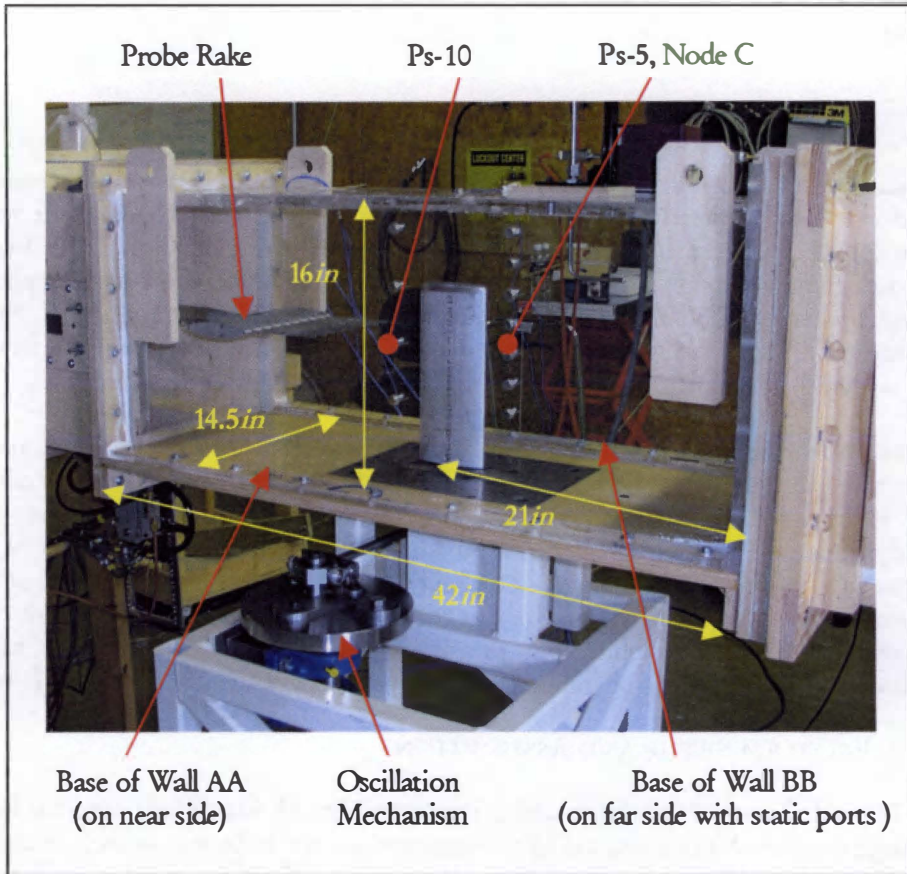


Figure 1: Photograph of Test Cell with Airfoil at 0-Degree Pitch

Table 1: Mechanical Properties of Acrylite® FF

| Property                   | ASTM Method | Typical Value |
|----------------------------|-------------|---------------|
| Specific Gravity           | D 792       | 1.19          |
| Tensile Strength           | D 638       | 10,000psi     |
| Modulus of Elasticity      | D 638       | 400,000psi    |
| Compressive Yield Strength | D 695       | 17,000psi     |
| Rockwell Hardness          | D 785       | M-93          |

(courtesy of CYRO Industries)

The walls will be modeled as beams in a two-dimensional plan view of the test cell, so the properties of this acrylic must be modified so that the beam deflections simulate plate deflections. Either the beam thickness or modulus of elasticity may be adjusted to force the deformation of a beam under static loading to match that of the plate, thus creating static equivalency. The section titled *Determination of Equivalent Stiffness* contains a static analysis of the acrylic walls under a constant distributed pressure loading to predict a modified modulus of elasticity for use in the two-dimensional model.

Dynamic equivalency is important for ensuring vibration characteristics of the simplified two-dimensional structural model responds similarly to the test cell walls. This vibration analysis is contained in a section titled *Structural Dynamic Equivalency* later in this chapter, and is performed using modal analysis. Modal analysis is part of a vibration analysis and is important for diagnosis, design, and control [3]. Essentially, mechanical systems have preferred vibration motions, or mode shapes, at frequencies known as resonance frequencies. When mechanical systems are excited, they vibrate at these resonance frequencies. If the excitation frequency matches a specific resonance, the system will assume its mode shape at that frequency, perhaps yielding destructive results. This analysis concludes with the selection of a modified density for use in two-dimensional beam model. The modified density was set so that the first fundamental frequencies of both the plate and beam would be equal. This simulation assumes the first mode of vibration will dominate the wall response. If later analysis shows an excitation frequency equal to a higher eigenfrequency, the density will be adjusted to account for this higher mode excitation. The same edge constraints were used from the static equivalency analysis for both plate and beam models.

**Structural Analysis.** Test cell walls will be modeled under steady state and dynamic loading in two-dimensions. This two-dimensional approach is highly simplified, but provides a good starting point. Ideally, the problem would be modeled in three-dimensions since the experimental setup contains an airfoil that does not span the entire test cell from floor to ceiling; however, a two-dimensional approach was selected due to computational difficulties previously experienced with FLOTRAN® in a three-dimensional analysis. Distributed differential pressure loading will be applied from the steady-state CFD results to each wall in order to determine static deflections under each airfoil pitch angle. Dynamic analysis may proceed in one of three ways, each more complicated than the previous: single DOF mass-damper-spring system, full dynamic forced response analysis using dynamic CFD pressure results, and sequentially coupled FSI analysis.

A simple, single DOF model of the wall would yield deflections for a given mode of vibration at a fixed point on the wall, i.e. the centerline. Equivalent spring stiffness may be obtained from a static deflection analysis of the two-dimensional wall under a known load. Structural damping will be neglected since it is expected to be negligible. Equivalent mass may be obtained from the equivalent density as determined in Appendix B. This model will require equivalent loading, which may be applied by reducing the fluid dynamic pressure results from a given pitch angle to a resultant point load in terms of any force offset,  $F_0$ , and maximum force,  $F_{max}$ , as a function of time.

$$F(t, \omega) = F_0 + F_{max} \sin(\omega \cdot t) \quad (1)$$

ANSYS® contains computational methods for performing a full dynamic structural analysis when a forcing function is known. This method uses some of the algorithms already discussed in the last chapter for transient analysis and discretization. Again, dynamic pressure results from each pitch angle may be used to establish this forcing function. This approach still lacks coupling of the structural and fluid solutions.

Sequentially coupled FSI analysis is superior to the previous two analysis methods for quantifying the dynamic structural deformation because it does not include the assumption that the fluid problem is unaffected by the structural deformations as discussed in Chapter II.

## DETERMINATION OF EQUIVALENT STIFFNESS

**FEM Development.** The test cell cross-section was modeled full scale in two-dimensions using BEAM3 elements in ANSYS® with a uniform pressure applied to the interior of the test cell. BEAM3 elements are discussed in Appendix B. The uniform pressure results in a balanced load condition, or no reaction forces. Section A-A in Figure 2 depicts the test section as modeled. The maximum displacement of this section, at node C, should equal the maximum displacement of a two-dimensional beam model along section B-B in Figure 2 to ensure static equivalency of the plate wall with a two-dimensional beam model. This approach assumes the center of the plate behaves as a transverse beam from nodes A-C-B, which will be explored momentarily. Changing the material's modulus of elasticity or its thickness will affect the stiffness, and subsequently the displacement. Beam theory will be used in determining the appropriate thickness and/or modulus of elasticity.

To illustrate the validity of the previous assumption, consider a fixed plate (representing the side wall of the test cell) of length  $a = 42in$  and height  $b = 16in$ . The ratio of length to height,  $a/b$ , is 2.625. A uniformly loaded plate with all edges fixed, or constrained against displacement and rotation, with an  $a/b$  ratio of  $\infty$  approaches the behavior of a fixed beam of length  $b$  [13]. The coefficient for maximum plate deflection,  $\beta$ , of a fixed plate approaches 0.0284 as  $a/b$  approaches infinity, whereas the fixed beam has a  $\beta$  of 0.03125. There is some uncertainty associated with the actual behavior of the bonded joints between the walls and the top and bottom plates of the test cell. The error is less than ten percent, and produces a more conservative displacement since it will predict greater influence on the contained fluid. Therefore this error is acceptable for an initial approximation as long as the two-dimensional sections considered are at the centerline of the test cell. Table 2 shows a comparison of the plate and transverse beam deflection behavior. Figure 3 shows the variation of  $\beta$  as  $a/b$  varies from 1.0 to 3.0. Figure 3 plots the ratio  $a/b = 2.625$  concurrent with the  $\beta$  curve.

Two mesh refinements, sixty and ninety nodes per wall, were considered. These nodes were concentrated closer to the wall's corners since the bending will be greater in these regions. Figure 4 shows the ANSYS® plot of the model with a depiction of the pressure loading. In this figure, the uniform pressure, 100psi applied internally on each wall, is depicted to indicate node distribution by placing an arrow at each node location. The modulus was set at 400,000psi as specified by CRYO's material data sheet for Acrylite® FF [2].

The test cell cross-section model, Section A-A, is globally constrained against displacement in the X- and Y-directions at node A, and against global rotation by constraining displacement in the X-direction at node B. Figure 4 contains indications of these constraints as well as the uniform pressure loading. Section A-A assumes full moment capacity available across all bonded joints at the corners of the cross-section.

**Results and Analysis.** Table 3 lists results for three nodes of interest. Nodes A and B are the corner nodes of wall BB from Figure 1, and node C is the center node on this wall. Figure 5 shows the deformed shape.

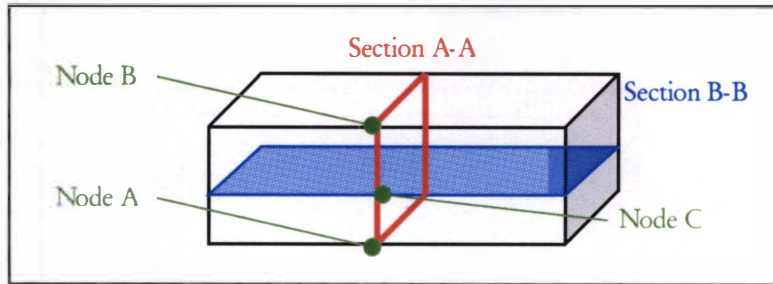

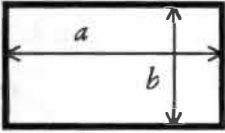


Figure 2: Depiction of Test Cell and Cross Sections for Stiffness Analysis

Table 2. Comparison of Maximum Deflection in a Simply Supported Plate and Beam

| Description                       | Maximum Deflection Under Uniform Load                | Depiction with Notation   |
|-----------------------------------|--|---|
| Beam with Fixed End Constraints   | $\frac{12 \cdot w \cdot b^4}{384 \cdot E \cdot t^3}$ |  |
| Plate with Fixed Edge Constraints | $\beta \cdot \frac{w \cdot b^4}{E \cdot t^3}$        |  |

( $\beta$  is shown in Figure 3 based on  $a/b$  ratio)

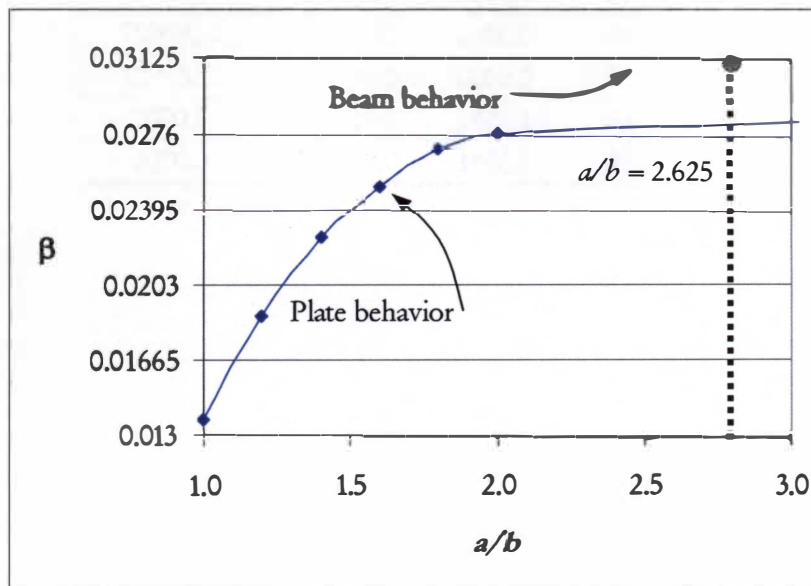


Figure 3. Fixed Plate Deflection Constant  $\beta$  vs. Ratio  $a/b$

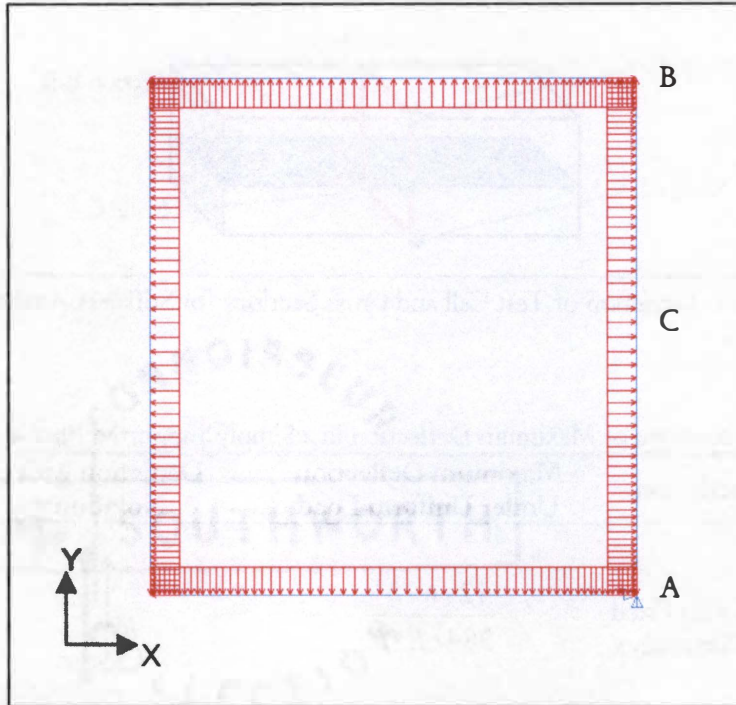


Figure 4: Section A-A, Nodes with Uniform Load

Table 3: Nodal Results, Two Mesh Refinements

| Node | Mesh | UX (in) | UY (in)  | ROTZ (rad) |
|------|------|---------|----------|------------|
| A    | 60   | 0.0000  | 0.0000   | -0.085927  |
|      | 90   | 0.0000  | 0.0000   | -0.085927  |
| B    | 60   | 0.0000  | 0.032222 | 0.085927   |
|      | 90   | 0.0000  | 0.032222 | 0.085927   |
| C    | 60   | 1.3551  | 0.016111 | 0.0000     |
|      | 90   | 1.3551  | 0.016111 | 0.0000     |

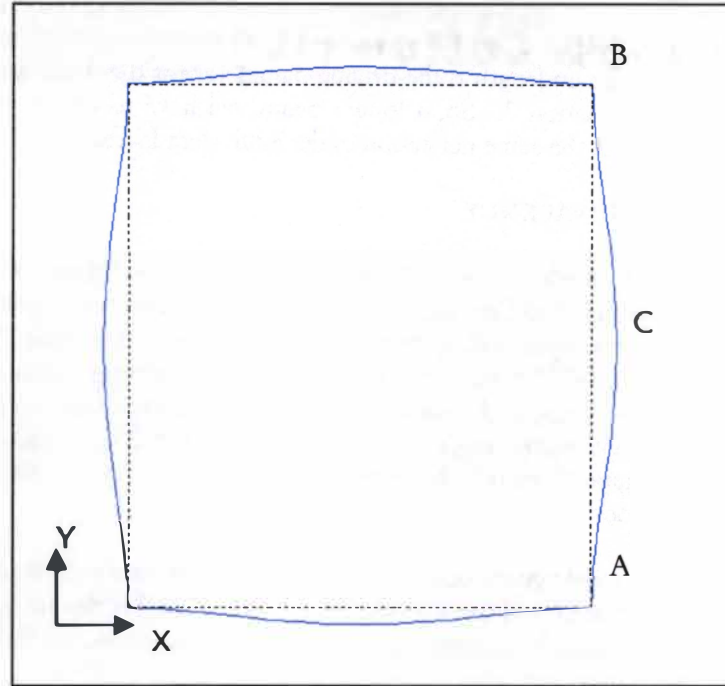


Figure 5: Section A-A, Deformed and Undeformed Shape

Refining the mesh beyond ninety nodes is not beneficial since the same solution with both meshes indicate convergence. Node C, at the centerline, is displaced by  $1.3551in$  in the X-direction. This was the largest X-direction displacement between nodes A and B. Node B slightly deflected in the Y-direction, but since the X-direction displacement is the only direction of interest, Y-direction measurements do not affect the resulting conclusion.

A beam representation of the  $42in$  length along Section B-B is fixed at both ends. Equation 2 yields the maximum displacement of a fixed-fixed beam under a distributed load [13].

$$U_{X \max} = \frac{p \cdot L^4}{384 \cdot E \cdot I_{ZZ}}; \text{ at } X = L/2 \quad (2)$$

Solving equation 2 for the modulus of elasticity,  $E$ , using  $UX = 1.3551in$ ,  $L = 42in$ , a constant  $I_{ZZ}$  based on actual plate thickness, and applying an equivalent distributed pressure load  $p = 100psi$  yields  $E = 17,009,641psi$ .

Another option to ensure static equivalency is to keep  $E$  constant and adjust the thickness,  $t$ , and subsequently the moment of inertia,  $I_{ZZ}$ . This approach yields a thickness of  $2.726in$  and an  $I_{ZZ}$  of  $1.688in^4$ . Increasing the modulus is preferred over altering the geometry since the modulus acts as a scaling factor in deformation formulas. Beam thickness is raised to the third power when calculating the moment of inertia, providing more room for error. Also, altering the beam thickness would complicate stress calculations should they be desired in later analyses. The final stresses, however, will have to be transformed to the original material properties in either case.



Based on these calculations, the appropriate material constants for the two-dimensional model are listed in Table 4. The increased modulus seems reasonable since the length of the test cell's wall is much greater than its height. Beam length is the driving parameter for the deflections because it is raised to the fourth power in equation 2. So, a longer beam will have to be much stiffer than a shorter beam if both are to predict the same deflection under equivalent loads.

## STRUCTURAL DYNAMIC EQUIVALENCY

**FEM Development.** Two modal analyses will be conducted to investigate the modal shapes,  $\Psi$ , and resonance frequencies,  $\omega$ . The first analysis will be of a test cell wall modeled as a three-dimensional panel. The second analysis will be of the two-dimensional beam used to represent the tunnel walls in later analyses. ANSYS® has several options for conducting modal analysis; Block Lanczos, Sub-Space, Power Dynamics, and Reduced methods. The Block Lanczos method is used for linear systems having large symmetric eigenvalue problems [1]. The Block Lanczos method will be used to determine mode shapes for both the plate wall and beam due to its speed and accuracy compared with the other methods.

Modal analysis of an undamped system consists of solving a linear system of equations with two primary parameters, the mass matrix and the stiffness matrix [3]. If  $[M]$  is the mass matrix and  $[K]$  the stiffness matrix, the differential equation for a linear, lumped-mass, undamped system is described by equation 3 [1]:

$$[M] \frac{\partial^2 x}{\partial t^2} + [K]x = f(t) \quad (3)$$

In equation 3,  $x$  is the displacement vector and  $f$  is the force vector. Because the displacement vectors have harmonic motions at specific frequencies, they can be expressed by equation 4:

$$x = \Psi \cos(\omega \cdot t) = \Psi \cdot e^{j \cdot \omega \cdot t} \quad (4)$$

Combining equations 3 and 4 yields an eigenvalue problem in which only certain nontrivial solutions exist for  $\Psi$ . Resulting solutions give the natural frequencies, or eigenfrequencies, and the mode shapes, or eigenvectors. The determinate of the system containing linear homogeneous equations must equal zero, giving the characteristic equation as follows:

$$\det[\omega^2 \cdot [M] - [K]] = 0 \quad (5)$$

Equation 5 has a root for every DOF; therefore a natural frequency exists for every DOF in the system [3].

Table 4: Material Properties of Acrylic for FSI Analysis

| Const.          | Value                    |
|-----------------|--------------------------|
| w               | 1.0 in                   |
| t               | 0.75 in                  |
| A               | 0.75 in <sup>2</sup>     |
| I <sub>zz</sub> | 0.035156 in <sup>4</sup> |
| E               | 17,009,641 psi           |

All systems prefer to vibrate one or more of their mode shapes,  $\Psi$ . These corresponding frequencies,  $\omega_n$ , are referred to as the “natural frequencies.” ANSYS® uses equation 6 to solve for eigenvectors of mode  $i$  [1].

$$[K]\{\Psi_i\} = \omega_i^2 [M]\{\Psi_i\} \quad (6)$$

The wall was modeled as a panel using plate elements having six DOF per node. The leading and trailing edges were restrained in all six degrees since the test cell attached to the tunnel with rigid flanges. The top and bottom edges were constrained in the X, Y, and Z-direction and the Y and Z-rotation since the roof and floor of test cell restrains the walls in those directions. This restraint condition is consistent with the restraints assumed in the two-dimensional beam analysis. The modulus was set to 400,000psi and material density was set to 0.04299lb/in<sup>3</sup> in accordance with CYRO’s material data sheet for Acrylite® FF during the plate wall analysis.

The beam was modeled using beam elements with three DOF per node. The leading and trailing points were restrained in both degrees of freedom. The modulus was set to 17,009,641psi as determined in the previous stiffness analysis. The density will be selected through iterative solutions in order to affect the mass matrix,  $[M]$ , of the approximated beam until the first fundamental frequency of the beam,  $\omega_n$ , matches that of the plate. Higher frequencies of both models are not likely to match. Adjusting the density, and therefore the mass, of the representative material affects only the dynamic response since gravitational effects are ignored in later FSI analysis.

**Results and Analysis.** Nine mode shapes of the plate wall are listed in Table 5. Figure 6 depicts exaggerated wall deflections for these modes. Figure 7 depicts exaggerated beam deflections for the first three modes. By setting the material density of the beam to 0.13640lb/in<sup>3</sup>, the first beam frequency matches that of the plate, 95.92Hz.

For the plate model, sinusoidal waves of increasing frequency form in the X-Z plane as is evident in Figure 6. Higher modes, beginning with the fifth, exhibit displacement waveforms with a period of  $2\pi$  in the Y-Z direction. During these  $2\pi$  periods in the Y-direction the centerline is stationary. Waveform periods increase by  $\pi$ , where  $i$  equals 1, 2, 3...n, first in the X-Z plane, then in the Y-Z plane. When higher periods are reached in the Y-Z plane, the X-Z waveform period returns to  $\pi$  and the cycle continues.

Table 5. Plate Modal Analysis Frequencies in Hertz

| Mode Shape, $\Psi$ | Freq. (Hz) | X-Z Waveform Period | Y-Z Waveform Period |
|--------------------|------------|---------------------|---------------------|
| 1                  | 95.920     | $\pi$               | $\pi$               |
| 2                  | 140.1      | $2\pi$              | $\pi$               |
| 3                  | 211.08     | $3\pi$              | $\pi$               |
| 4                  | 304.43     | $4\pi$              | $\pi$               |
| 5                  | 331.81     | $\pi$               | $2\pi$              |
| 6                  | 372.27     | $2\pi$              | $2\pi$              |
| 7                  | 420.85     | $5\pi$              | $\pi$               |
| 8                  | 438.36     | $3\pi$              | $2\pi$              |
| 9                  | 528.97     | $4\pi$              | $2\pi$              |

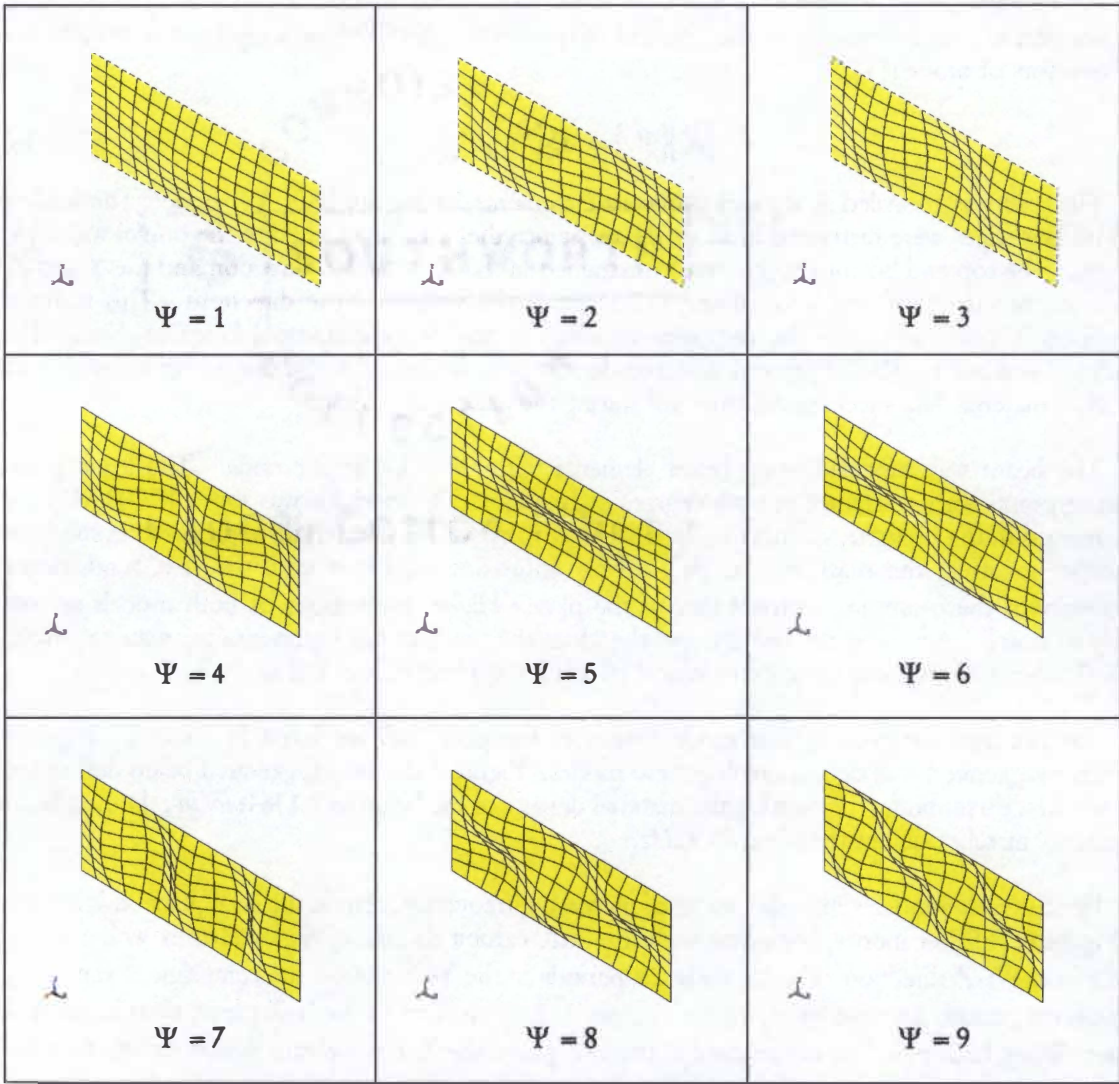


Figure 6: First Nine Fundamental Mode Deflections of Test Cell Wall

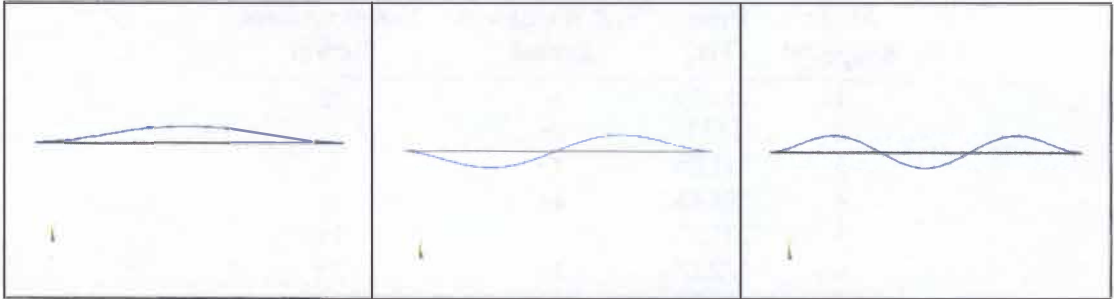


Figure 7: First Three Fundamental Mode Deflections of Beam Model

The beam model shows similar sinusoidal waves forming with increasing frequency. Note how the beam's ends have no slope in Figure 7. The same zero slopes are evident in Figure 6 on the plate walls. The beam mode shapes resemble sinusoids, with the first mode corresponding to waveform period  $\pi$ , the second mode corresponding to period  $2\pi$ , and continuing at  $i\pi$  where  $i$  equals 1,2,3...n. The same shapes are visible on the centerline of the plate in Figure 6, but this similarity erodes beginning with mode shape five when the plate enters its first shape where the centerline is stationary. Any plate mode shape with a Y-Z waveform period having an even multiple of  $\pi$  cannot be matched at the centerline in two dimensions.

The dynamic response of a plate cannot be perfectly modeled with a beam. With this beam approximation, only some mode shapes are similar, and have different frequencies beyond the first. Only one frequency can be matched, and since the plate and beam will prefer to vibrate in the first mode shape due to the pressure distribution, the first eigenfrequency was chosen. The material density of the beam should be  $0.13640 \text{ lb/in}^3$ , or a mass density of  $3.53\text{E-}4 \text{ lbf}\cdot\text{sec}^2/\text{in}^4$ , so that the primary natural frequency of the beam corresponds with the primary natural frequency of the plate. If two-dimensional dynamic analysis is required for excitation at any fundamental frequency other than the first, the beam density should be revised in order to ensure dynamic equivalency at that frequency. The beam calculation will not adequately capture the amplitude of the deflections if a forcing frequency couples with another eigenfrequency from the plate analysis.

## FLUID PROBLEM SETUP AND ASSUMPTIONS

Appendix C contains an input file for the 4-degree pitch angle steady-state CFD analysis, and is typical of the options used for all six steady-state pitch angles. All options, controls, properties, and operating conditions are listed. English units will be used in modeling and analysis, with length in inches, pressure expressed in *psi*, density expressed in  $\text{lbf}\cdot\text{sec}^2/\text{in}^4$ , and viscosity expressed in  $\text{lbf}\cdot\text{sec}/\text{in}^2$ .

**Problem Domain and Boundary Conditions.** The problem domain is limited to a two-dimensional  $42\text{in} \times 14.5\text{in}$  plan view of the test cell as depicted by Section B-B in Figure 2. Limiting the fluid domain to Section B-B assumes the airfoil's tip has no influence in this plane. Inlet and exit conditions of the test cell are known, and limiting the domain to two dimensions reduces computational complexity, time, and resources. The analysis assumes free stream pressure conditions at the outlet by applying a zero relative pressure constraint at the outlet. The reference pressure for the FEM will be set to the static pressure inside the airflow,  $13.9796\text{psi}$ . Using this condition ensures relative pressures calculated by FLOTRAN® are deviations from the free stream static pressure. The inlet flow profile will be assumed fully formed in order to apply boundary conditions. The inlet velocity is set to  $2038.4\text{in}/\text{sec}$  for  $0.15\text{Ma}$  analyses. These boundary conditions and assumptions are annotated in Figure D.1 of Appendix D.

**Flow Regime.** The CFD flow regime is modeled as turbulent, adiabatic, and compressible with air modeled as an ideal gas at  $73.71^\circ\text{F}$  and  $14.2\text{psi}$ , consistent with the experimental test conditions listed in Table F.1 of Appendix F. Specific heat and conductivity will be ignored. These assumptions are consistent with the aerodynamic theories discussed in Chapter II.

**Finite Element Mesh.** In order to ensure the structured mesh was sufficiently dense along the walls and airfoil, the shear boundary layer thickness was calculated for flow along a flat plate using equation B18 of Appendix B. Reynolds number was calculated based on airflow at  $0.3\text{Ma}$ , the highest Mach number experienced inside this tunnel. The resulting thickness came to  $0.116\text{in}$  for the airfoil chord ( $x=4.5\text{in}$ ), and  $0.693\text{in}$  for the test cell walls ( $x=42\text{in}$ ). The airfoil is approximated as a flat plate  $4.5\text{in}$  long and the determination of the airfoil shear boundary layer thickness neglects

acceleration around the airfoil. The airfoil's shear boundary layer thickness,  $0.116in$ , is shown in Figure D.2 of Appendix D. The wall's shear boundary layer thickness,  $0.693in$ , is shown in Figure D.3 of Appendix D. For the airfoil, the shear boundary layer has twenty element with the first node located  $4.01E-3in$  from the surface. For the test cell walls, the shear boundary layer has twelve elements with the first node is located  $3.14E-2in$  from the wall. Nodes in both shear boundary layers are compacted toward the wall. These shear layers are annotated in Figure D.1 of Appendix D.

By constructing the entire mesh of quadrilateral elements versus triangular elements, the most accurate results will be obtained for two-dimensional compressible analyses [1]. Mapped meshing is used wherever possible, but especially around the walls in order to capture wall effects consistently. A tighter mesh was generated in areas where large gradients are expected (around and behind the airfoil). Figure D.1 in Appendix D shows a representative mesh for the problem domain with a 4-degree airfoil pitch angle.

**Analysis Parameters.** Relaxation and stabilization parameters will be used as needed to reach a converged solution. Their use will be limited and on a selective basis as suggested in the ANSYS® documentation [1]. All parameters will be removed before the final solution iterations since the presence of some parameters would otherwise affect the final results.

**CFD Algorithm Controls.** SIMPLEN will be used for fluid DOF coupling to increase the convergence rate. All equations will be solved with semi-direct solvers until prescribed convergence criterion is met, or until a predetermined number of global iterations occur. Preconditioned Conjugate Residual (PCCR) method will be used to solve the pressure equation because of its balance in capability and memory requirements. Preconditioned BiCGStab method (PBCGM) will be used to solve momentum, energy, and turbulence equations since it is recommended by ANSYS® for SIMPLEN coupling. Default settings for each DOF will be used in this problem where possible for relaxation and stabilization parameters.

The standard  $k$ - $\epsilon$  turbulence model is chosen over the zero equation model because it is slightly more robust. Default values from ANSYS were used, as defined by [17]. Other turbulence models are extensions of the standard model, and their use requires specific knowledge about various turbulence parameters.

**Discretization Options.** In transient analyses, the Newmark integration method was chosen over forward difference integration for solving equation A1 of Appendix A because it is more accurate. For advection terms, the compressible pressure and turbulence equations will be solved using the monotone streamline upwind (MSU) approach. Momentum and energy equations will be solved using the SUPG approach for its second order accuracy. These are the SIMPLEN defaults. Weighting functions that drive the diffusion and source term contributions were listed in Table B.5 of Appendix B for FLUID141 elements. No options are available for altering these functions.

The full solution method will be utilized to solve equation A6 of Appendix A since the more restrictive assumptions from both the reduced and mode superposition methods are not desired. A static load step will be solved in this analysis either as a part of the final solution, or to determine initial conditions for the transient analysis.

## FSI SETUP AND ASSUMPTIONS

Either physics environment may be solved first in a sequentially coupled analysis. For this problem, the fluid physics environment will be analyzed first since the transient fluid analysis must start with conditions determined by a steady-state fluid solution. The procedure then follows Figure

A.1 from Appendix A. Time stepping will initially be chosen to allow the airfoil to move one degree between each iteration. The frequency will then be adjusted in subsequent trials until the time step size no longer has a significant effect on the solution.

ANSYS® documentation is not clear on how fluid constraints along a moving boundary are considered. Initially, the velocity will be set to zero along the walls. Once a solution is obtained, fluid velocities along the tip or tail of the foil should nearly equal the velocity of the structural airfoil, which equals  $247.5\text{m/sec}$  for  $f = 50\text{Hz}$ . This calculation assumes pitch angles match equation 7, and that the tip velocity will equal half the chord length multiplied by the maximum angular velocity from equation 8. Corrections to the boundary conditions will be made if this condition is not met.

$$\alpha = \alpha_{\max} \sin(\omega \cdot t) \quad (7)$$

$$\dot{\alpha} = \omega \cdot \alpha_{\max} \cos(\omega \cdot t) \quad (8)$$

## CHAPTER IV

### RESULTS & DISCUSSION

Table 6 contains a list of attempted analyses and the resulting success or failure of each analysis. Steady-state CFD analysis using FLOTRAN<sup>®</sup> was successful. However, steady-state experimental results were not obtained. As a result, steady-state CFD results were not validated with experimental data as planned. Also, dynamic results were not obtained since ANSYS<sup>®</sup> mesh updating would not function. ANSYS7.0<sup>®</sup> would not run the published example problem titled “Example Fluid-Structural Analysis Using Physics Environments [1].” The DAMORPH command, which sets morphing or remeshing options for specific areas or volumes, would not function within ANSYS<sup>®</sup> versions 7.0 or 7.1, the latest ANSYS<sup>®</sup> versions. This problem prevents dynamic analysis from continuing as described in Chapter III, and is attributed to software licensing issues. An alternative approach was taken where necessary.

#### STEADY STATE CFD ANALYSIS

Numerical analysis continued for steady-state conditions as described in Chapter III. The fluid problem was solved at steady-state conditions for airfoil angles at 0, 4, 8, 12, 16, and 20 degrees. Each steady-state CFD solution was evaluated for convergence using the convergence monitors on velocity in the X and Y-directions, relative pressure (PRES), turbulent kinetic energy (ENKE), and turbulent energy dissipation rate (ENDS). In some cases, these monitors oscillated initially and settled to a value lower than preset convergence criterion. Other models required substantially more global iterations to reach a satisfactory solution when the monitors began to oscillate without reaching convergence criterion tolerance values, likely due to turbulent effects. Eventually, all solutions converged, albeit sometimes with the assistance the artificial viscosity stability parameter. All stability parameters were removed before final solution iterations. Convergence monitor values for all monitored variables were compared to the absolute value of the smallest solution value for that variable. If the absolute value of the smallest result was large compared to the monitor’s magnitude, and mass was conserved, the solution was considered converged regardless of monitor value oscillations. This comparison is contained in Tables D.1 through D.6 of Appendix D. When the smallest solution value was zero, as in the case of VX in Tables D.1 and D.2, the magnitude of the monitor was compared to the absolute value of the average solution result for that variable. Mass balance was reviewed for all solutions to ensure mass was conserved. Once the mass flows in and out of the problem domain were essentially equal, the problem was considered converged. The largest difference in mass balance was  $3.E-7 \text{ lbf} \cdot \text{sec} / \text{in}$  compared to a mass flow rate of  $3.14E-3 \text{ lbf} \cdot \text{sec} / \text{in}$  in the 8-degree solution; reference Table D.3 of Appendix D.

Table 6. Summary of Analysis Success

| Attempted Analysis                 | Success? |
|------------------------------------|----------|
| Steady State CFD Analysis          | ☑        |
| Steady State Experimental Analysis | ☒        |
| Transient CFD Analysis             | ☒        |
| Transient Experimental Analysis    | ☑        |
| Steady State Structural Analysis   | ☑        |
| Transient Structural Analysis      | ☒        |
| Structural Experimental Results    | ☒        |

When a satisfactorily converged fluid solution was obtained for each static angle of attack, relative pressure values were recorded along each wall. Contour plots of the average velocity and relative pressure were recorded while maintaining constant contour gradients to ease comparison between plots. Steady-state CFD results are contained in Appendix D. Figure D.5 through Figure D.10 show a gradual progression as the velocity accelerates around the airfoil. The overall maximum velocity is  $4334\text{in/sec}$ , significantly higher than the free stream velocity at  $2038.4\text{in/sec}$ , and occurs near the nose of the airfoil at 20 degrees pitch. The most extreme pressures were also calculated at 20 degrees pitch, as evident in Figure D.17 on the airfoil's leading edge.

## STEADY STATE STRUCTURAL ANALYSIS

Relative pressure CFD results were transformed into differential pressures by adding numerically determined relative pressure results to the tunnel static pressure,  $13.9796\text{psi}$ , which yields an absolute pressure as described prior to equation B10 in Appendix B. The gauge pressure, or differential pressure across the test cell walls, may then be obtained from this calculated absolute pressure and the atmospheric pressure,  $14.202\text{psi}$ , by subtracting the atmospheric pressure from the absolute pressure. In this manner, the differential pressure at zero relative pressure equals  $-0.222\text{psi}$ . The differential pressure was then transferred as distributed surface pressures on an equivalent beam model in ANSYS® in order to solve for the steady-state structural deflection at each pitch angle.

The wall modeled from position (0, 0) to (42, 0) is referred to as wall BB in these results, and the wall modeled from position (0, 14.5) to (42, 14.5) is referred to as wall AA. Figure E.1 includes this nomenclature, as well as a depiction of the distributed pressure loading and resulting exaggerated deformations along the walls for the 4-degree pitch angle. Other deformation solutions appeared essentially the same as shown in Figure E.1. The airfoil oscillates symmetrically about a longitudinal centerline through the plan view; therefore, solutions were only obtained for positive airfoil pitch angles as shown in Figure E.1. Calculating solutions for negative pitch angles would merely produce mirror images. Reaction solutions are tabulated for UX, UY, and ROTZ at both ends of each beam. These results are contained in Appendix E, Tables E.1 through E.6.

Figures E.2 through E.13 plot both the differential pressure profile and resulting wall deflection together. Deflections are plotted in blue with diamond-shaped markers whereas differential pressures are plotted in red with square-shaped markers. Note the two vertical axes used in these figures, one on the left for deflection in inches and another on the right for pressure in pounds per square inch. The scale of each axis is constant in these figures to facilitate comparison between the results. Differential pressures were applied to face 1 of the BEAM 3 elements as depicted in Figure B.3 of Appendix B. Air flows as from location  $0.0\text{in}$  to  $42.0\text{in}$ . Positive differential pressure would indicate a bulging wall effect, or outward force, but all pressures were negative. So, more negative differential pressures indicate greater suction, or inward force. Differential pressure values in each case approach the difference in absolute and atmospheric pressure,  $-0.222\text{psi}$ , at the test cell outlet where a zero relative pressure boundary condition was applied. In Figures E.2 through E.7 for wall AA, negative deflections are toward the airfoil. Wall BB responses in the opposite manner in Figures E.8 through E.13. Refer to Figure E.1 as these conventions follow that figure's layout.

For a zero angle of attack, where the airfoil was aligned with the airflow, symmetric pressures on both sides of the airfoil resulted in a symmetric suction effect on the walls. As the airfoil's angle of attack increased, suction on the wall above the airfoil increased while suction decreased the wall below the airfoil. The largest wall deflections were approximately  $0.003\text{in}$ , calculated for the zero-degree angle of attack, even though the largest local differential pressure magnitude,  $-0.268\text{psi}$ , was calculated for the twenty-degree angle of attack on wall AA, which had a maximum deflection of  $0.00275\text{in}$ . This discrepancy demonstrates how the pressure distribution profile is more important



than local pressure magnitude. Intuitively, a beam would deflect more when a greater load is distributed across the beam, as was the case with the zero-degree case.

The approach described in Chapter III sought to draw conclusions regarding structural deflections resulting from a dynamically pitching oscillation of the airfoil, but such conclusions are not possible without the ability to conduct dynamic numerical computations. The complexity required to couple data between FLOTRAN® and ANSYS® reduced portions of the scope in this analysis to a comparison of steady-state CFD results with dynamic experimental results, and a FFT analysis of experimental static pressure results obtained from two static pressure ports mounted on the wall. A comparison of steady-state CFD results to dynamic experimental results must be preceded with a realization that these results should not theoretically match, especially in the region surrounding the airfoil. A dynamic system contains inertial effects that will not be included in steady-state analyses. The only conditions where this comparison would be valid are in cases of quasi-equilibrium.

Consider the Strouhal number, or reduced frequency, in order to determine what conditions this system must be under for a quasi-equilibrium assumption to be valid. The Strouhal number,  $St$ , is an important indicator of the dynamic nature of turbulent flow as it is an indication of the vortex shedding frequency. The Strouhal number, calculated using equation 9, is a function of  $Re$  for a wide range of characteristic diameters  $D$ , and is essentially 0.2 for  $300 < Re < 300,000$ . At  $Re=760,000$ ,  $St$  is approximately 0.22. For high values of Reynolds number, greater than 400, vortices themselves become turbulent and lose their otherwise regular shape.

$$St = \frac{f \cdot D}{U} \quad (9)$$

The Strouhal number is calculated at two extremes based on experimental test conditions. The minimum extreme is based on the airfoil thickness of 0.9in at 2038in/sec with  $f=10Hz$ , where  $St=0.0044$ . The maximum extreme is based on the airfoil chord length of 4.5in at the same velocity with  $f=50Hz$ , where  $St=0.022$ . Even in the highly conservative maximum extreme case, the Strouhal number is merely half of the predicted value 0.22. A  $St$  lower than the predicted value suggests a shedding frequency less than what is naturally preferred, which is not realistic. For 0.15Ma with  $St=0.22$ , vortices will shed at  $291Hz < f < 498Hz$  for  $1.54in > D > 0.9in$ . These frequencies are much higher than the airfoil oscillation frequencies, suggesting the shedding frequency will nominally follow equation 9 at  $St=0.22$  regardless of the pitching frequency in the experimental range from  $10Hz < f < 50Hz$ . So, the time history of airfoil oscillation should not be evident at a given moment in time within the fluid due to an overwhelming influence from the turbulent flow. A quasi-equilibrium comparison of steady-state numerical data to experimentally recorded dynamic data should therefore be valid.

## TRANSIENT EXPERIMENTAL ANALYSIS

Appendix F contains a comparison of the steady-state absolute pressure magnitudes to those recorded in a FSI experiment. Table F.1 contains experimental test conditions that were subsequently used to determine reference conditions and boundary constraints in the FEM. Table F.2 contains both experimental and numerical results. Experimental static pressures were recorded at two locations on the walls: Ps-5 located adjacent to the airfoil at  $L=21in$  and Ps-10 located 4in further downstream as shown in Figure 1. Comparisons are graphed at both positions on each wall: Ps-5 on wall AA and BB, and Ps-10 on wall AA and BB in Figure F.1 through Figure F.4. Dynamic experimental data was reduced to samples corresponding with five airfoil positions: 0, 4, 8, 12, and 16 degrees. Error was estimated from the scattered sample values at a 0.95 confidence level and plotted

above and below each experimental value. The largest standard deviation of all experimental data points,  $0.00943\text{psi}$ , was for 16 degrees at Ps-10 on wall BB, as shown in Figure F.4 of Appendix F. Standard deviation values at other locations were typically around  $0.006\text{psi}$ . As an aside, a phase shift, or offset, may exist in the pressures recorded at the wall and the angle of the airfoil. This offset was not calculated; however, the relative pressure magnitudes along the wall do not fluctuate greatly from peak-to-peak. For that reason, any error introduced by this crude assumption should be negligible, especially compared to the difference in experimental and numerical results. At each pressure port for the airfoil in all six angles of attack, the experimental static pressures are consistently lower than the predicted steady-state values. The results essentially trend in the same manner, but numerical results were consistently larger than their experimental counterparts. This offset may be attributed to the difference in steady-state numerical assumptions and transient flow conditions in the experiment.

Since the experimental data was recorded at  $9766\text{Hz}$ , sufficient data was available to conduct a Fast Fourier Transform (FFT) in order to reveal dominant frequency components in the pressure loading with approximately  $0.5\text{Hz}$  resolution. Figure F.5 and Figure F.6 in Appendix F contain peak-to-peak FFT plots of static pressure measured in inches of water ( $\text{inH}_2\text{O}$ ) versus frequency ( $f$ ). Inches of water may be converted to pounds per square inch by multiplying by  $0.03613\text{psi}/\text{inH}_2\text{O}$ . Figure F.5 is a FFT of data collected at static pressure port Ps-5, while Figure F.6 contains data collected at static pressure port Ps-10. At Ps-5, pressures impact the wall in scalar multiples of the airfoil oscillation frequency,  $10\text{Hz}$ . The  $10\text{Hz}$  oscillation frequency is dominant at a magnitude of approximately  $0.64\text{inH}_2\text{O}$  or  $0.023\text{psi}$ , and the vibration amplitude drops exponentially through higher frequencies. This peak-to-peak pressure magnitude is small compared to  $13.98\text{psi}$ , the absolute pressure, or  $-0.26\text{psi}$ , the average gauge pressure. Recall how the peak-to-peak values represent the oscillation amplitude about the average gauge pressure, so small values indicate a relatively small influence at the wall. In this experiment, the gauge pressure fluctuated by roughly fourteen percent. Ps-10 shows a different result. The magnitude experienced at the first and third frequencies are significantly lower than at Ps-5, while the magnitude of the second frequency is roughly the same as at Ps-5.

These FFT plots indicate that the walls will not be excited at their first fundamental frequency since the pressure dynamics follow the oscillation frequency of the airfoil. This frequency is substantially lower than the first fundamental frequency determined with modal analysis. The walls should, however, vibrate in a mode shape similar to what was predicted as the first mode shape during modal analysis because the differential pressure on the wall creates constant suction along the length of the walls.

## CHAPTER V

### CONCLUSION

---

#### CONCLUSIONS

This thesis considered a problem wherein a flow field and surrounding structure are interactively coupled. The problem consists of a pitched airfoil mounted inside an open-circuit wind tunnel. The objective was to explore effects of varying pressure distributions along the walls of a test cell, and subsequently quantify test section wall deflections resulting from this loading. Steady-state numerical results were obtained with ANSYS® and FLOTRAN®, the chosen numerical codes, the airfoil at six fixed angles of attack. An experiment was conducted with an oscillating airfoil inside the test cell, and provided dynamic data that allowed for limited comparison with the six steady state CFD solutions. Increasing angles of attack resulted in increasing velocities local to the airfoil's leading edge. The difference between pressure extremes also grew with increasing angle of attack. These results indicate increased wall pressures with increasing angle of attack through twenty degrees, which was anticipated with the NACA 0012 airfoil used in the FSI experiment. Unfortunately, these results could not be validated with experimental data for fixed angles of attack. Collecting experimental data at the same steady-state angles of attack would have verified the numerical approach was correct.

Steady-state differential pressure profiles were and applied on an equivalent beam model as distributed surface pressures in ANSYS®. The beam model was statically equivalent to the acrylic walls. The analysis demonstrated how the pressure distribution profile on the walls is more important than local pressure magnitude since the beam model predicted greater deflection when a greater load is distributed across the beam.

Dynamic experimental data showed that the pressure profile on the walls primarily oscillates at the frequency of airfoil oscillation. Calculations of the Strouhal number indicate that vortices would shed from this airfoil between thirty to fifty times faster than the airfoil is oscillating; however, the oscillation frequency dominates the frequency spectrum in FFT plots. These plots in Appendix F, Figures F.5 and F.6, were constructed from peak-to-peak static pressures; therefore, the oscillation frequency domination may be contributed to larger peak-to-peak pressure values at that frequency regardless of the absolute pressure magnitudes. In other words, while the airfoil is shedding vortices at higher frequencies, the largest pressure differentials are seen at the oscillation frequency.

The tunnel walls should vibrate in their first mode shape as predicted during modal analysis because the differential pressure on the wall creates constant suction along their entire length. Importantly, the determination of the wall's first fundamental frequency, 95.92Hz, yielded a frequency almost ten times higher than the oscillation frequency in the experimental test scenario considered herein, and almost five times higher than the maximum airfoil oscillation frequency, 20Hz. For this reason, the wall vibration magnitude should not be amplified at the first fundamental frequency.

In Chapter IV, a quasi-equilibrium comparison of steady state numerical data to experimentally recorded dynamic data was drawn based on the prediction that the dynamic oscillations of the airfoil would be at quasi-equilibrium in this flow field. The transient experimental data and steady-state numerical solutions did not show agreement as expected following an evaluation of the Strouhal number. The disagreement may be attributed to the difference in steady-state numerical assumptions

and transient flow conditions in this experiment. Experimentation conducted at fixed angles of attack, or transient numerical analysis, would give further insight.

The predicted displacements from this simplified analysis are significantly small compared to magnitudes that would likely cause concern with experimental data collection. Wall vibrations experienced during FSI tests also support this conclusion. Further detailed analysis is not necessary for airflow at this Mach number since the improved accuracy would not produce deflections that would cause concern; however, the following recommendations are suggested for improving the accuracy of this analysis or continuing a more detailed analysis at higher Mach numbers.

## RECOMMENDATIONS

Several activities planned for this effort were not successfully completed. First, steady state experimental results should be collected in order to validate the steady-state CFD results. Unavoidable problems with priority scheduling in a commercial facility prevented such data collection during this effort. This initial validation would provide assurance that FLOTRAN® has been implemented correctly. Mistakes would surely be repeated in dynamic analysis if not caught in steady-state analysis since the former builds on the latter.

Secondly, dynamic analysis of the fluid regime should be conducted in FLOTRAN® to ensure the airfoil will in fact oscillate in the computer model, and to discover how best to perform mesh updating. CFD results obtained from this dynamic analysis could be used to formulate forcing functions for a single DOF mass-spring-damper model or full dynamic structural analysis as described in Chapter III. The single DOF model should have the same static and dynamic response as the wall's first fundamental frequency mode, thereby providing basic frequency response data to compare with experimental FFT data. The full dynamic structural analysis would provide deflections all along the length of the wall instead of at a single point, and would be more desirable since the distributed pressure loading in this problem is highly nonlinear.

Once ANSYS® and FLOTRAN® can be run independently in order to obtain satisfactory solutions, they may be coupled and run together. The final step to complete an original goal of this effort would be to sequentially couple the fluid and structural problem in a FSI analysis. Results from such an analysis could be compared directly with experimental data in order to validate the code. The primary remaining discrepancy between the two-dimensional model and experimental data would be the assumption that the airfoil tip does not influence the flow near the test cell's vertical centerline.

Finally, in order to eliminate error from the previously mentioned assumption of the two-dimensional model, a three-dimensional analysis of the dynamically pitching airfoil should be performed. Three-dimensional modeling in FLOTRAN® is significantly more complicated than two-dimensional, so some of the steps leading up to sequential coupling may need to be repeated for validation again. If significant differences persist in experimental and numerical data, choosing a different turbulence model or different solution algorithms may lead to a more accurate numerical solution. Greater detail must be gathered regarding turbulence in order to utilize one of the more complex  $k$ - $\epsilon$  models.

## LIST OF REFERENCES

---

## LIST OF REFERENCES

---

1. ANSYS7.0 Documentation, SAS IP Inc, 2002.
2. CYRO Industries, <http://www.cyro.com/>
3. de Silva, Clarence W. Vibration Fundamentals and Practice. CRC Press, Boca Ration, 2000.
4. Favier, D., C. Maresca and C. Barbi. "Unsteady Aerodynamics of an Airfoil in Combined Translation/Pitch Oscillations Below and Through Stall." *ALAA/ASME/SLAM/APS 1<sup>st</sup> National Fluid Dynamics Congress*, TA 357, A 127, July 1988, p 785-798.
5. Goethert, B. H. Transonic Wind Tunnel Testing. Pergamon Press, New York, 1961.
6. Hsing, Ching-Chyuan and C. Edward Lan. "Low-Speed Wall Interference Assessment/Correction with Vortex Flow Effect." *Journal of Aircraft*, v 34, n 2, Mar-Apr 1997, p 220-227.
7. Huerta A. and W. K. Liu. "Viscous Flow with Large Free Surface Motion." *Computer Methods in Applied Mechanics and Engineering*, v 69, 1988, p 277-324.
8. Kankainen, P. and E. Brundrett, and J.A. Kaiser. "Small Wind Tunnel Significantly Improved by a Multi-Purpose, Two-Flexible-Wall Test Section." *Journal of Fluids Engineering, Transactions of the ASME*, v 116, n 3, Sept 1994, p 419-423.
9. Katz, Joseph and Robert Walters. "Effects of Large Blockage in Wind-Tunnel Testing." *Journal of Aircraft*, v 32, n 5, Sep-Oct 1995, p 1149-1152.
10. Kohnke, P.C. and C. Rujakumar. "General-Purpose Finite-Element Software for Fluid-Structure Analysis." *International Journal of Computer Applications in Technology*, v 5, n 2-4, 1992, p 199-207.
11. Kroyer, Robert. "FSI Analysis in Supersonic Fluid Flow." *Computers and Structures*, v 81, n 8-11, May 2003, p 755-764.
12. Lo, C.F. "Tunnel Interference Assessment from Measurements on Two Surfaces." *ALAA Journal*, v 28, n 8, Aug 1990, p 1481-1484.
13. Roark, Raymond J. and Warren C. Young. Formulas for Stress and Strain. Fifth Edition. McGraw-Hill, New York, 1975.
14. Russell, Lynn D. and George A. Adebiyi. Classical Thermodynamics. Saunders College Publishing, Fort Worth, 1993.
15. Shu, Dongwei et al. "Investigation of Pressure in a Pipe Subjected to Axial-Symmetric Pulse Loading." *International Journal of Impact Engineering*, v 25, n 6, July 2001, p 523-536.
16. Silcox, Richard J. and Walter J. Szwarc. "Wind Tunnel Dynamic Analysis of an Oscillating Airfoil." *ALAA 10<sup>th</sup> Annual Meeting and Technical Display*, n 74-259, January 1974.
17. Spalding, D. B. and B. E. Launder. "The Numerical Computation of Turbulent Flows." *Computer Methods in Applied Mechanics and Engineering*, v 3, 1974, p 269-289.
18. White, Frank M. Fluid Mechanics. Fourth Edition. WCB/McGraw-Hill, Boston, 1999.
19. Wilcox D. C. Turbulence Modeling for CFD. DCW Industries Publishers, California, 1994.
20. Zienkiewicz, O. C., The Finite Element Method, McGraw-Hill, London, 1977.
21. Zwaan, R.J. and B.B. Prananta. "Fluid/Structure Interaction in Numerical Aeroelastic Simulation." *International Journal of Non-Linear Mechanics*, v 37, n 4-5, June 2002, p 987-1002.

## APPENDICES

---

### COUPLED-FIELD ANALYSIS

Coupled-field analysis refers to the interaction of multiple engineering disciplines where each discipline contains an individually distinct problem. Coupled-field analyses include structural-magneto, thermal-magneto, thermal-stress, thermal-electric, and fluid-structure interactions. Any time the results from one problem provide input to another, the two may be considered “coupled.” ANSYS® contains several methodologies for solving coupled problems. Sequential methods solve each discipline separately, transferring needed information between each problem [1]. Direct methods work for problems when the finite elements are coded with all necessary degrees of freedom (DOF). Direct methods are useful for highly nonlinear problems like piezoelectric, conjugate heat transfer with fluid flow, and circuit-electromagnetic analyses [1]. ANSYS contains special elements for these types of problems.

Two types of sequentially coupled methods are available in ANSYS®: sequentially coupled physics and sequential weak coupling. For FSI, ANSYS® codes solve the structural problem while FLOTRAN® codes solve the CFD problem. Sequentially coupled physics methods solve individual problems one at a time, requiring a relatively large degree of user control and judgment during analysis. Sequential weak coupling is a more automated method that allows for transfer across dissimilar mesh boundaries. Weak coupling requires a great deal preparation before computational routines solve the problem since these decisions are implemented automatically during analysis. In sequentially coupled physics problems, the separate disciplines shall be referred to as distinct physical environments, i.e. a structural physics environment and a fluid physics environment. This physics method is explained further since it is used in this project.

ANSYS® requires five steps to complete a FSI coupled-field analysis [1].

- Setup Fluid and Solid Analysis
- Specify Coupled Solution Options
- Write Physics Environments
- Obtain the Solution
- Post-Processing Results

**Setup Fluid and Solid Analysis.** For all sequential problems, both physical problems are defined within ANSYS®. Structural environments use ANSYS elements, and fluid environment use FLOTRAN® elements in a FSI analysis. Decisions regarding the problem’s dimensionality, physical constants and material properties, and loading and boundary conditions are made during this step. More specific considerations for formulating both of these problems are contained later in this chapter.

**Specify Coupled Solution Options.** Each physical problem has specific options that must be set prior to defining a physics environment. Some of these options are coupled like the problem itself, i.e. a transient analysis will require transient solutions to physical problems. A detailed description of pertinent options is contained in the structural and fluid analysis discussions later.

**Write the Physics Environment.** Each problem’s physics environment contains the following information [1]:

- Finite element types and their settings
- Physical, or real, constants (area, moment of inertia, thickness, etc.)



- Material properties (modulus of elasticity, density, etc.)
- Element coordinate systems (global v. local, Cartesian v. polar, etc.)
- Solution analysis and loading options
- Constraint equations
- Coupled node sets at FSI interfaces
- Boundary conditions

Some of these parameters and options are described in more detail later in this chapter as needed.

**Obtain the Solution.** During sequentially coupled analyses, the results from one physical solution alter parameters in the other solution. Once one problem is satisfactorily solved, information is transferred across physical environments as required. Information is transferred again once the subsequent physical problem is solved. The user must decide which physics problem to solve first. For FSI problems, total pressure is transferred from a FLOTRAN® analysis to become a load in the structural analysis [1]. Structural deformation may be significant enough to require the fluid FEM to be updated.

Mesh updating must occur for coupled-field analysis when significant structural deflections occur in an analysis involving a field domain [1]. Recursive solutions must be obtained until the user is satisfied the overall results have reached convergence. ANSYS® allows for mesh updating of the field domain (fluid, magnetic, or electrostatic) using “morphing” and “remeshing”. Morphing moves nodes to coincide with the deformed structure. For morphing, the original nodes and elements are conserved, but their location or shape changes. Nodes are neither created nor removed. Remeshing removes the previous mesh and replaces it with new nodes and elements that conform to the structural mesh, which is not affected. The solid model, including all geometric entities defining the model, is not affected by either morphing or remeshing [1]. Either option may be selected in ANSYS®, or the program may be allowed to determine which is most appropriate.

Figure A.1 depicts how a sequentially coupled physics analysis generally proceeds in a flow-driven FSI problem [1].

**Post-Processing Results.** Even though ANSYS® completes a solution, a sanity check is required to ensure the solution has converged on a realistic result. Not every problem will reach a converged solution. ANSYS® documentation recommends, “Use your engineering judgment when examining the results to evaluate the plausibility and consistency of the overall analysis approach, how specific properties are used, and the conditions imposed [1].” Information gained from theoretical sources, previous experiments and modal analysis of the specific problem yield insight into what is realistic in the result. Further discussion on post-processing structural and fluid results is contained in later sections of this chapter.

## TRANSIENT THEORY AND ANALYSIS

Problems that are dynamic, or change in time, are known as transient. Transient analysis solution methods employed in ANSYS® and FLOTRAN® for linear second order systems assume initial conditions are known, and that no gyroscopic or Coriolis effects are included. Equation A1 is a dynamic equilibrium equation governing such systems [1].

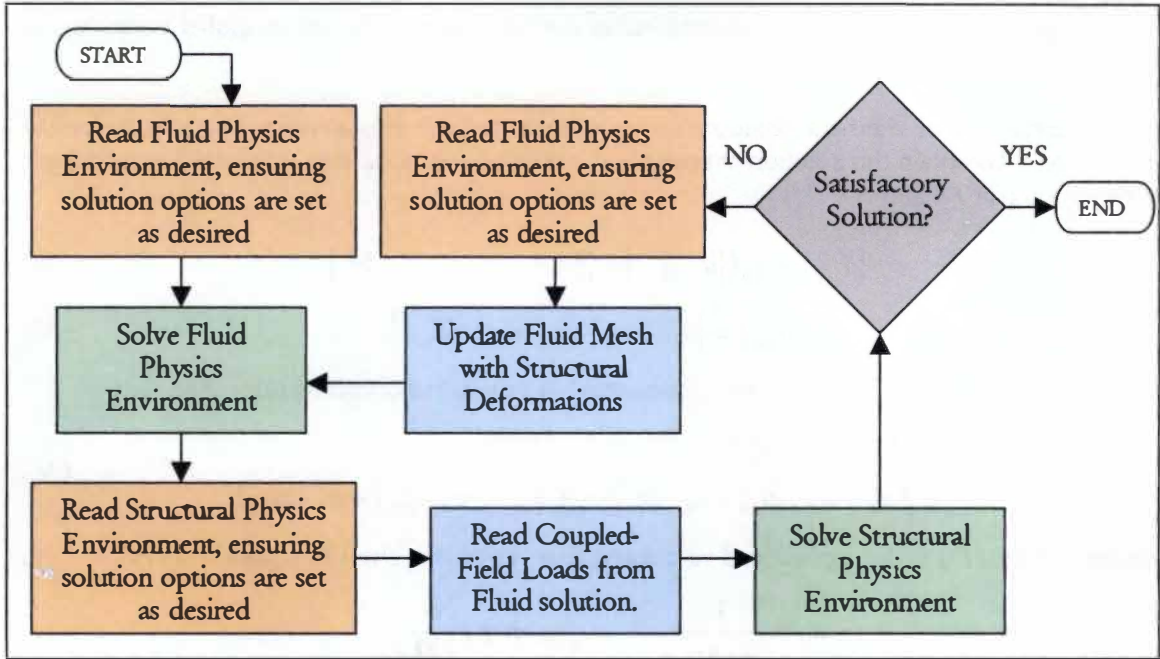


Figure A.1: Sequentially-Coupled Physics Analysis Procedure for FSI Analysis

$$[M] \cdot \{\ddot{u}\} + [C] \cdot \{\dot{u}\} + [K] \cdot \{u\} = \{f\} \quad (A1)$$

In equation A1,  $[M]$  is the mass matrix,  $[C]$  is the damping matrix,  $[K]$  is the stiffness matrix, and  $\{u\}$  is the nodal displacement vector with appropriate derivatives.

ANSYS® contains two methods for solving this equation: forward difference time integration for explicit analyses and Newmark time integration for implicit analyses [1]. The more accurate method is known as the Newmark time integration method. The Newmark method employs finite difference expansions on a time interval  $\Delta t$  until equations A2 and A3 are satisfied.

$$\{\dot{u}_{i+1}\} = \{\dot{u}_i\} + [(1 - \delta)\{\ddot{u}_i\} + \delta \cdot \{\ddot{u}_{i+1}\}]\Delta t \quad (A2)$$

$$\{u_{i+1}\} = \{u_i\} + \{\dot{u}_i\} \cdot \Delta t + [(0.5 - \alpha)\{\ddot{u}_i\} + \alpha \cdot \{\ddot{u}_{i+1}\}]\Delta t^2 \quad (A3)$$

In equations B22 and B23,  $\alpha$  and  $\delta$  are Newmark integration parameters,  $\Delta t$  equals  $t_{i+1} - t_i$ , and  $\{u_i\}$  terms indicate nodal displacement, velocity, or acceleration at time  $t_i$ . Zienkiewicz states that the Newmark solution is unconditionally stable for  $\delta \geq 0.5$ ,  $\alpha \geq 0.25(0.5 + \delta)^2$ , and  $0.5 + \delta + \alpha > 0$ . ANSYS® defaults to values of  $\alpha = 0.25$  and  $\delta = 0.5$  with a small level of numerical damping, as suggested by Zienkiewicz for problems without other sources of damping, by setting an amplitude decay factor to 0.005 [20].

The transient time step  $\Delta t$  is crucial to convergence. ANSYS® will set this time step to the lesser of an advent limit or a pressure wave limit. This option provides the most conservative time step since neither a fluid particle nor pressure waves will propagate through an element in one time step.

In each time step, iterations continue until either the user-defined maximum global iterations, or preset convergence limits are reached.

The initial aim of transient computation is to solve for the displacement  $\{u_{i+1}\}$  in governing equation A1. To obtain this solution at time  $t_{i+1}$ , the previous equation pair A2 and A3 is rearranged into equation pair A4 and A5.

$$\{\ddot{u}_{i+1}\} = a_0(\{u_{i+1}\} - \{u_i\}) - a_2 \cdot \{\dot{u}_i\} - a_3 \cdot \{\ddot{u}_i\} \quad (A4)$$

$$\{\dot{u}_{i+1}\} = \{\dot{u}_i\} + a_6 \cdot \{\dot{u}_i\} + a_7 \cdot \{\ddot{u}_{i+1}\} \quad (A5)$$

Then these equations are combined with equation A1 at time  $t_{i+1}$  to obtain equation A6:

$$\begin{aligned} (a_0 \cdot [M] + a_1 \cdot [C] + [K])\{u_{i+1}\} &= \{F^a\} + \\ [M](a_0 + a_2 \cdot \{\dot{u}_i\} + a_3 \cdot \{\ddot{u}_i\}) &+ [C](a_1 + a_4 \cdot \{\dot{u}_i\} + a_5 \cdot \{\ddot{u}_i\}) \end{aligned} \quad (A6)$$

In equation A6,  $\{F^a\}$  is the applied load vector and  $a_x$  are constants given by equation set A7.

$$\begin{aligned} a_0 &= \frac{1}{\alpha \cdot \Delta t^2} & a_1 &= \frac{\delta}{\alpha \cdot \Delta t} \\ a_2 &= \frac{1}{\alpha \cdot \Delta t} & a_3 &= \frac{1}{2 \cdot \alpha} - 1 \\ a_4 &= \frac{\delta}{\alpha} - 1 & a_5 &= \frac{\Delta t}{2} \left( \frac{\delta}{\alpha} - 2 \right) \\ a_6 &= \Delta t(1 - \delta) & a_7 &= \delta \cdot \Delta t \end{aligned} \quad (A7)$$

ANSYS® contains three transient solution methods: full, reduced, and mode superposition [1]. The full solution method solves equation A6 directly using the Newton-Raphson procedure and Newmark assumptions for a nonlinear analysis, making no additional assumptions. The inversion of equation A6 is performed using Gaussian elimination with the frontal, or wavefront, solver available for solving structural equations. Reduced solution method assumes constant  $[M]$ ,  $[C]$ , and  $[K]$  matrices, constant time steps, no pressure or thermal strains, and limits zero-displacement DOF restrictions. Elemental loads, like pressure, cannot be applied [1]. The mode superposition also makes assumptions in addition to the Newmark assumptions, and uses natural frequencies and mode shapes to predict response to the transient forcing function. Equation A6 requires initial values for the displacement vector and its derivatives, so prior to the transient analysis, either a static load step is solved, conditions are specified, or zero conditions are assumed in the program. Regardless of the approach, the initial transient acceleration is zero. Once a solution for the displacement vector  $\{u_{i+1}\}$  is obtained, the velocities and accelerations are updated using equations A4 and A5.

## CFD FUNDAMENTALS

FLOTRAN® solves flow problems by a CFD modeling approach based on the laws of conservation of mass, momentum, and energy. Each conservation law is a partial differential equation that FLOTRAN® solves on a discrete basis using finite element techniques. The fluid must be single phase and all gases are considered to be ideal gases.

**Continuity Equation.** The law of conservation of mass yields the continuity equation, expressed by equation B1 in vector form [18], [1].

$$\frac{\partial \rho}{\partial t} + \nabla \cdot (\rho \vec{U}) = \frac{1}{R \cdot T_{abs}} \frac{\partial P}{\partial t} + \nabla \cdot (\rho \vec{U}) = 0 \quad (B1)$$

In equation B1,  $\rho$  is the density,  $\vec{U}$  is the velocity vector,  $R$  is the gas constant,  $T_{abs}$  is the absolute temperature, and  $P$  is the pressure. Note that the time derivative of density can be rewritten in terms of the gas constant, absolute temperature, and pressure for ideal gases under isothermal conditions. When density is constant, this equation reduces to the divergence of the velocity vector equal to zero [18].

**Momentum Equation.** The momentum equation for Newtonian fluids is known as the Navier-Stokes equation, expressed by equation B2 in vector form [18].

$$\rho \frac{D\vec{U}}{Dt} = -\nabla P_{abs} + \mu_e \nabla^2 \vec{U} + T_i \quad (B2)$$

Equation B2 ignores gravitational forces, includes viscous loss terms, and excludes terms from a FLOTRAN® option called “distributed resistances” such as flow through a screen. In this equation,  $\mu_e$  is the effective viscosity and  $T_i$  is a viscous loss term. Effective viscosity is defined in the discussion of turbulence, and the pressure gradient is addressed later in this chapter as well. The viscous loss term, relevant only in compressible flows, is defined by equation B3 in two dimensions [1].

$$\begin{aligned} T_x &= \frac{\partial}{\partial x} \left( \mu \frac{\partial U_x}{\partial x} \right) + \frac{\partial}{\partial y} \left( \mu \frac{\partial U_y}{\partial x} \right) \\ T_y &= \frac{\partial}{\partial x} \left( \mu \frac{\partial U_x}{\partial y} \right) + \frac{\partial}{\partial y} \left( \mu \frac{\partial U_y}{\partial y} \right) \end{aligned} \quad (B3)$$

**Energy Equation.** The conservation of energy, equation B4, is in terms of total stagnation temperature in compressible flows and static temperature in incompressible flows [18].

$$\frac{\partial}{\partial t} (\rho \cdot C_p \cdot T_0) + P_{abs} (\nabla \cdot \vec{U}) = \nabla \cdot (K \cdot \nabla T_0) + W^v + E^k + Q_v + \Phi + \frac{\partial P_{abs}}{\partial t} \quad (B4)$$

Equation B4 is valid for compressible flows, with  $T_0$  is the total, or stagnation, temperature,  $K$  is the thermal conductivity,  $W^v$  is a viscous work term,  $Q_v$  is a volumetric heat source,  $\Phi$  is a viscous heat

generation term, and  $E^k$  is the kinetic energy. For adiabatic problems in FLOTRAN®, the static temperature,  $T$ , is calculated from the total temperature using equation B5 [1].

$$T = T_0 - \frac{U^2}{2 \cdot C_p} = T \left( 1 + \frac{\gamma - 1}{2} Ma^2 \right) \quad (B5)$$

**Turbulence.** In turbulent flow, the instantaneous velocity fluctuates at all points in the flow field. The velocity can be expressed by equation B6 in terms of a mean value and a dynamic value [1].

$$U_i = \bar{U}_i + U'_i \quad (B6)$$

In equation B6,  $\bar{U}_i$  is the mean component of velocity in the  $i$  direction, and  $U'_i$  is the dynamic component. Substituting this value for velocity into the Navier-Stokes equation B2 and time averaging the equation, extra terms result in the momentum equation. These extra terms are known as turbulent stresses, and are defined in equation B7 [1]:

$$\begin{aligned} \sigma_x^R &= -\frac{\partial}{\partial x} (\overline{\rho \cdot U'_x \cdot U'_x}) - \frac{\partial}{\partial y} (\overline{\rho \cdot U'_x \cdot U'_y}) - \frac{\partial}{\partial z} (\overline{\rho \cdot U'_x \cdot U'_z}) \\ \sigma_y^R &= -\frac{\partial}{\partial i} (\overline{\rho \cdot U'_y \cdot U'_x}) - \frac{\partial}{\partial y} (\overline{\rho \cdot U'_y \cdot U'_y}) - \frac{\partial}{\partial z} (\overline{\rho \cdot U'_y \cdot U'_z}) \\ \sigma_z^R &= -\frac{\partial}{\partial i} (\overline{\rho \cdot U'_z \cdot U'_x}) - \frac{\partial}{\partial y} (\overline{\rho \cdot U'_z \cdot U'_y}) - \frac{\partial}{\partial z} (\overline{\rho \cdot U'_z \cdot U'_z}) \end{aligned} \quad (B7)$$

The effective viscosity is defined by the sum of the laminar viscosity  $\mu$  and the turbulent viscosity  $\mu_t$ , which depends on the turbulence model chosen. Since this term has the same form as the viscous force terms in equation B2, the effective viscosity term is defined equation B8 in two-dimensional Cartesian coordinates [1]:

$$\mu_e \nabla^2 \vec{U} = \frac{\partial}{\partial x} \left[ \mu \frac{\partial \bar{U}}{\partial x} - (\overline{\rho \cdot U'_x \cdot U'_x}) \right] + \frac{\partial}{\partial y} \left[ \mu \frac{\partial \bar{U}}{\partial y} - (\overline{\rho \cdot U'_x \cdot U'_y}) \right] \quad (B8)$$

FLOTRAN® contains six turbulence models [1]:

- Standard  $k$ - $\varepsilon$  Model
- Zero Equation Model
- Re-Normalized Group Model, or RNG
- New  $k$ - $\varepsilon$  Model due to Shih, or NKE
- Model due to Girimaji, or GIR
- Shi, Zhu, Lumley Model, or SZL

In the Zero Equation Model, the  $\mu_t$  calculation depends heavily on the mesh density near walls, and is the simplest model in FLOTRAN® [1]. In all other models,  $\mu_t$  is a function of turbulent kinetic energy  $k$  and turbulent dissipation rate  $\varepsilon$ . The standard  $k$  -  $\varepsilon$  model requires the solution of two additional equations, one for the transport of kinetic energy and one for the transport of dissipation. Equation B9 relates turbulent kinetic energy and the turbulent dissipation rate [19]. Spalding and Launder have composed a detailed discussion on this model, and their default values for  $k$  and  $\varepsilon$  are

used in ANSYS® [17]. The remaining four turbulence models are extensions of the standard  $k - \varepsilon$  model with changes in viscosity terms or in the source term of the dissipation equation.

$$\mu_t = 0.09 \cdot \rho \frac{k^2}{\varepsilon} \quad (\text{B9})$$

**Pressure.** FLOTRAN® algorithms solve for relative pressure rather than absolute pressure in order to improve numerical accuracy. Neglecting gravitational effects, the absolute pressure  $p_{abs}$  is the sum of the reference pressure  $p_{ref}$  and relative pressure  $p_{rel}$  in a stationary coordinate system [1].  $p_{ref}$  is defined globally for the problem, and usually equals the atmospheric pressure such that  $p_{rel}$  equals the gauge pressure. If  $p_{ref}$  is set to the free stream static pressure,  $p_\infty$ , then  $p_{rel}$  is the deviation from  $p_\infty$ . Gauge pressure, or differential pressure, is calculated by subtracting  $p_{abs}$  from the atmospheric pressure in such cases. The momentum equation can be rewritten as equation B 10 in vector form for a stationary coordinate system.

$$\rho \frac{D\vec{U}}{Dt} = -\nabla p_{rel} - \mu \nabla^2 \vec{U} + T_i \quad (\text{B10})$$

FLOTRAN® calculates the total, or stagnation, pressure based on equation B 11 for compressible problems [1].

$$p_{total} = (p_{rel} + p_{ref}) \left( 1 + \frac{\gamma - 1}{2} \cdot Ma^2 \right)^{\frac{\gamma}{\gamma - 1}} - p_{ref} \quad (\text{B11})$$

## FLOTRAN® ANALYSIS

Typically, FLOTRAN® analysis consists of seven steps [1].

- Determine the problem domain
- Determine the flow regime
- Create the finite element mesh
- Apply boundary conditions
- Set FLOTRAN® analysis parameters
- Execute solution algorithms
- Post-Processing Results

**Determine the Problem Domain.** When determining the problem's domain, choosing boundaries where conditions are known is an important consideration. Locating the boundaries near regions of steep gradients in solution variables should be avoided [1]. If the results show steep gradients in solution variables, the domain boundaries must be moved and the problem should be reanalyzed. These domain boundaries are defined by boundary conditions applied as load constraints.

**Determine the Flow Regime.** Fluid properties, physical geometry, and the velocity and pressure fields characterize the flow regime [1]. FLOTRAN® can analyze several types of flow regimes, and they are not mutually exclusive (i.e. a turbulent analysis can be compressible or incompressible). Each of these analyses types must be considered in order to define the flow regime. A FLOTRAN® analyses can be [1]:

- Laminar or turbulent
- Thermal or adiabatic
- Compressible or in-compressible
- Newtonian or non-Newtonian

- Include multiple species transport

Laminar or Turbulent. When considering the viscous behavior of Newtonian fluids, the primary parameter of consideration is the dimensionless Reynolds number defined by equation B12.

$$Re = \frac{\rho \cdot U \cdot D}{\mu} = \frac{U \cdot D}{\nu} \quad (B12)$$

In equation B12,  $\rho$  is the fluid density,  $\mu$  is the coefficient of viscosity,  $\nu$  is the kinematic viscosity, and  $U$  and  $D$  are characteristic velocity and length, respectively [18].  $Re$  was named after Osborne Reynolds, a British engineer who proposed it in 1883 [18]. Table B.3 shows viscosity, density, kinematic viscosity at standard temperature (68°F) and pressure (14.7 $psi$ ) for several fluids for comparison.

Recall turbulent flow occurs in a flow with high Reynolds number. “Low” and “high” are relative terms and vary depending on flow geometry. White suggests representative ranges for approximating turbulent transitions as listed in Table B.4 [18]. The ranges listed in the table are for flow in ducts, and vary somewhat with geometry, surface roughness, and inlet stream conditions. For example, airflow at standard temperature and pressure moving at 0.15 $Ma$  through a 14.5 $in$  duct has a Reynolds number equal to 1.26E6, well beyond the transition region.

Table B.1. Properties of Three Fluids at 14.7 $psi$  and 68°F

| Fluid    | $\rho$ , lb/in <sup>3</sup> | $\mu$ , (lbf·s)/in <sup>2</sup> | $\nu$ , in <sup>2</sup> /s |
|----------|-----------------------------|---------------------------------|----------------------------|
| Hydrogen | 3.03E-6                     | 1.28E-9                         | 1.63E-1                    |
| Air      | 4.34E-5                     | 2.61E-9                         | 2.34E-2                    |
| Water    | 3.61E-2                     | 1.45E-7                         | 1.57E-3                    |

Table B.2. Approximate Turbulence Regions

| Region                                   | Description                              |
|--|--|
| 0 < $Re$ < 1                             | highly viscous laminar “creeping” motion |
| 1 < $Re$ < 100                           | laminar, strong $Re$ dependence          |
| 100 < $Re$ < 10 <sup>3</sup>             | laminar, boundary-layer theory used      |
| 10 <sup>3</sup> < $Re$ < 10 <sup>4</sup> | transition to turbulence                 |
| 10 <sup>4</sup> < $Re$ < 10 <sup>6</sup> | turbulent, moderate $Re$ dependence      |
| 10 <sup>6</sup> < $Re$ < $\infty$        | turbulent, slight $Re$ dependence        |

Thermal or Adiabatic FLOTRAN® restricts analysis of gases to only ideal gases which obey equation (27).

$$p \cdot v = R \cdot T \quad (\text{B13})$$

In equation B13,  $p$  is the fluid pressure,  $v$  is the fluid specific volume,  $R$  is the gas-specific constant, and  $T$  is the fluid temperature [14]. Air's gas-specific constant equals  $0.287 \text{ kJ}/(\text{kg} \cdot \text{K})$ , or  $18544.2 (\text{lb} \cdot \text{ft} \cdot \text{in})/(\text{lbmol} \cdot ^\circ\text{R})$ . If the temperature is assumed to be constant, a special case of equation B13 known as Boyle's Law, equation B14, relates pressure and specific volume [14].

$$p_1 \cdot v_1 = p_2 \cdot v_2 = p \cdot v = \text{constant} \quad (\text{B14})$$

Compressible or Incompressible Compressibility of fluid flow is primarily a function of the Mach number  $Ma$ . This number is named after Austrian physicist Ernst Mach [18].  $Ma$  is a ratio of a flow's velocity  $U$  to the speed of sound  $a$  in that fluid, as expressed in equation B15.

$$Ma = \frac{U}{a} \quad (\text{B15})$$

In FLOTRAN®,  $Ma$  for an ideal gas is calculated with equation B16 as a function of the velocity magnitude, the ratio of specific heats  $\gamma$ , the ideal gas constant  $R$ , and the absolute temperature  $T_{abs}$  [1].

$$Ma = \frac{|U|}{(\gamma \cdot R \cdot T_{abs})^{0.5}} \quad (\text{B16})$$

Newtonian or non-Newtonian In 1687, Sir Isaac Newton postulated a linear resistance law for fluids in shear. Fluids that follow his law are now known as Newtonian fluids. Common fluids such as air, water, and light oils behave as Newtonian fluids. When a Newtonian fluid is sheared, the shear stress,  $\tau$ , is linearly proportional to the coefficient of viscosity,  $\mu$ . Equation B17 defines Newtonian fluids [18].

$$\tau = \mu \frac{d\theta}{dt} = \mu \frac{du}{dy} \quad (\text{B17})$$

Multiple Species Transport Multiple species transport is useful for calculating dispersion of dilute contaminants or pollutants in fluid flow. It can also be used in applications like heat exchangers where two or more fluids are involved.

**Create the Finite Element Mesh.** Before any finite element geometry is meshed, an element must be chosen. FLOTRAN® has two types of elements compatible across physics environments: a two-dimensional element called FLUID141, and a three-dimensional element called FLUID142 [1]. FLUID141 can be a four-node quadrilateral or three-node triangle [1]. FLUID142 can be a four-node tetrahedral or an eight-node hexahedral [1]. These elements are depicted in the Figure B.1.

Both FLOTRAN® elements have six DOF per node. These DOF include fluid velocity, pressure, temperature, turbulent kinetic energy, turbulent energy dissipation, and multiple species mass fractions for up to six fluids [1].



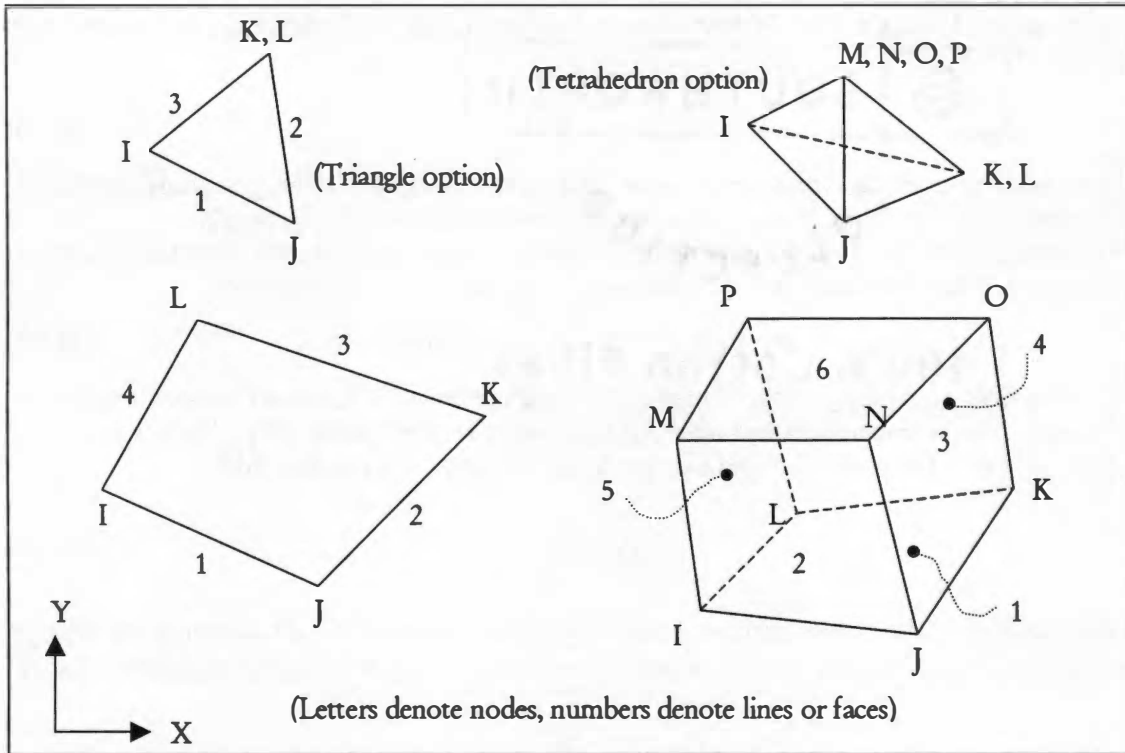


Figure B.1: FLUID141 and FLUID142 Fluid/Thermal Elements

ANSYS® will mesh geometries with automated mesh routines. Resulting meshes may be structured or freely mapped. Free meshing allows the program to generate nodes that grow to fill a space; however, the mesh must be sufficiently refined along regions of steep gradients [1]. These regions are near structural surfaces and behind obstructions such as an airfoil. If the mesh is too coarse in these regions, it will likely not capture significant effects like turbulent vortices. Along structural surfaces like an airfoil, FLOTRAN® is tolerant of large aspect ratios with the elongated side along directions of very low gradients; therefore, the structured meshing option is more appropriate than an unstructured approach. The boundary layer region of the airfoil requires densely packed nodes normal to the surface, but does not require as many nodes parallel to the surface. A structured mesh has regular node intervals defined by the program's user, so they may be more densely packed in one direction over another. Unlike structural elements, large aspect ratios in fluid elements do not adversely affect the solution if the elongated side of the element is in a direction with low gradients [1].

**Apply Boundary Conditions.** Along solid surfaces, such as walls, viscous fluid velocities are characteristically set to zero relative to the wall, known as the no-slip condition. A boundary layer, or shear layer, forms between the wall and regions of nearly inviscid flow. A highly refined FEM should be created to capture these shear layers in order to resolve the resulting velocity profiles [1]. Equation B18 expresses an experimental boundary layer thickness function for  $\delta$  at a length  $x$  along a flat plate [18].

$$\delta = 0.37 \cdot x \cdot \text{Re}_x^{-1/5} \quad (\text{B18})$$

Any known DOF quantity may be specified at a FEM boundary. A zero gradient normal to the boundary is applied for every unspecified DOF [1]. For subsonic flow,  $Ma$  less than 1.0, the inlet boundary condition should be specified using velocity or pressure, and the outlet boundary condition should be specified using pressure [1].

**Set FLOTRAN® Analysis Parameters.** Reference conditions within FLOTRAN® include the reference pressure, bulk modulus, specific heat ratio, reference temperatures, and gravity [1]. Fluid properties may be set for density, viscosity, conductivity, and specific heat, all of which may vary during the analysis. Other important analysis options may be considered, including relaxation and stabilization parameters and transient analysis parameters [1].

Relaxation and Stabilization. Relaxation and stabilization parameters may be adjusted, and DOF properties may be capped during the solution process in order to more quickly reach convergence in complex problems. ANSYS® documentation contains recommendations for adjusting these parameters to bring complicated problems to convergence [1].

Relaxation factors adjust how much of the newly calculated solution is considered when adjusting the previous iteration solution. These factors affect advection algorithm schemes as part of equation discretization discussed later in this chapter. Equation B19 demonstrates how the relaxation factor  $RELX$  is applied to a solution variable,  $\xi$ . The relaxation factors for every component must be between 0.0 and 1.0 [1].

$$\xi_{new} = (1 - RELX)\xi_{previous} + RELX \cdot \xi_{calculated} \quad (B19)$$

Stability controls increase diagonal dominance of an equation during inertial relaxation, thus making the matrix equation easier to solve; however, more iterations are required to reach convergence when inertial relaxation is used [1]. Inertial relaxation may be applied to the momentum, temperature, pressure, and turbulence equations [1]. One important stabilization parameter is artificial viscosity, which is added to the main diagonal and forcing function of the momentum equations [1]. Compressible fluid problems with high velocity gradients are more easily solved with artificial viscosity, but it must be gradually removed since its presence will affect the final solution. Convergence also takes longer to achieve with stability controls activated, although in some problems convergence may never be achieved without these controls.

By capping the maximum or minimum value for a troublesome variable, the variable will not be allowed to reach values that otherwise lead to stalling, divergence, or unrealistic properties like negative density. The velocity, pressure, and temperature DOF may be capped [1].

Convergence Monitors. Convergence monitors provide a normalized measure of a solution's rate of change between iterations. Changes of each monitored DOF variable are calculated from the absolute difference of the results between the current iteration  $i$  and the previous iteration ( $i-1$ ), divided by the sum of the current values. The summation is performed over all  $n$  nodes. Velocity, pressure, kinetic energy, and kinetic energy dissipation rate may be monitored [1]. Equation B20 shows the formulation that takes place during every iteration for each monitored DOF variable.

$$ConvergenceMonitor = \frac{\sum_{m=1}^n |\xi_m^i - \xi_m^{(i-1)}|}{\sum_{m=1}^n |\xi_m^i|} \quad (B20)$$

The fluid solution may have converged once these normalized monitors have settled to a constant value, but convergence is not guaranteed since fluid problems are nonlinear [1]. The magnitudes of converged monitor values depend on the geometry, FEM, turbulence severity, and flow development near the outlet boundaries [1]. Comparison of the average, maximum, and minimum values for each monitored DOF with the magnitude of the convergence monitor provides more meaning to the resulting monitor magnitudes. For example, monitor magnitudes on the same order of magnitude as the minimum DOF result indicate changes in the solution variables are substantial compared to the results.

**Execute Solution Algorithms.** The laws of conservation of mass, momentum, and energy define fluid problems. These laws are expressed in terms of partial differential equations, and discretized using finite elements. For these equations to be valid, the fluid must be Newtonian, consist of a single phase, and the problem domain must be constant [1]. Conservation equations are used for viscous fluid flow and energy in fluid regions. Velocities are obtained from the conservation of momentum while pressures are obtained from the conservation of mass principle. Temperature is obtained from the law of conservation of energy.

**CFD Solution Algorithms.** When FLOTRAN® executes a global iteration, approximate solutions are obtained from the momentum equation and used as forcing functions to solve the pressure equation while conserving mass. These pressures are used in turn to update velocities until the velocity field conserves mass. Temperature and temperature-dependent variables are then updated if desired. Once these fundamental equations are solved, turbulence equations are addressed and the effective viscosity and thermal conductivity are calculated from the turbulent kinetic energy and dissipation rate. These revised properties replace laminar viscosity and thermal conductivity in the model to impart turbulence on the flow. All of these calculations occur in each global iteration in a process summarized below [1].

1. Formulate and solve the nodal velocities in the X-direction approximately
2. Formulate and solve the nodal velocities in the Y-direction approximately
3. Formulate and solve the nodal velocities in the Z-direction approximately
4. Formulate the pressure equation using these approximate velocities
5. Solve the pressure equation
6. Update velocities based on conservation of mass
7. Formulate and solve the energy equation for temperature
8. Solve species transport equations
9. Update temperature-dependent properties
10. Solve turbulence equations
11. Update effective viscosity based on the turbulent solution
12. Calculate convergence monitors
13. End of global iteration

CFD solver algorithms for solving fundamental CFD equations may be adjusted for each DOF. Options include the Tri-Diagonal Matrix Algorithm (TDMA), Conjugate Residual (CR) method, Preconditioned Conjugate Residual (PCCR) method, Preconditioned Generalized Minimum Residual (PGMR) method, Preconditioned BiCGStab (PBCGM) method, and a Sparse Direct solver [1]. TDMA, a special case of the standard Gauss-Seidel iterative method, is preferred for approximate solutions to the momentum and turbulence equations when exact solutions are not required [1]. CR,

PCCR, PGMR, and PBCGM methods are semi-direct solvers that iterate to a specified convergence criterion based on search directions. These semi-direct algorithms may conclude when convergence is achieved, the maximum number of iterations has been reached without convergence, or the solution has stalled. CR requires the least memory, but is insufficient for ill-conditioned thermal problems [1]. PCCR requires more memory than CR, and is better suited for solving ill-conditioned conjugate heat transfer problems [1]. PGMR is the most memory intensive method because of its tighter convergence capability, and is the solver recommended by ANSYS® for extremely ill conditioned heat transfer [1]. PBCGM is similar to PGMR in ability to solve extremely ill conditioned heat transfer problems, but is requires less memory [1]. The Sparse Direct solver factors the matrix and then uses backward/forward substitution to solve for unknowns [1]. A separate solver may be chosen for each DOF.

Individual DOF solutions are coupled in FLOTRAN® using a nonlinear segregated fashion with a Semi-Implicit Method for Pressure Linked Equations (SIMPLE). A more robust algorithm – known as SIMPLEN – has been added to the SIMPLEF algorithm in order to improve the convergence rate. These coupling algorithms directly affect steps one through seven of the global iteration process outlined previously. ANSYS® documentation contains references explaining these algorithm's backgrounds [1].

Discretization of Equations. In order for a finite element code to conduct these calculations, element matrices are derived separately for each variable by a discretization of the fluid flow equations in a process known as a segregated sequential solver algorithm [1]. This process takes different forms depending on the terms within the equation. Momentum, energy, and turbulence equations have four types of terms: transient, advection, diffusion, and source. Galerkin's method of weighted residuals yields a weighting function, or shape function. This function is used to form element integrals used in deriving element matrices for formulation of the matrix equations [1]. More detail on shape functions used for specific matrices or vectors is included at the end of this chapter.

The transient term is solved first, using the Newmark integration method or the forward difference time integration methods. Refer to the discussion on transient analysis earlier in this chapter for information on these methods.

The advection term may be solved in one of three ways within FLOTRAN®: monotone streamline upwind (MSU) is first order accurate, streamline upwind / Petro-Galerkin (SUPG) and collocated Galerkin (COLG) are both second order accurate, with a tendency to produce oscillatory results [1]. MSU assumes no advection occurs across characteristic lines, or streamlines; thus the advection term is constant throughout an element. SUPG consists of a Galerkin discretization and perturbation term acting in the advection direction. This perturbation term yields more stability than in pure Galerkin discretization. In the COLG approach, element-based velocities are introduced to the SUPG scheme. These velocities must satisfy the continuity equation, while traditional velocities satisfy the momentum equations. The COLG approach is useful for coarsely meshed steady-state incompressible flows. SIMPLEN uses SUPG to solve momentum and energy equations and MSU for turbulence and pressure.

The diffusion contribution results from an integration over the problem's domain of the diffusion term multiplied by a weighting function [1]. Source term contribution results from multiplying the source terms by the weighting function and integrating over the domain [1]. These weighting functions, or shape functions, are described in the Figure B.2 and Table B.5 for FLUID141 elements [1].

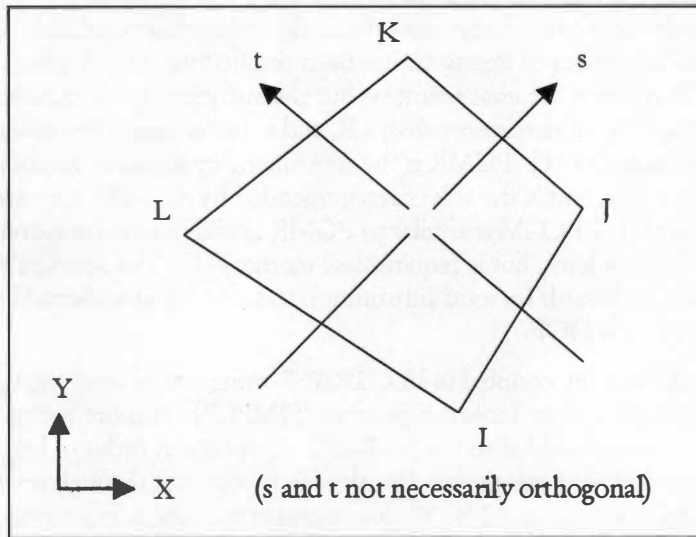


Figure B.2: 2-D, 4-Node Quadrilateral FLUID141 Element

Table B.3: Shape Functions for FLUID141 DOF

| Matrix or Vector   | Shape Function  |
|--|---|
| Advection-Diffusion Matrices for Momentum Equations ( $i = X, Y$ or $Z$ )                    | $U_i = \frac{1}{4} \left[ \sum_{m=I}^L U_{i,m} (1-s)(1-t) \right]$  |
| Advection-Diffusion Matrix for Pressure  | $P = \frac{1}{4} \left[ \sum_{m=I}^L P_m (1-s)(1-t) \right]$  |
| Advection-Diffusion Matrix for Energy (Temperature)  | $T = \frac{1}{4} \left[ \sum_{m=I}^L T_m (1-s)(1-t) \right]$  |
| Advection-Diffusion Matrices for Turbulent Kinetic Energy (ENKE) and Dissipation Rate (ENDS) | $ENKE = \frac{1}{4} \left[ \sum_{m=I}^L ENKE_m (1-s)(1-t) \right];$<br>$ENDS = \frac{1}{4} \left[ \sum_{m=I}^L ENDS_m (1-s)(1-t) \right]$ |
| Momentum Equation Source Vector  | Same as momentum equation matrix  |
| Pressure Equation Source Vector  | Same as pressure matrix   |
| Turbulent Kinetic Energy and Dissipation Rate Source Term Vectors                            | Same as kinetic energy and dissipation rate matrices  |

**Post-Processing Results.** FLOTRAN® will plot velocity vectors for each node. These vectors indicate magnitude with either color or length, or both. Contour plots of velocity and pressure use a color spectrum to visualize gradients in the property's values. Paths can be defined along lines of interest in order to plot two variables against one another, or to plot a specific variable along the line on the model itself. All results may be listed. Convergence monitors along with average, maximum, and minimum DOF values yield insight into the solution's convergence, and mass flow calculations ensure conservation of mass has been achieved.

## STRUCTURAL FUNDAMENTALS

ANSYS® uses the principle of virtual work to derive structural matrices [1]. Under this principle, virtual changes, denoted by the virtual operator  $\delta$ , in the internal strain energy  $Y$  are identically offset by a change in the external work  $\zeta$  due to applied loads.

$$\delta Y = \delta \zeta \quad (B21)$$

Therefore, virtual work may be expressed by equation B22 without thermal affects assuming linear deformations so that Hooke's law remains valid.

$$\delta Y = \int_{vol} \left( \{\delta \varepsilon\}^T [D] \{\varepsilon\} \right) d(vol) \quad (B22)$$

In equation B22,  $[D]$  is the elastic stiffness matrix, or stress-strain matrix. Equation B22 may be revised into equation B23 by relating the strain vector  $\{\varepsilon\}$  to virtual changes in the nodal displacement vector  $\{\delta u\}$  as a multiple of the strain-displacement matrix  $[B]$ .

$$\delta Y = \{\delta u\}^T \int_{vol} \left( \{B\}^T [D] \{B\} \right) d(vol) \{u\} \quad (B23)$$

The strain-displacement matrix is based on the element shape functions, which are described in the *ANSYS Structural Analysis* section later in this Appendix.

External work is expressed as the sum of inertial, pressure, and nodal terms. The inertial term is a function of general point displacements  $\{w\}$  and the D'Alembert's acceleration force vector  $\{F^a\}$ .

$$\delta \zeta_{inertia} = - \int_{vol} \left( \{\delta w\}^T \frac{\{F^a\}}{vol} \right) d(vol) \quad (B24)$$

Newton's second law, written in similar nomenclature, suggests that this acceleration force vector equals the material density multiplied by the second derivative of the displacement vector  $\{w\}$ . These general displacements,  $w$ , are internal element displacements that are related to the nodal displacement vector as a multiple of the shape function matrix  $[N]$ . Equation B24 may be rewritten as equation B25 if density,  $\rho$ , is constant over the volume.

$$\delta \zeta_{inertia} = - \{\delta u\}^T \rho \int_{vol} \left( [N]^T [N] \right) d(vol) \frac{\delta^2 \{u\}}{\delta t^2} \quad (B25)$$

Work due to external pressure, equation B26, is expressed in terms of an applied pressure vector  $\{p\}$  acts on a surface or area.

$$\delta\zeta_{pr} = \{\delta u\}^T \int_{area} ([N]^T \{p\}) d(area) \quad (B26)$$

Work due to externally applied nodal forces on elements  $\{F_e^{nd}\}$  is expressed by equation B27.

$$\delta\zeta_{nd} = \{\delta u\}^T \{F_e^{nd}\} \quad (B27)$$

Combining equations B23, B25, B26, and B27 into equation B21 yields one expression for virtual work.

$$[K_e] \{u\} = [M_e] \{\ddot{u}\} + \{F_e^{pr}\} + \{F_e^{nd}\} \quad (B28)$$

In equation B28,  $[K_e]$  is the element stiffness matrix,  $[M_e]$  is the element mass matrix,  $\{\ddot{u}\}$  is the acceleration vector, and  $\{F_e^{pr}\}$  is the element pressure vector.

The mass matrix formulation is element dependant within ANSYS®. A lumped mass formulation is also coded in ANSYS® to reduce the load vector by removing rotational DOF [1]. For a static analysis, the mass matrix formulation you use does not significantly affect the solution accuracy. The choice of mass matrix formulation is primarily important in dynamic analyses where the structure contains initial stresses [1].

## ANSYS STRUCTURAL ANALYSIS

Structural finite element analysis in ANSYS® consists primarily of calculating nodal displacements, then using these results to derive other quantities such as stresses or reaction forces [1]. These calculations apply to static analysis when the loading is constant, or to transient dynamic analysis when the loads vary in time. Both linear and nonlinear (i.e. plasticity or stress hardening) solution capabilities, as well as modal, harmonic, spectrum and buckling analyses, are all available in ANSYS®. Refer to the ANSYS® Structural Analysis Guide for a discussion of these options.

ANSYS® contains two solution methods for structural analyses: the h-method and the p-method [1]. The h-method – useful for any analysis type – is the system default. The p-method, or polynomial method, is only useful for static analyses, and has several advantages. The p-method allows the user to define a desired level of accuracy by adjusting the polynomial level. By doing so, the structural FEM may not have to be as fine.

A static structural analysis ignores dampening and inertial loads, with the exception of gravity and rotational inertial loads [1]. Problems with time-varied loads that may be considered statically equivalent may be solved with this technique also. Typical loading scenarios include external forces, steady-state inertial forces, imposed displacements, temperatures, and fluences. A typical analysis consists of six steps [1].

- Modeling
- Solution Controls
- Solution Options
- Apply Loads and DOF Constraints
- Execute Solution Algorithms
- Post-Processing Results

**Modeling.** Element types, real constants, material models, and model geometry definitions constitute the modeling phase. Multiple finite element categories are provided within ANSYS® for solving structural problems, each containing multiple element types. These categories include spars, beams, pipes, two and three-dimensional solids, shells, and specialized element types [1]. ANSYS® contains a two-dimensional beam element with tension, compression, and bending capabilities known as BEAM3 [1]. The element has three DOF for each of its two nodes: displacement in the X-direction (UX), displacement in the Y-direction (UY), and rotation about the Z-axis (ROTZ).

This element is depicted in Figure B.3. Real constants define geometric attributes specific to each element type. For example, a two-dimensional beam element BEAM3 has real constants defining area, area moment of inertia, beam height, shear deflection, initial strain, and added mass per unit length [1]. Each element type chosen must have an associated material model. These models can be defined by the user, or selected from an internal library [1]. The user must implement consistent units during modeling, material selection, and post processing results.

BEAM3 elements may be considered to have four faces for the purpose of surface loading. Face one lays between nodes I and J with a negative Y normal direction. Face two also lays between nodes I and J, but with a positive X normal direction. Faces three and four are at nodes I and J, respectively. The cross-section of this element is not limited, but stresses are derived as though the neutral axis is half of the beam's height. The height is only used in deriving bending stresses. These elements must lie in the X-Y plane and have a non-zero length and area [1].

**Solution Controls.** While adjusting solution controls, decisions must be made regarding the analysis type, load stepping, and solution output [1]. Considerations for the analysis type include large or small displacements, static or transient loading, or restarting a previous analysis. Load stepping refers to the application of loads during the solution process. Different loading scenarios occur in load steps that are associated with a "time." This time is merely a counter for static analyses [1]. In a transient analysis, loads may be stepped or ramped across as a load step increment of time. Also, dampening coefficients and integration parameters may be adjusted [1].

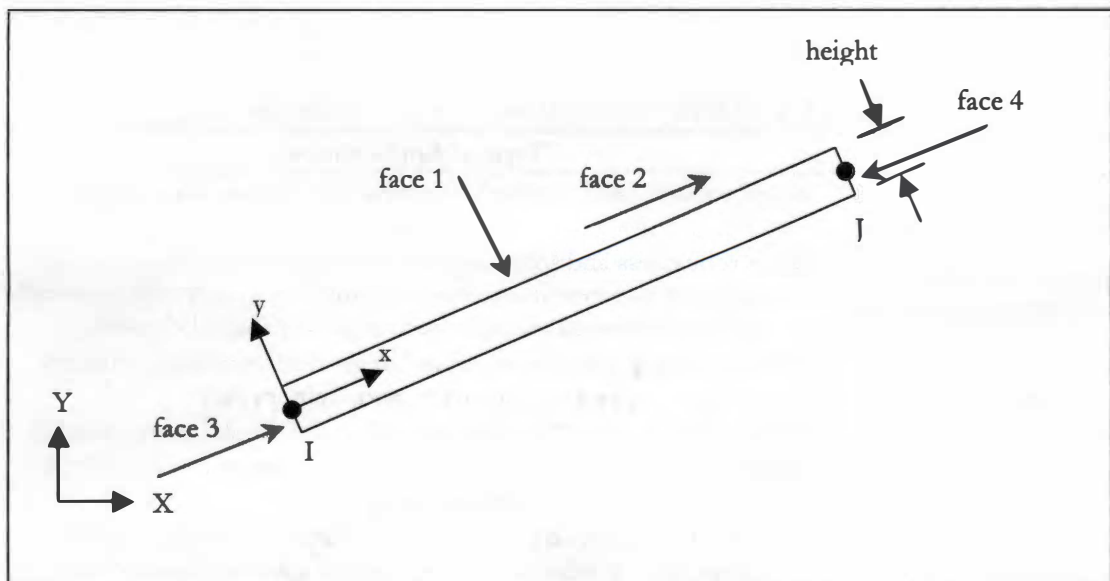


Figure B.3: BEAM3 Element



**Solution Options.** Solution options include selection of equation solvers and restarts controls. ANSYS® will select an equation solver based on the physical problem, or the user may specify one of the available solution options: sparse direct, Jacobi conjugate gradient (JCG), incomplete Cholesky conjugate gradient (ICCG), preconditioned conjugate gradient (PCG), and frontal direct or wavefront [1]. Table B.6 contains brief descriptions of applications for these solvers, which are discussed later in this chapter.

**Apply Loads and DOF Constraints.** Loads may be applied to a structure as displacements, forces, moments, pressures, temperatures, or fluences [1]. The model may be constrained by setting a DOF to a constant value [1]. Structural pressure loads are applied as surface loads in ANSYS®, meaning they are applied as distributed loads over a surface to selected elements and corresponding nodes [1].

**Execute Solution Algorithms.** Steady-state structural finite element modeling produces a system of simultaneous linear equations that may be solved directly by Gaussian elimination or by an iterative method. This system of equations consists of a stiffness matrix  $[K]$ , displacement vector  $\{u\}$ , and force vector  $\{F\}$  [1].

$$[K]\{u\} = \{F\} \tag{B29}$$

Gaussian, or direct, elimination involves decomposition of the stiffness matrix to compute the solution matrix. Both the frontal (wavefront) solver and the sparse direct solver use this method. Iterative solvers start with an initial guess for the unknown displacement vector and successively steps through solutions until a tolerance level has been achieved [1].

In a static analysis, ignoring inertial and damping effects, the overall equilibrium equation B29 can be expanded to equation B30.

$$\sum_{m=1}^n [K_e] \{u\} = \left( \{F^{nd}\} + \{F^{ac}\} + \sum_{m=1}^n (\{F_e^{th}\} + \{F_e^{pr}\}) \right) + \{F^r\} \tag{B30}$$

Table B.4. ANSYS® Structural Solvers and Applications

| Solver  | Typical Applications  |
|---|---|
| Frontal Solver<br>(direct elimination solver)       | When robustness is required (nonlinear analysis) or when memory is limited.   |
| Sparse Direct Solver<br>(direct elimination solver) | When robustness and solution speed are required (nonlinear analysis); for linear analysis where iterative solvers are slow to converge (especially for ill-conditioned matrices, such as poorly shaped elements). |
| JCG Solver<br>(iterative solver)                    | When solution speed is crucial in "single-field" problems (thermal, magnetic, acoustics, and multiphysics)  |
| ICCG Solver<br>(iterative solver)                   | When solution speed is crucial in multiphysics applications. Handles models that are harder to converge in other iterative solvers (nearly indefinite matrices).  |
| PCG Solver<br>(iterative solver)                    | When solution speed is crucial (linear analysis of large models). Especially well suited for large models with solid elements.  |

In equation B30,  $n$  is the number of elements,  $e$  denotes an element,  $nd$  denotes applied loads,  $ac$  denotes acceleration loads,  $th$  denotes thermal loads,  $pr$  denotes pressure loads, and  $r$  denotes a reaction load [1]. For a transient analysis, a mass matrix  $[M]$  and damping matrix  $[C]$ , joined with appropriate nodal acceleration vectors and velocity vectors, appear on the left hand side of equation A9. Transient solutions proceed in the same manner described for transient fluid analyses discussed later in this Appendix in the *Set FLOTRAN<sup>®</sup> Analysis Parameters* section.

Element and mass stiffness matrices, in the element coordinates, are shown in Chapter 14.3 of the ANSYS<sup>®</sup> Theory Reference for BEAM3 elements (ANSYS). The element pressure load vector, in the element coordinate system, for BEAM3 elements in ANSYS<sup>®</sup> is given by equation B31 assuming uniform lateral pressure (ANSYS, Theory Reference, 14.3):

$$\{F_e^{pr}\} = \left\{ 0 \quad -\frac{pL}{2} \quad -\frac{pL^2}{12} \quad 0 \quad -\frac{pL}{2} \quad \frac{pL^2}{12} \right\}^T \quad (B31)$$

Weighting functions, or shape functions, are described in Figure B.4 and Table B.7 for BEAM3 elements [1].

**Post-Processing Results.** Results may be evaluated once a solution is obtained by listing reaction forces for each constrained DOF at constrained nodes. The total force and total moment on any node may be listed. This total load should sum to zero for equilibrium on all nodes except where applied loads or reactions exist [1]. The deformed shape may be plotted against the undeformed structure. For small deflections, deformations may be exaggerated so that the maximum deflection is five percent of the maximum model length [1].

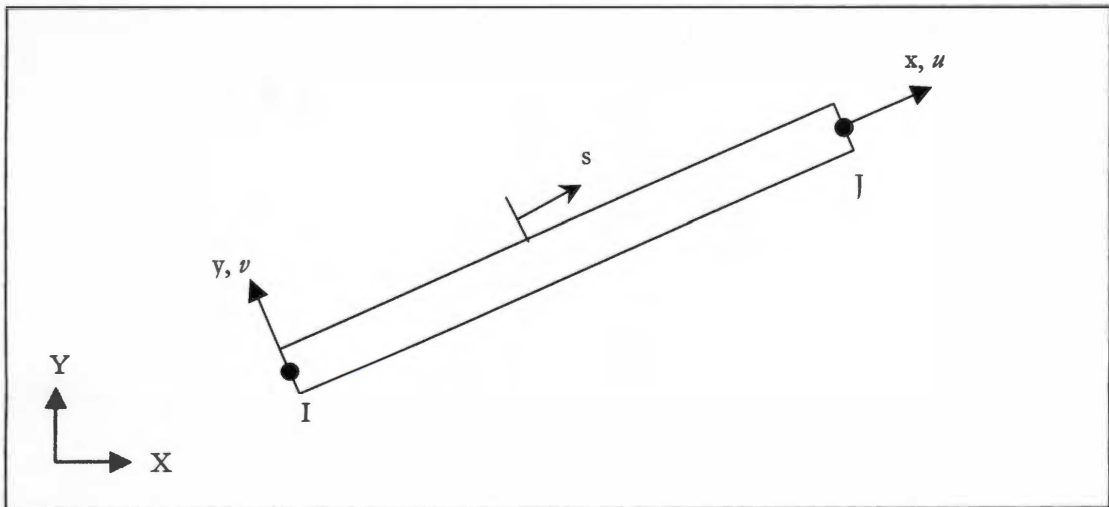


Figure B.4: 2-D, 2-node BEAM3 Element

Table B.5. Shape Functions for BEAM3 DOF

| Matrix or Vector  | Shape Functions   |
|---|---|
| Stiffness and Mass Matrices;<br>Thermal and Pressure Load Vectors | $u = \frac{1}{2} [u_I (1 - s) + u_J (1 + s)];$ $v = \frac{1}{2} \left[ v_I \left( 1 - \frac{s(3 - s^2)}{2} \right) + v_J \left( 1 + \frac{s(3 - s^2)}{2} \right) \right]$ $+ \frac{L}{8} [\theta_{z,I} (1 - s^2)(1 - s) + \theta_{z,J} (1 - s^2)(1 + s)]$ |
| Stress Stiffness Matrix   | Same as $v$ from Stiffness and Mass Matrices Above  |

APPENDIX C: TYPICAL FLOTRAN® INPUT FILE

---

ANSYS Release: 7.0

Release Date: 2002/10/10

A N S Y S / F L O T R A N

Job Name: 16deg

2D XY ADIABATIC COMPRESSIBLE TURBULENT FLOW

Writing results to 16deg.rfl file.

Writing the following degrees of freedom:

VX VY PRES TEMP ENKE ENDS DENS VISC EVIS ECON

File: airfoil

Analysis Settings 10/08/2003 09:08:19

Analysis Options Output Control

|                    |   |                        |      |
|--------------------|---|------------------------|------|
| Flow Solution      | T | Max. Global Iterations | 1000 |
| Turbulent          | T | Summary Frequency      | 10   |
| Compressible       | T | Overwrite Frequency    | 1000 |
| Thermal            | F | Append Frequency       | 500  |
| Transient          | F |                        |      |
| Swirl              | F |                        |      |
| Species Transport  | F |                        |      |
| Free Surface       | F |                        |      |
| Incomp. Visc. Heat | F |                        |      |
| ALE formulation    | F |                        |      |
| Radiosity Solution | F |                        |      |

Algorithm Control

-----  
SIMPLEN algorithm is used in this analysis

| Variable | Termination Criterion |
|----------|-----------------------|
| VX       | 1.00E-02              |
| VY       | 1.00E-02              |
| VZ       | 1.00E-02              |
| PRES     | 1.00E-08              |
| ENKE     | 1.00E-02              |
| ENDS     | 1.00E-02              |
| TEMP     | 1.00E-08              |

#### Fluid Properties

|            |            |                |             |
|------------|------------|----------------|-------------|
| Density:   | AIR-IN     | Conductivity:  | CONSTANT    |
| Nominal:   | 1.0909E-07 | Nominal:       | -1.0000E+00 |
| Variable:  | T          | Variable:      | F           |
| Viscosity: | AIR-IN     | Specific Heat: | CONSTANT    |
| Nominal:   | 2.6420E-09 | Nominal:       | -1.0000E+00 |
| Variable:  | T          | Variable:      | F           |

Update Frequency 1

#### Property Calculations

| Property     | Form        | Coefficients |
|--------------|-------------|--------------|
| Density      | 11          | 2.47327E+05  |
| Viscosity    | 12          | 1.57850E-10  |
|              |             | 1.99000E+02  |
| Bulk modulus | 0.10000E+16 |              |
| Initial      | 0.00000E+00 |              |
| Viscosity    |             |              |

Operating Conditions

|                      |             |                    |            |
|----------------------|-------------|--------------------|------------|
| Bulk Temp for H Calc | 73.7113     | Temperature Offset | 460.00     |
| Reference Pressure   | 1.39796E+01 | Gas Constant       | 2.4733E+05 |
| Total Temperature    | 73.7113     | Ratio CP/CV        | 1.4000E+00 |
| Nominal Temperature  | 73.7113     |                    |            |

Acceleration

-----

|             |            |
|-------------|------------|
| X component | 0.0000E+00 |
| Y component | 0.0000E+00 |
| Z component | 0.0000E+00 |

Rotational Terms

-----

|                  |                 |
|------------------|-----------------|
| Rotational Speed | Rotational Axis |
|                  | Offset          |
| X 0.0000E+00     | X 0.0000E+00    |
| Y 0.0000E+00     | Y 0.0000E+00    |
| Z 0.0000E+00     | Z 0.0000E+00    |

| Variable | Relaxation |       | Quadrature |   | Diff | Src | Adv |
|----------|------------|-------|------------|---|------|-----|-----|
|          | Schmidt #  | Under | Inertial   |   |      |     |     |
| VX       | 1.00       | 0.800 | 1.00E+15   | 0 | 0    | 2   |     |
| VY       | 1.00       | 0.800 | 1.00E+15   | 0 | 0    | 2   |     |
| VZ       | 1.00       | 0.800 | 1.00E+15   | 0 | 0    | 2   |     |
| PRES     | 0.00       | 0.500 | 1.00E+15   | 1 | 1    | 2   |     |
| ENKE     | 1.00       | 0.500 | 1.00E+15   | 0 | 2    | 2   |     |
| ENDS     | 1.30       | 0.500 | 1.00E+15   | 0 | 2    | 2   |     |
| TEMP     | 1.00       | 0.800 | 1.00E+15   | 0 | 2    | 2   |     |
| DENS     | 0.00       | 1.000 | 0.00E+15   | 0 | 0    | 0   |     |
| VISC     | 0.00       | 0.500 | 0.00E+15   | 0 | 0    | 0   |     |
| COND     | 0.00       | 0.500 | 0.00E+15   | 0 | 0    | 0   |     |
| EVIS     | 0.00       | 0.500 | 0.00E+15   | 0 | 0    | 0   |     |
| ECON     | 0.00       | 0.500 | 0.00E+15   | 0 | 0    | 0   |     |
| TTOT     | 1.00       | 0.800 | 1.00E+15   | 0 | 2    | 2   |     |
| SPHT     | 0.00       | 1.000 | 0.00E+15   | 0 | 0    | 0   |     |
| SFTS     | 0.00       | 1.000 | 0.00E+00   | 0 | 0    | 0   |     |
| RDFL     | 0.00       | 0.000 | 0.00E+00   | 0 | 0    | 0   |     |

Artificial Viscosity 0.0000E+00

| Variable | Advection Formulation | MIR Stabilization Factor |
|----------|-----------------------|--------------------------|
| VX       | SUPG                  | 0.00000E+00              |
| VY       | SUPG                  | 0.00000E+00              |
| VZ       | SUPG                  | 0.00000E+00              |
| PRES     | MSU                   | 0.00000E+00              |
| ENKE     | MSU                   | 0.00000E+00              |
| ENDS     | MSU                   | 0.00000E+00              |
| TEMP     | SUPG                  | 0.00000E+00              |

| Variable | Maximum Solver | Convergence Iterations | Search Criterion | Minimum Vectors | Delta    |
|----------|----------------|------------------------|------------------|-----------------|----------|
| VX       | PBCGM          | 100                    | 1.00E-05         | 2               | 1.00E-10 |
| VY       | PBCGM          | 100                    | 1.00E-05         | 2               | 1.00E-10 |
| VZ       | PBCGM          | 100                    | 1.00E-05         | 2               | 1.00E-10 |
| PRES     | PCCR           | 1000                   | 1.00E-12         | 2               | 1.00E-10 |
| ENKE     | PBCGM          | 100                    | 1.00E-05         | 2               | 1.00E-10 |
| ENDS     | PBCGM          | 100                    | 1.00E-05         | 2               | 1.00E-10 |
| TEMP     | PBCGM          | 1000                   | 1.00E-12         | 2               | 1.00E-10 |

The PBCGM Fill-In parameter is set to 0

Debug Output

Print Residuals F Debug Print Level 1  
Solution Error Est. 0

Turbulence Model used

Standard K-E Model

Turbulence Inlet Parameters

Turbulence Intensity 1.0000E-02 Length Scale Factor 1.0000E-02

Base Turbulence Model Constants

-----  
CMu     0.090     C1     1.440  
Kappa   0.400     C2     1.920  
E        9.000     C3     1.000  
A        26.000    C4     0.000

Transition Point for Y Plus Calc: 11.500  
Coefficient of Thermal Expansion: 0.00E+00  
Wall Conductivity Model: Van Driest

Effective Viscosity Initialization

-----  
Ratio to Laminar     1.0000E+03

Model Has 15538 Nodes and 15259 Elements



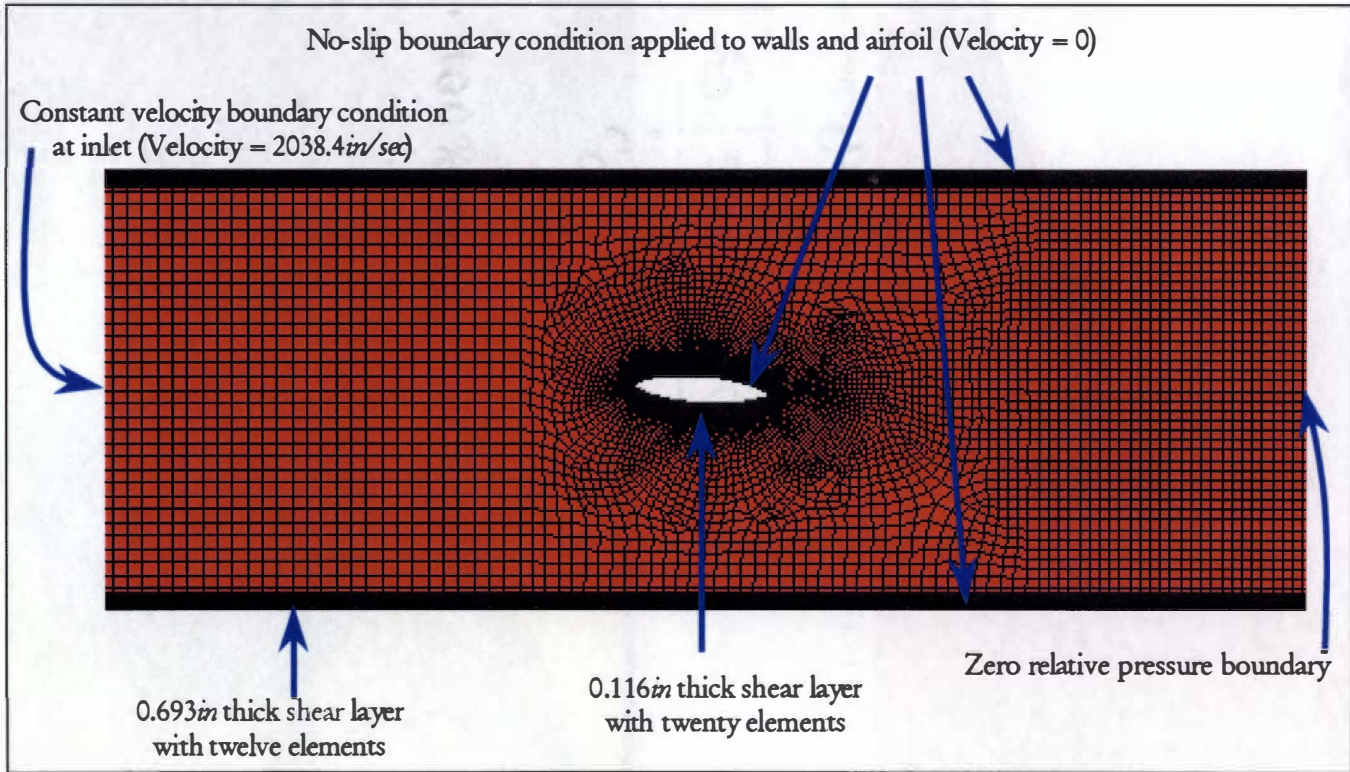


Figure D.1: FLUID141 FEM Around Airfoil at 4 Degrees Pitch

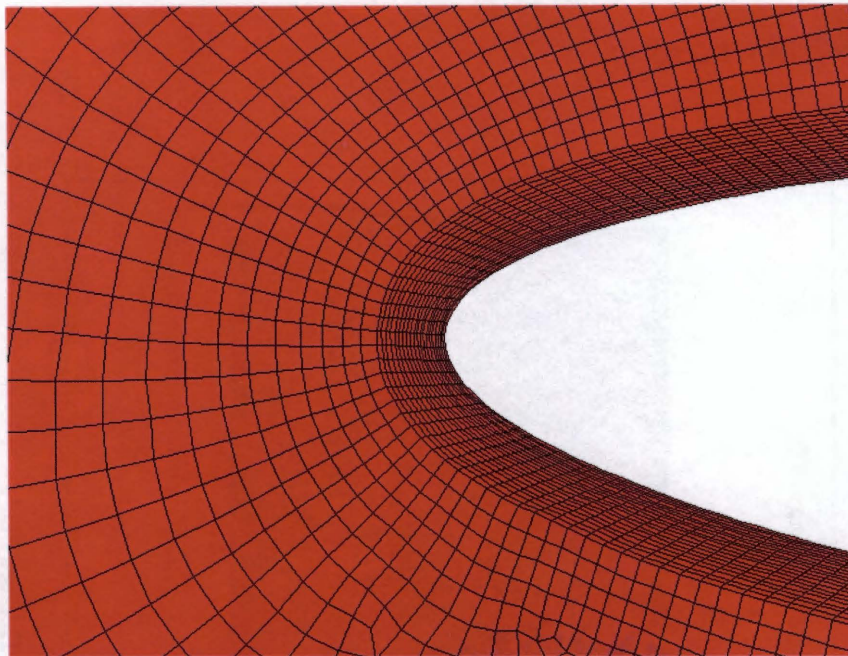


Figure D.2: FLUID141 FEM Detail Around Airfoil Nose, 4-Degree Pitch

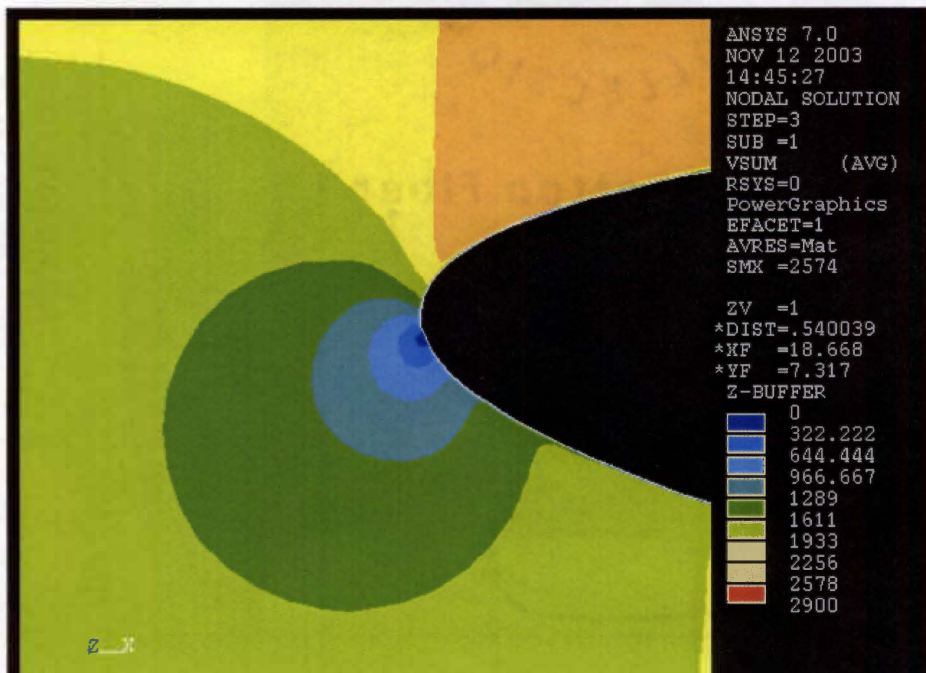


Figure D.3: 4-Degree, Average Velocity Contours Around Airfoil Nose



Figure D.4: FLUID141 FEM Detail Near Wall

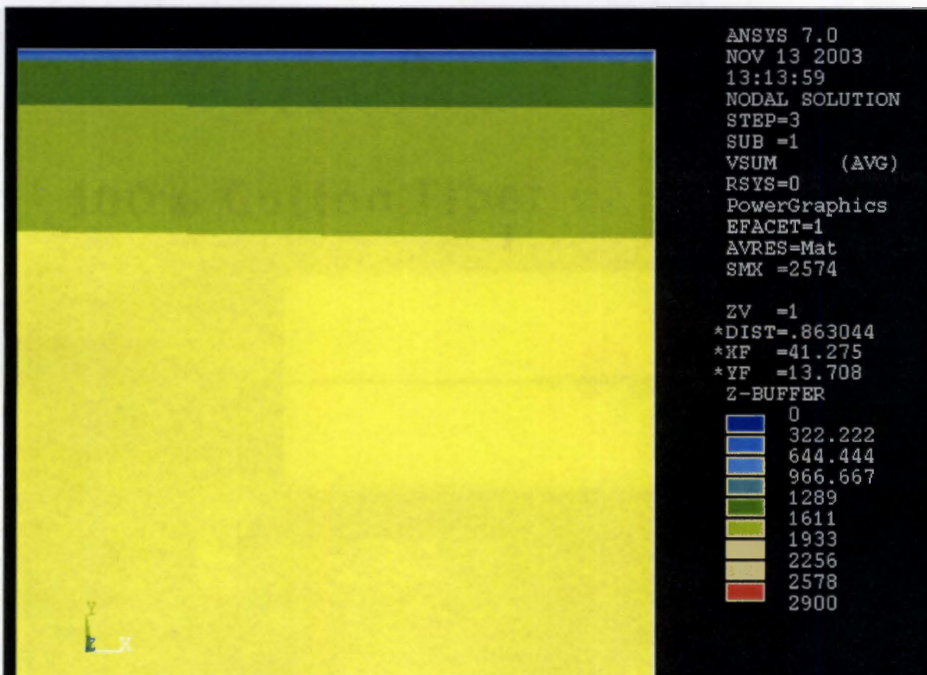


Figure D.5: 4-Degree, Average Velocity Contours Near Wall

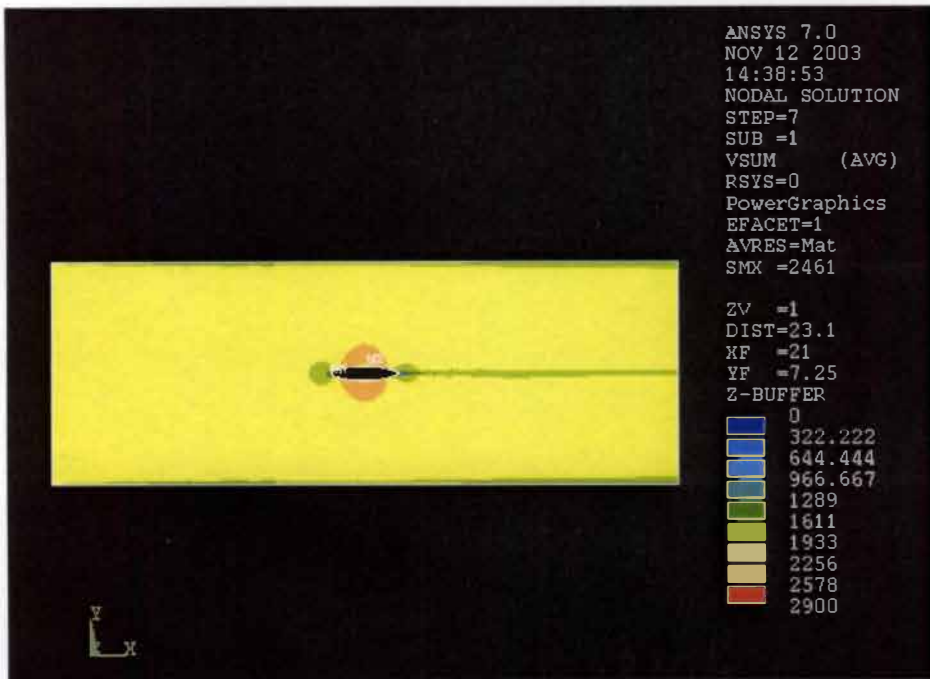


Figure D.6: 0-Degree, Average Velocity Contours, Max = 2461 *in/sec*

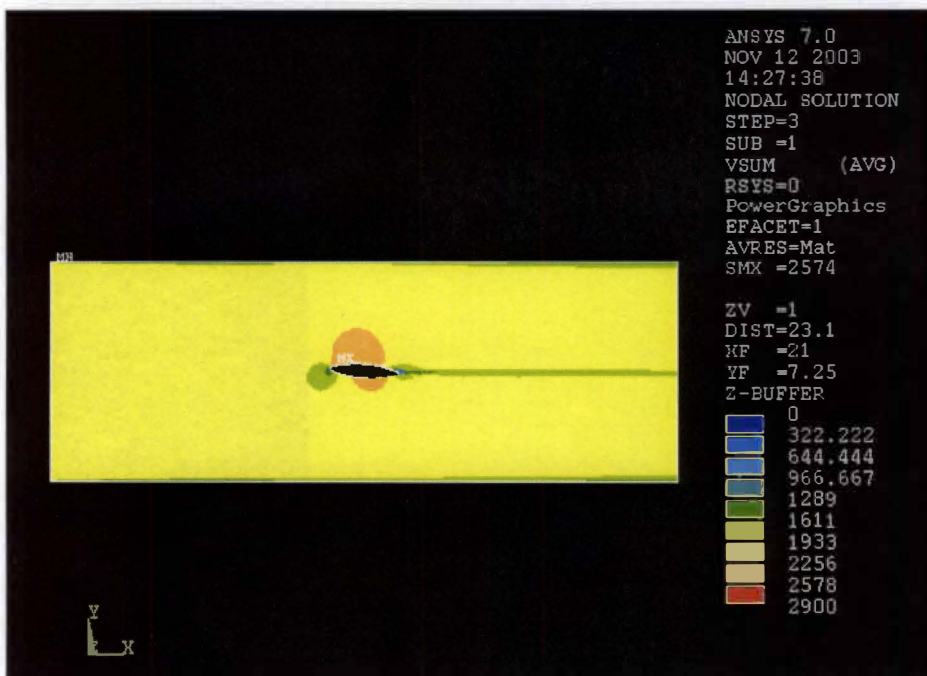


Figure D.7: 4-Degree, Average Velocity Contours, Max = 2574 *in/sec*

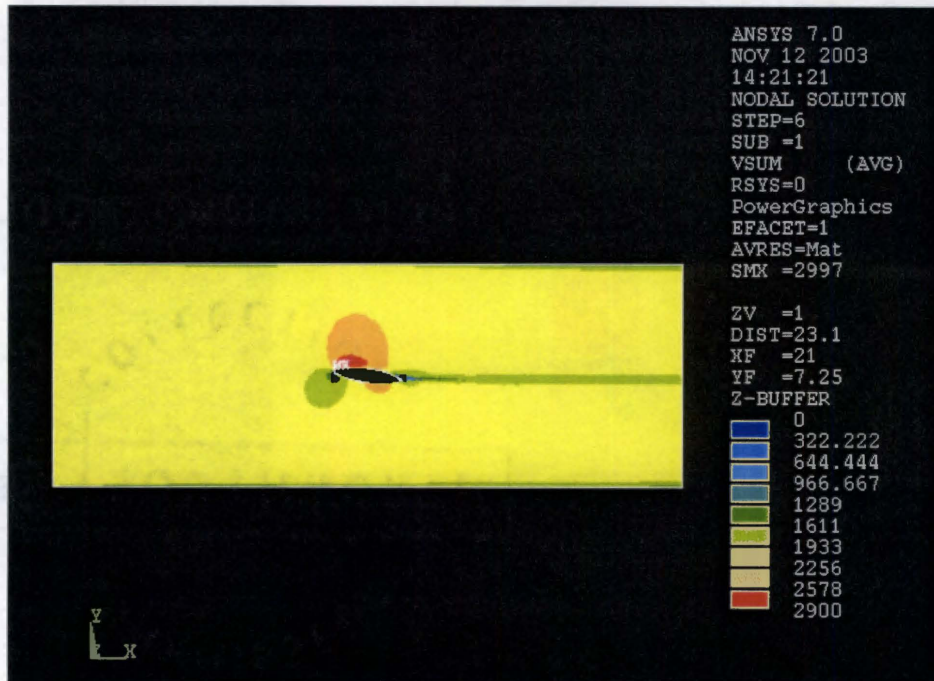


Figure D.8: 8-Degree, Average Velocity Contours, Max = 2997 in/sec

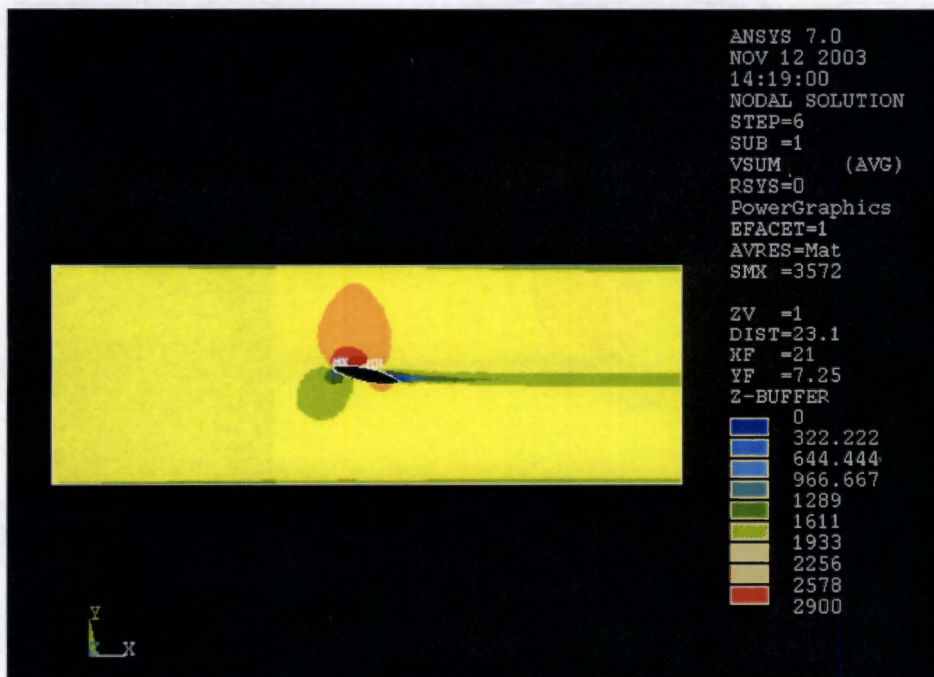


Figure D.9: 12-Degree, Average Velocity Contours, Max = 3572 in/sec

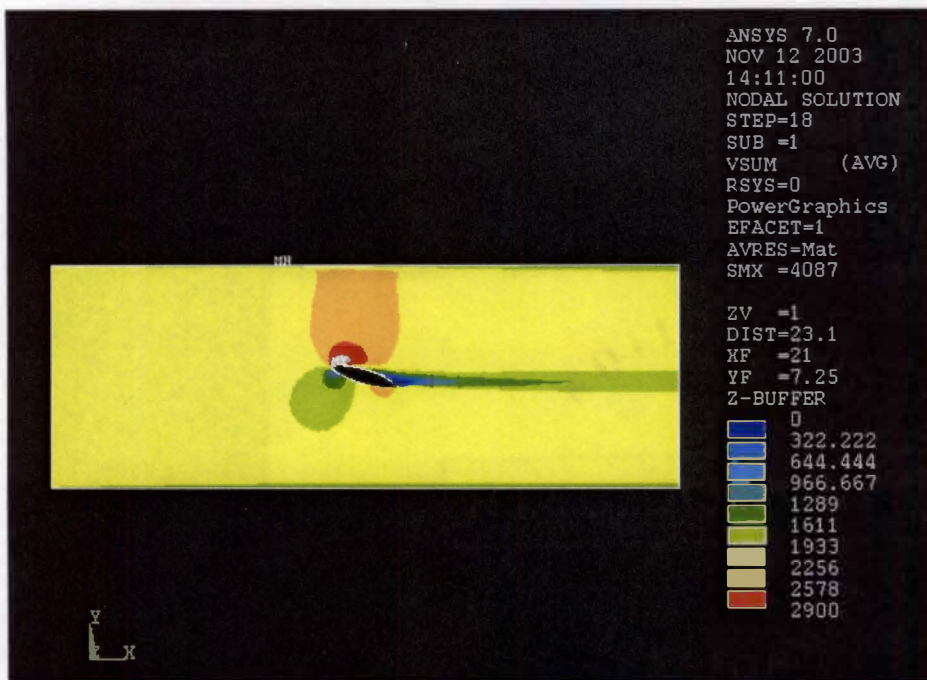


Figure D.10: 16-Degree, Average Velocity Contours, Max = 4087 *in/sec*

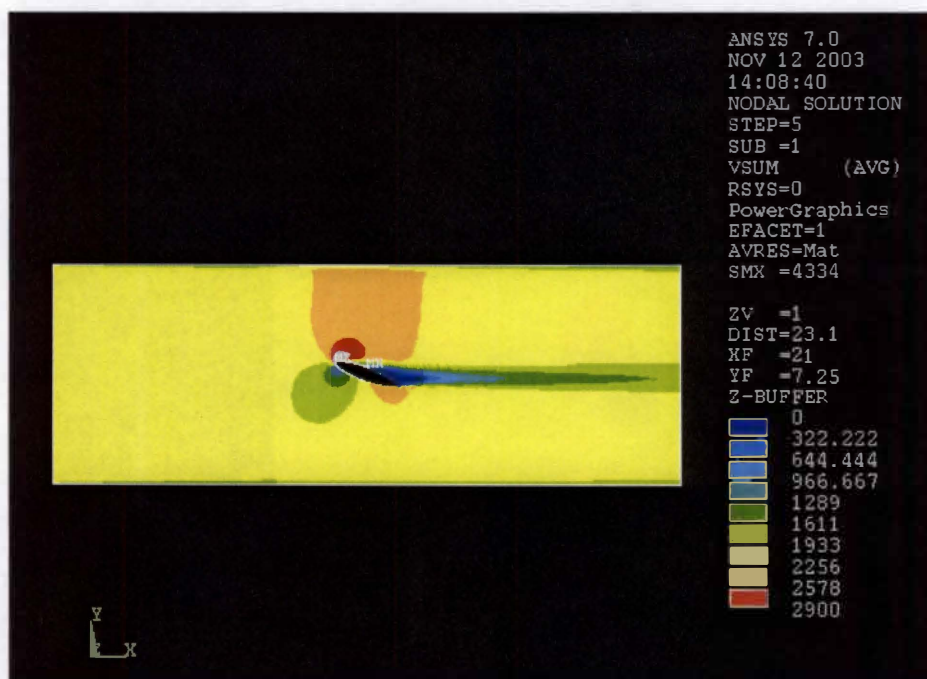


Figure D.11: 20-Degree, Average Velocity Contours, Max = 4334 *in/sec*

## PRESSURE CONTOUR PLOTS

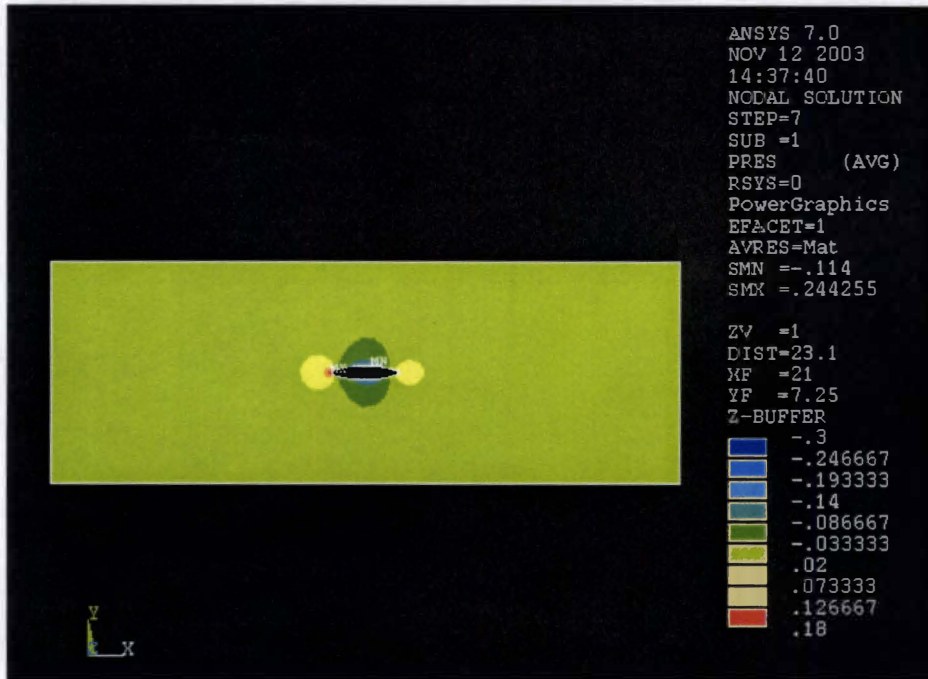


Figure D.12: 0-Degree, Relative Pressure, Max = 0.244 *psi*, Min = -0.114 *psi*

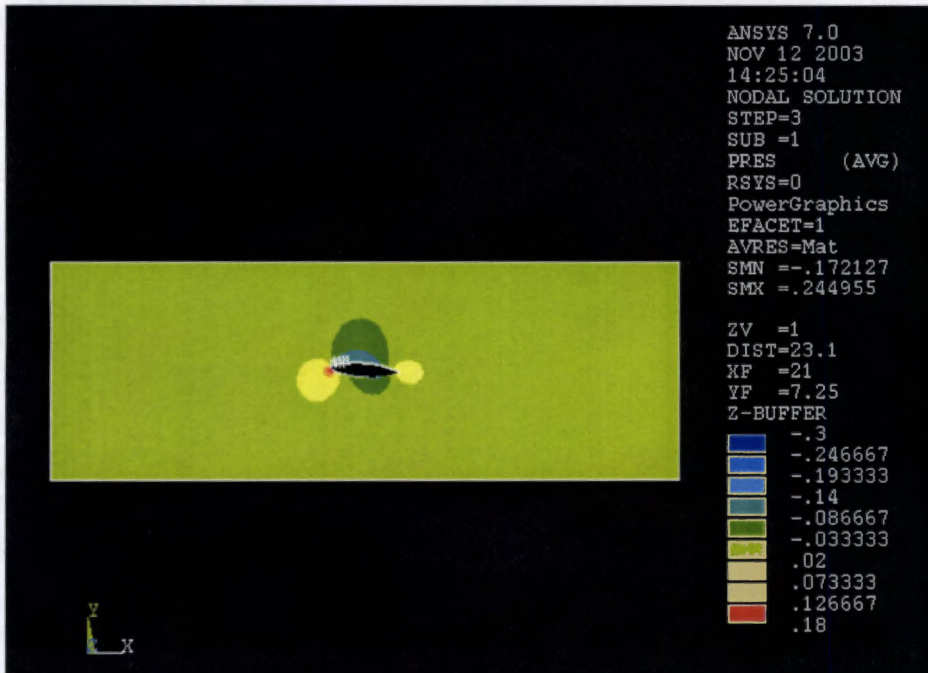


Figure D.13: 4-Degree, Relative Pressure, Max = 0.245 *psi*, Min = -0.172 *psi*

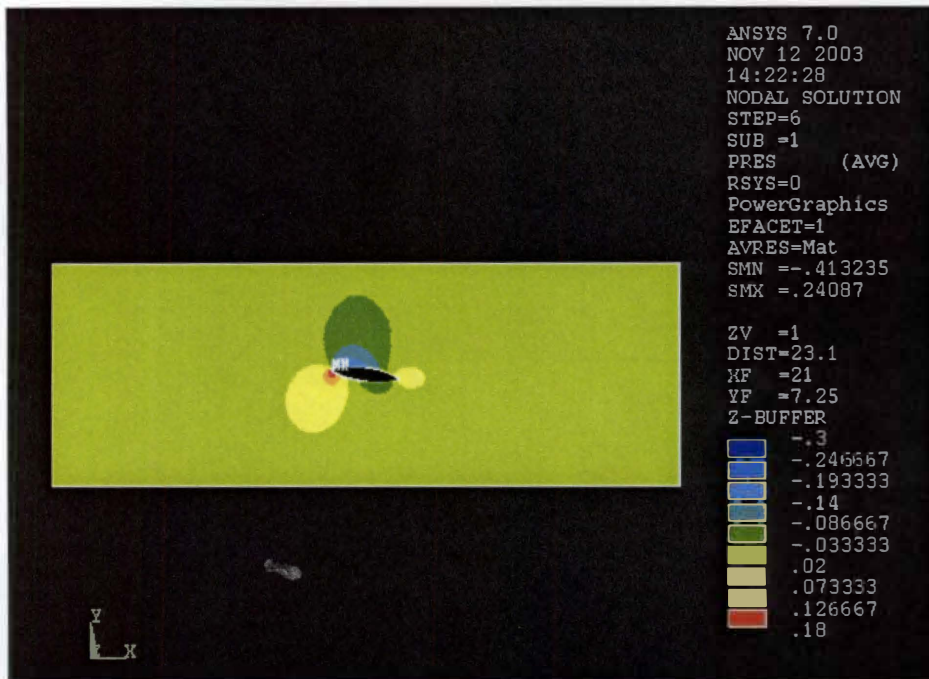


Figure D.14: 8-Degree, Relative Pressure, Max = 0.241 *psi*, Min = -0.413 *psi*

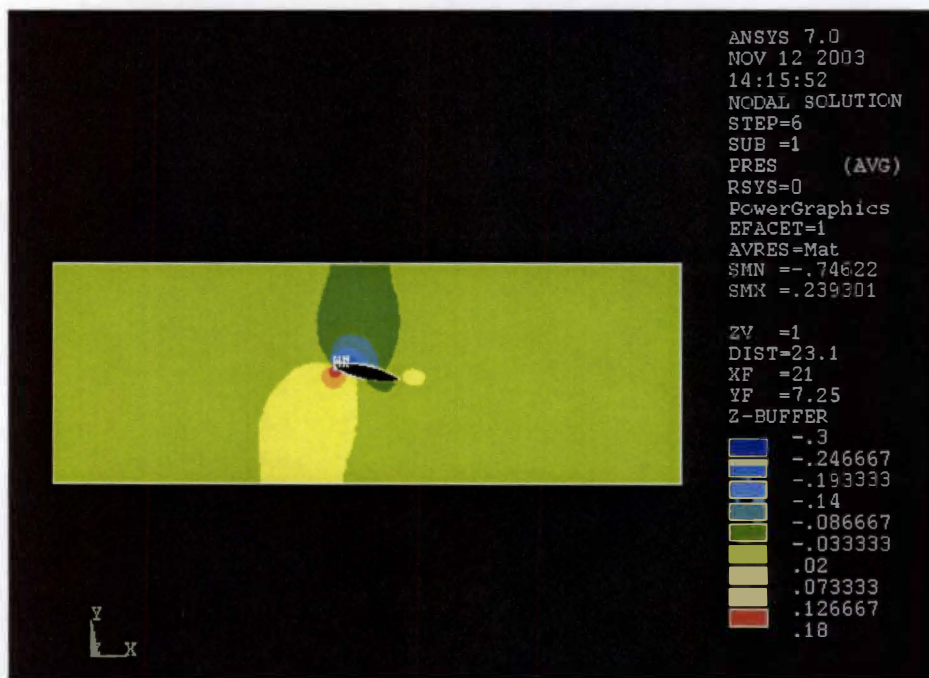


Figure D.15: 12-Degree, Relative Pressure, Max = 0.239 *psi*, Min = -0.746 *psi*



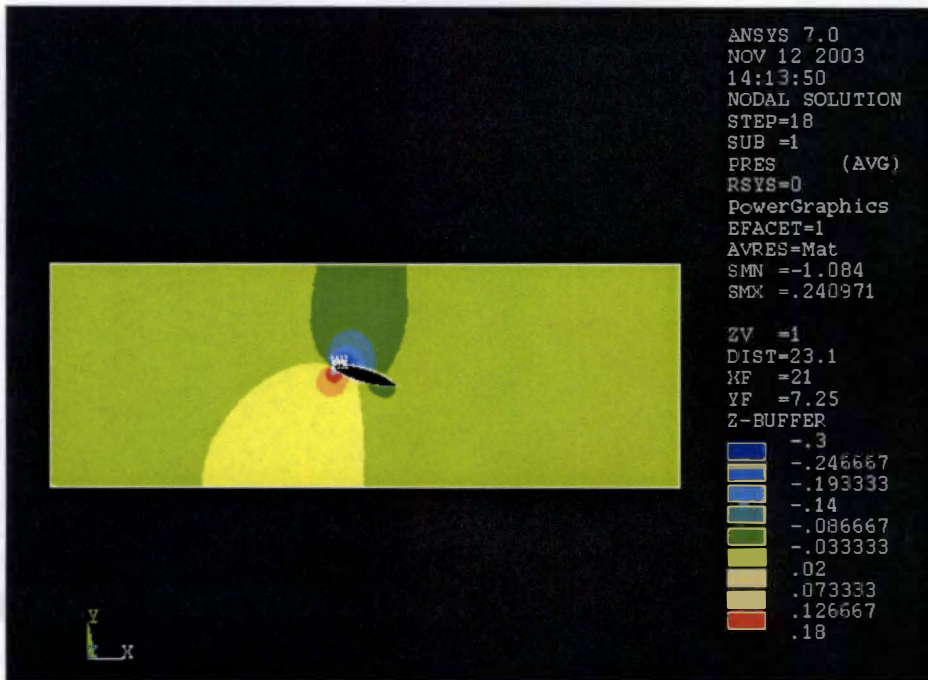


Figure D.16: 16-Degree, Relative Pressure, Max = 0.241 *psi*, Min = -1.08 *psi*

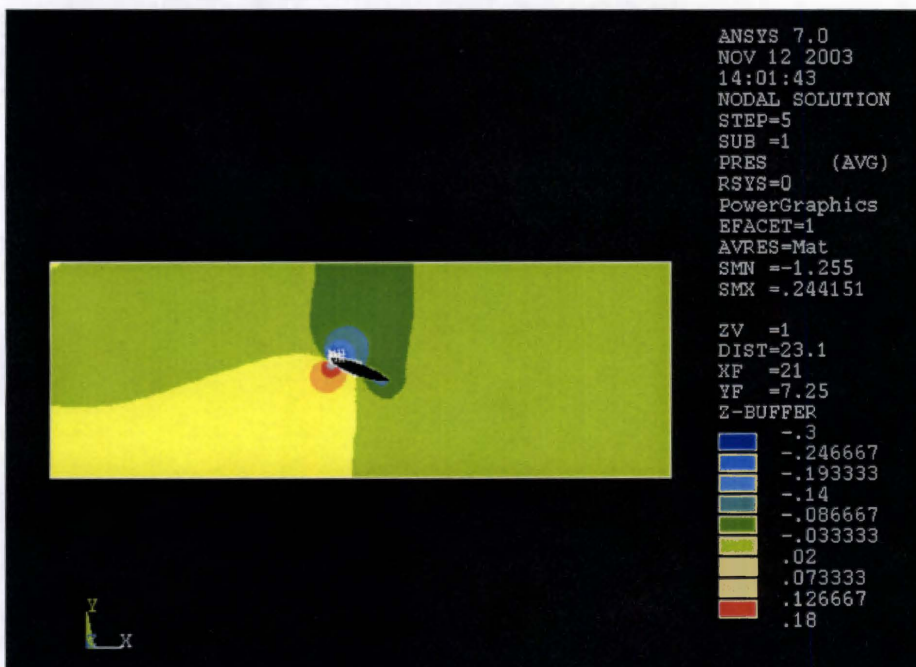


Figure D.17: 20-Degree, Relative Pressure, Max = 0.244 *psi*, Min = -1.26 *psi*

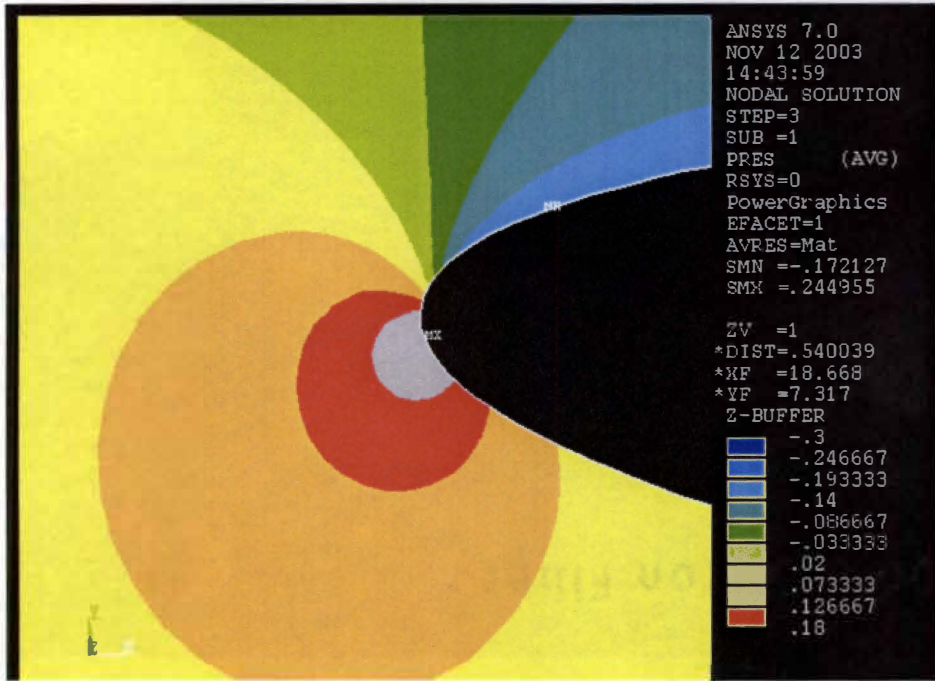


Figure D.18: 4-Degree, Relative Pressure Contours Around Airfoil Nose  
 (Grey Contour indicates pressure outside standardized contour plot range)

TABULATED CFD RESULTS SUMMARY

Table D.1: 0-Degree CFD Results Summary

| <b>Fluid Convergence Monitors</b>  |           |            |           |          |          |
|------------------------------------|-----------|------------|-----------|----------|----------|
| Vx                                 | Vy        | PRES       | ENKE      | ENDS     | TEMP     |
| 4.84E-07                           | 1.86E-07  | 6.26E-06   | 1.79E-06  | 1.73E-06 | 3.61E-09 |
| <b>Fluid Results Summary</b>       |           |            |           |          |          |
| Variable                           | Average   | Minimum    | Maximum   |          |          |
| Vx                                 | 1.90E +03 | 0.00E +00  | 2.46E +03 |          |          |
| Vy                                 | 2.60E +00 | -1.08E +03 | 1.08E +03 |          |          |
| PRES                               | -1.61E-02 | -1.14E-01  | 2.44E-01  |          |          |
| ENKE                               | 1.73E +04 | 4.77E +02  | 2.44E +05 |          |          |
| ENDS                               | 7.08E +07 | 5.91E +03  | 2.97E +09 |          |          |
| TEMP                               | 7.14E +01 | 7.02E +01  | 7.37E +01 |          |          |
| <b>Mass Flow Rate Summary</b>      |           |            |           |          |          |
| Total Mass Flow In = 0.31254E-02   |           |            |           |          |          |
| Total Mass Flow Out = -0.31253E-02 |           |            |           |          |          |
| ΔMass  = 1.E-07                    |           |            |           |          |          |

Table D.2: 4-Degree CFD Results Summary

| <b>Fluid Convergence Monitors</b>  |            |            |           |          |          |
|------------------------------------|------------|------------|-----------|----------|----------|
| Vx                                 | Vy         | PRES       | ENKE      | ENDS     | TEMP     |
| 4.71E-08                           | 2.54E-08   | 4.78E-07   | 1.73E-07  | 1.93E-07 | 3.03E-10 |
| <b>Fluid Results Summary</b>       |            |            |           |          |          |
| Variable                           | Average    | Minimum    | Maximum   |          |          |
| Vx                                 | 1.90E +03  | 0.00E +00  | 2.57E +03 |          |          |
| Vy                                 | -8.32E +00 | -7.26E +02 | 1.66E +03 |          |          |
| PRES                               | -1.85E-02  | -1.72E-01  | 2.45E-01  |          |          |
| ENKE                               | 1.95E +04  | 4.74E +02  | 3.05E +05 |          |          |
| ENDS                               | 7.78E +07  | 5.79E +03  | 4.16E +09 |          |          |
| TEMP                               | 7.14E +01  | 6.99E +01  | 7.37E +01 |          |          |
| <b>Mass Flow Rate Summary</b>      |            |            |           |          |          |
| Total Mass Flow In = 0.31393E-02   |            |            |           |          |          |
| Total Mass Flow Out = -0.31393E-02 |            |            |           |          |          |
| ΔMass  = 0.E-07                    |            |            |           |          |          |

Table D.3: 8-Degree CFD Results Summary

| <b>Fluid Convergence Monitors</b> |          |          |          |          |          |
|-----------------------------------|----------|----------|----------|----------|----------|
| Vx                                | Vy       | PRES     | ENKE     | ENDS     | TEMP     |
| 3.98E-07                          | 1.42E-07 | 8.56E-08 | 6.67E-07 | 8.04E-07 | 2.81E-09 |

| <b>Fluid Results Summary</b> |            |            |           |
|------------------------------|------------|------------|-----------|
| Variable                     | Average    | Minimum    | Maximum   |
| Vx                           | 1.87E +03  | -2.37E +02 | 2.84E +03 |
| Vy                           | -1.94E +01 | -5.86E +02 | 2.32E +03 |
| PRES                         | -2.07E-02  | -4.13E-01  | 2.41E-01  |
| ENKE                         | 2.43E +04  | 4.72E +02  | 4.32E +05 |
| ENDS                         | 9.62E +07  | 5.89E +03  | 6.98E +09 |
| TEMP                         | 7.15E +01  | 6.85E +01  | 7.37E +01 |

| <b>Mass Flow Rate Summary</b>      |
|------------------------------------|
| Total Mass Flow In = 0.31395E-02   |
| Total Mass Flow Out = -0.31392E-02 |
| ΔMass  = 3.E-07                    |

Table D.4: 12-Degree CFD Results Summary

| <b>Fluid Convergence Monitors</b> |          |          |          |          |          |
|-----------------------------------|----------|----------|----------|----------|----------|
| Vx                                | Vy       | PRES     | ENKE     | ENDS     | TEMP     |
| 9.41E-10                          | 4.42E-10 | 9.96E-09 | 5.79E-09 | 5.98E-09 | 6.30E-12 |

| <b>Fluid Results Summary</b> |            |            |           |
|------------------------------|------------|------------|-----------|
| Variable                     | Average    | Minimum    | Maximum   |
| Vx                           | 1.83E +03  | -4.92E +02 | 3.21E +03 |
| Vy                           | -2.00E +01 | -5.76E +02 | 2.96E +03 |
| PRES                         | -3.06E-02  | -7.46E-01  | 2.39E-01  |
| ENKE                         | 3.60E +04  | 4.79E +02  | 6.55E +05 |
| ENDS                         | 1.41E +08  | 5.89E +03  | 1.25E +10 |
| TEMP                         | 7.15E +01  | 6.63E +01  | 7.37E +01 |

| <b>Mass Flow Rate Summary</b>      |
|------------------------------------|
| Total Mass Flow In = 0.31400E-02   |
| Total Mass Flow Out = -0.31400E-02 |
| ΔMass  = 0.E-07                    |

Table D.5: 16-Degree CFD Results Summary

| <b>Fluid Convergence Monitors</b> |          |          |          |          |          |
|-----------------------------------|----------|----------|----------|----------|----------|
| Vx                                | Vy       | PRES     | ENKE     | ENDS     | TEMP     |
| 7.55E-07                          | 3.08E-07 | 1.04E-06 | 3.54E-06 | 1.06E-05 | 4.45E-09 |

| <b>Fluid Results Summary</b> |            |            |           |
|------------------------------|------------|------------|-----------|
| Variable                     | Average    | Minimum    | Maximum   |
| Vx                           | 1.74E +03  | -6.65E +02 | 3.55E +03 |
| Vy                           | -2.55E +01 | -6.28E +02 | 3.59E +03 |
| PRES                         | -3.73E-02  | -1.08E +00 | 2.41E-01  |
| ENKE                         | 4.96E +04  | 4.85E +02  | 8.83E +05 |
| ENDS                         | 1.96E +08  | 6.03E +03  | 1.87E +10 |
| TEMP                         | 7.15E +01  | 6.41E +01  | 7.37E +01 |

| <b>Mass Flow Summary</b>           |
|------------------------------------|
| Total Mass Flow In = 0.31409E-02   |
| Total Mass Flow Out = -0.31409E-02 |
| ΔMass  = 0.E-7                     |

Table D.6: 20-Degree CFD Results Summary

| <b>Fluid Convergence Monitors</b> |          |          |          |          |          |
|-----------------------------------|----------|----------|----------|----------|----------|
| Vx                                | Vy       | PRES     | ENKE     | ENDS     | TEMP     |
| 4.11E-05                          | 1.83E-05 | 3.17E-04 | 1.86E-04 | 2.02E-04 | 2.25E-07 |

| <b>Fluid Results Summary</b> |            |            |           |
|------------------------------|------------|------------|-----------|
| Variable                     | Average    | Minimum    | Maximum   |
| Vx                           | 1.68E +03  | -7.16E +02 | 3.71E +03 |
| Vy                           | -2.03E +01 | -7.11E +02 | 3.85E +03 |
| PRES                         | -4.32E-02  | -1.26E +00 | 2.44E-01  |
| ENKE                         | 5.77E +04  | 4.94E +02  | 1.00E +06 |
| ENDS                         | 2.27E +08  | 6.23E +03  | 2.21E +10 |
| TEMP                         | 7.16E +01  | 6.29E +01  | 7.37E +01 |

| <b>Mass Flow Summary</b>           |
|------------------------------------|
| Total Mass Flow In = 0.31419E-02   |
| Total Mass Flow Out = -0.31419E-02 |
| ΔMass  = 0.E-7                     |

## APPENDIX E: STRUCTURAL RESULTS

---

### REACTION SOLUTIONS

Table E.1: 0-Degree Reaction Solution

| Location ( <i>in</i> ) | FX ( <i>lbf</i> ) | FY ( <i>lbf</i> ) | MZ ( <i>lbf·in</i> ) |
|------------------------|-------------------|-------------------|----------------------|
| (0, 0)                 | 0.00000           | -4.6036           | -32.505              |
| (42, 0)                | 0.00000           | -4.6696           | 32.744               |
| (0, 14.5)              | 0.00000           | 4.7193            | 32.746               |
| (42, 14.5)             | 0.00000           | 4.6494            | -32.489              |

Table E.2: 4-Degree Reaction Solution

| Location ( <i>in</i> ) | FX ( <i>lbf</i> ) | FY ( <i>lbf</i> ) | MZ ( <i>lbf·in</i> ) |
|------------------------|-------------------|-------------------|----------------------|
| (0, 0)                 | 0.00000           | -4.5218           | -31.834              |
| (42, 0)                | 0.00000           | -4.6183           | 32.206               |
| (0, 14.5)              | 0.00000           | 4.6428            | 31.990               |
| (42, 14.5)             | 0.00000           | 4.5749            | -31.769              |

Table E.3: 8-Degree Reaction Solution

| Location ( <i>in</i> ) | FX ( <i>lbf</i> ) | FY ( <i>lbf</i> ) | MZ ( <i>lbf·in</i> ) |
|------------------------|-------------------|-------------------|----------------------|
| (0, 0)                 | 0.00000           | -4.4381           | -31.136              |
| (42, 0)                | 0.00000           | -4.5603           | 31.629               |
| (0, 14.5)              | 0.00000           | 4.5803            | 31.367               |
| (42, 14.5)             | 0.00000           | 4.5137            | -31.169              |

Table E.4: 12-Degree Reaction Solution

| Location ( <i>in</i> ) | FX ( <i>lbf</i> ) | FY ( <i>lbf</i> ) | MZ ( <i>lbf·in</i> ) |
|------------------------|-------------------|-------------------|----------------------|
| (0, 0)                 | 0.00000           | -4.3513           | -30.473              |
| (42, 0)                | 0.00000           | -4.5126           | 31.141               |
| (0, 14.5)              | 0.00000           | 4.5399            | 30.881               |
| (42, 14.5)             | 0.00000           | 4.4579            | -30.632              |

Table E.5: 16-Degree Reaction Solution

| <b>Location (in)</b> | <b>FX (lbf)</b> | <b>FY (lbf)</b> | <b>MZ (lbf·in)</b> |
|----------------------|-----------------|-----------------|--------------------|
| (0, 0)               | 0.00000         | -4.2715         | -29.967            |
| (42, 0)              | 0.00000         | -4.4928         | 30.901             |
| (0, 14.5)            | 0.00000         | 4.5428          | 30.693             |
| (42, 14.5)           | 0.00000         | 4.4187          | -30.278            |

Table E.6: 20-Degree Reaction Solution

| <b>Location (in)</b> | <b>FX (lbf)</b> | <b>FY (lbf)</b> | <b>MZ (lbf·in)</b> |
|----------------------|-----------------|-----------------|--------------------|
| (0, 0)               | 0.00000         | -4.2210         | -29.819            |
| (42, 0)              | 0.00000         | -4.5241         | 31.124             |
| (0, 14.5)            | 0.00000         | 4.6025          | 30.925             |
| (42, 14.5)           | 0.00000         | 4.3979          | -30.148            |

## DISPLACEMENT PLOTS

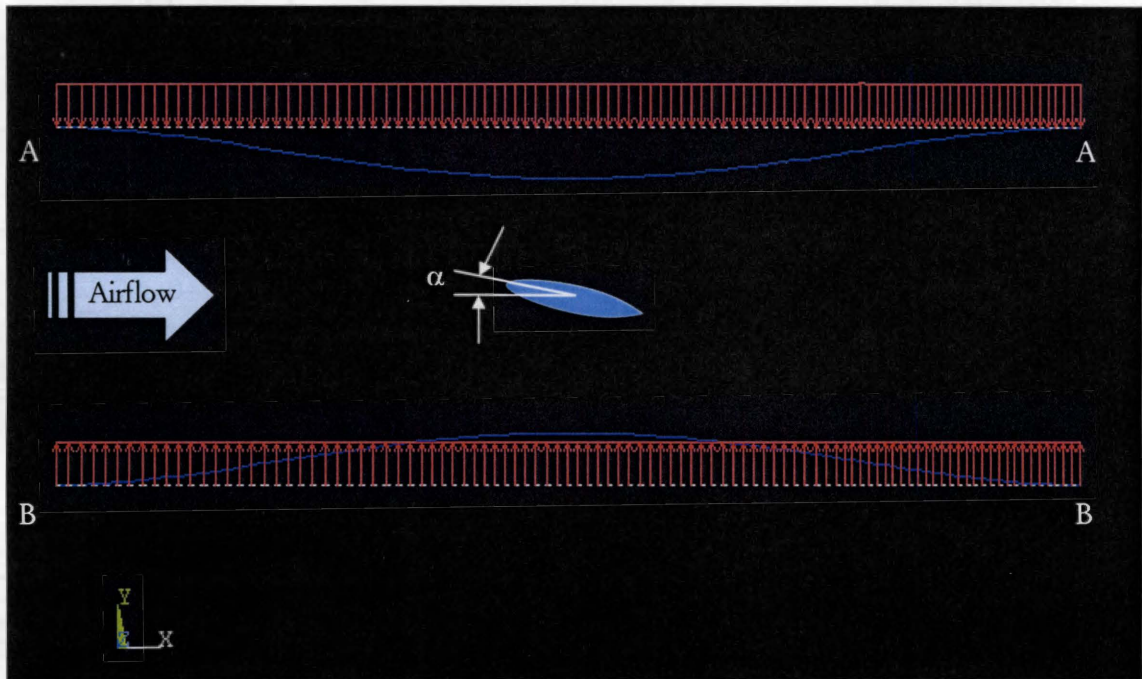


Figure E.1: Combination Predicted Pressure and Displacement  
(compilation of multiple images, both pre- and post-processing)



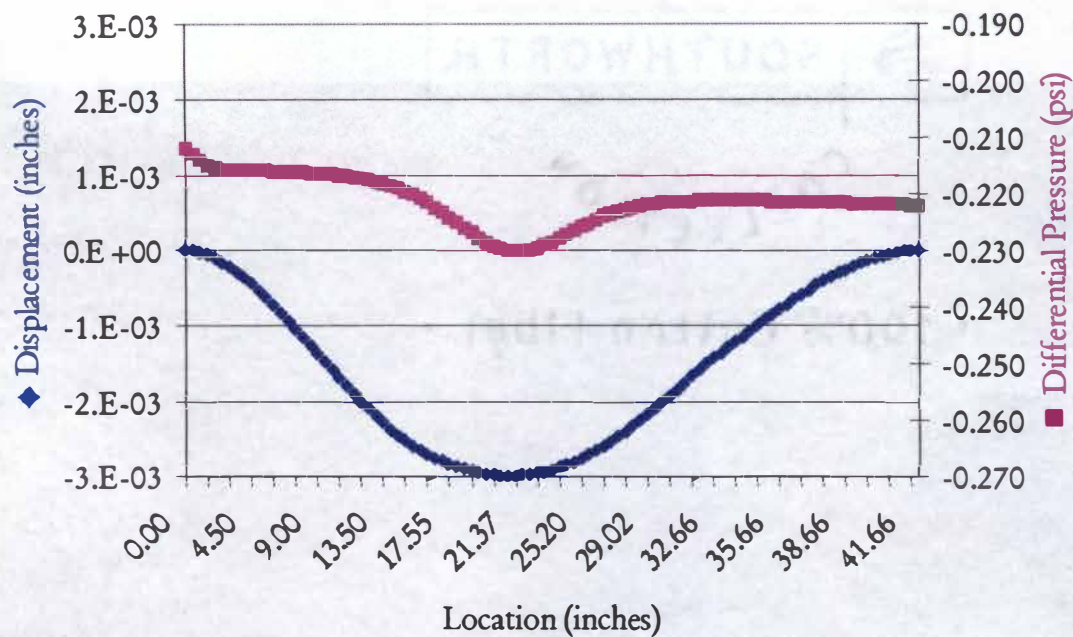


Figure E.2: 0-Degree, Wall AA, Predicted Displacement and Pressure vs. Wall Length  
 (Max Displacement =  $-2.99E-03$  in, Min Pressure =  $-0.230$  psi)

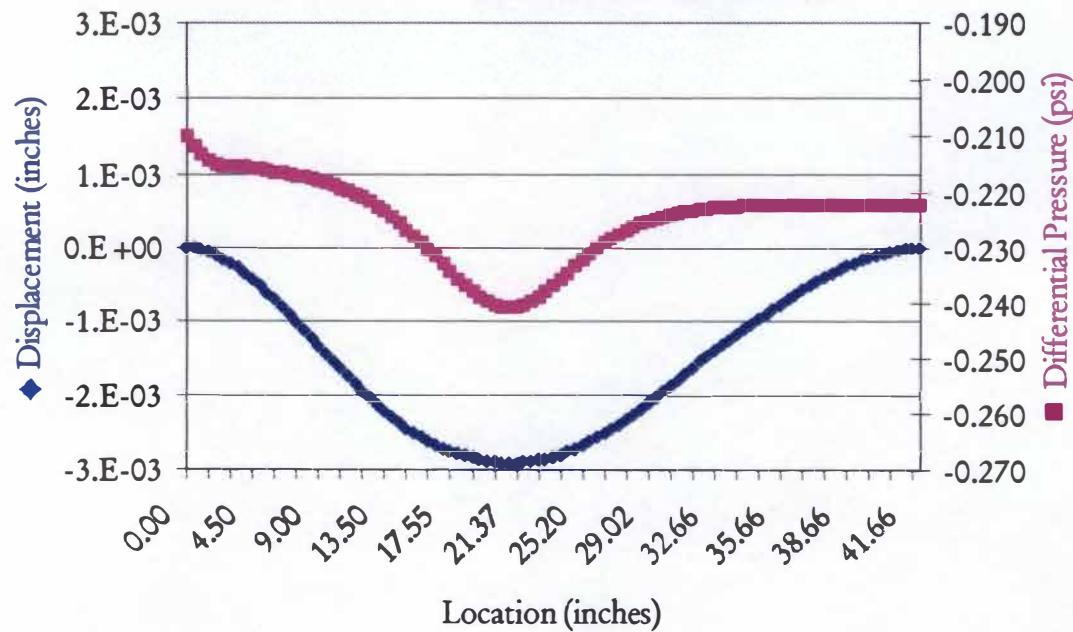


Figure E.3: 4-Degree, Wall AA, Predicted Displacement and Pressure vs. Wall Length  
 (Max Displacement =  $-2.91E-03$  in, Min Pressure =  $-0.241$  psi)

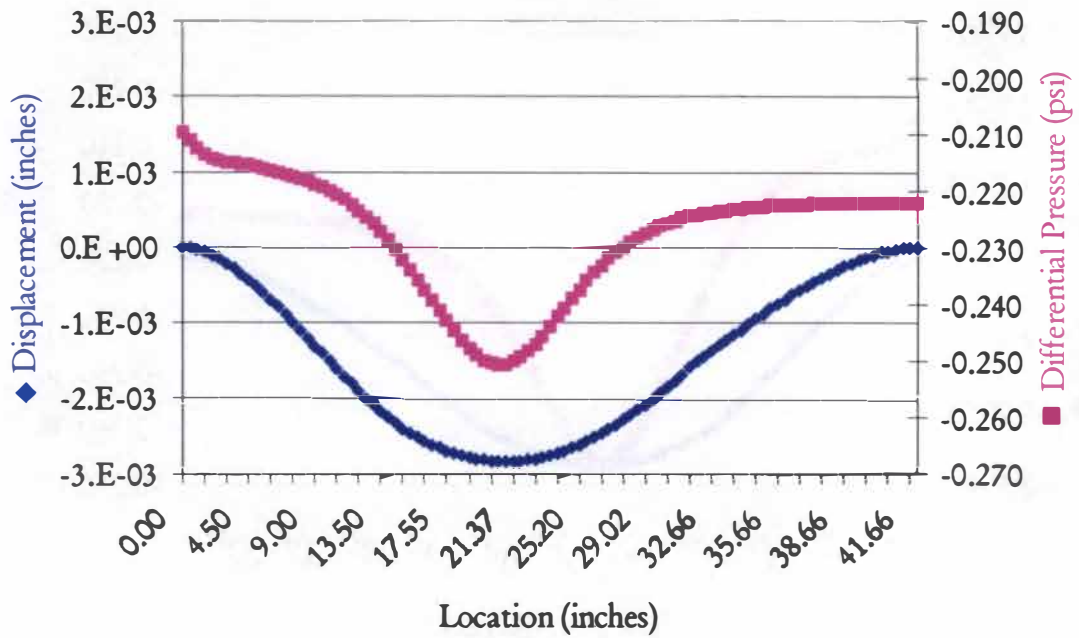


Figure E.4: 8-Degree, Wall AA, Predicted Displacement and Pressure vs. Wall Length  
 (Max Displacement =  $-2.84E-03$  in, Min Pressure =  $-0.251$  psi)

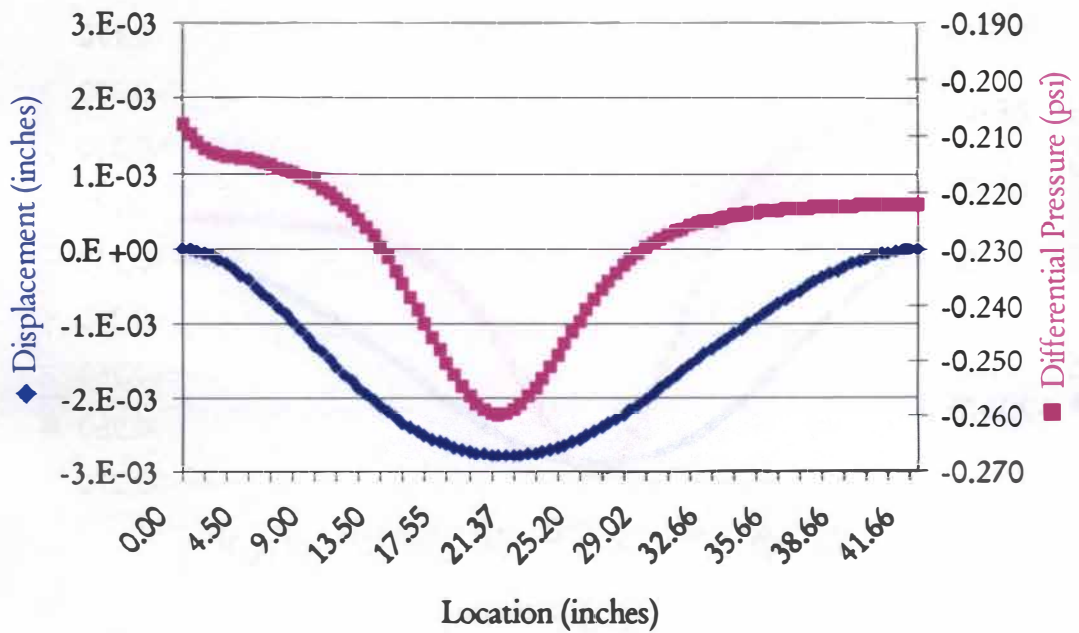


Figure E.5: 12-Degree, Wall AA, Predicted Displacement and Pressure vs. Wall Length  
 (Max Displacement =  $-2.78E-03$  in, Min Pressure =  $-0.260$  psi)

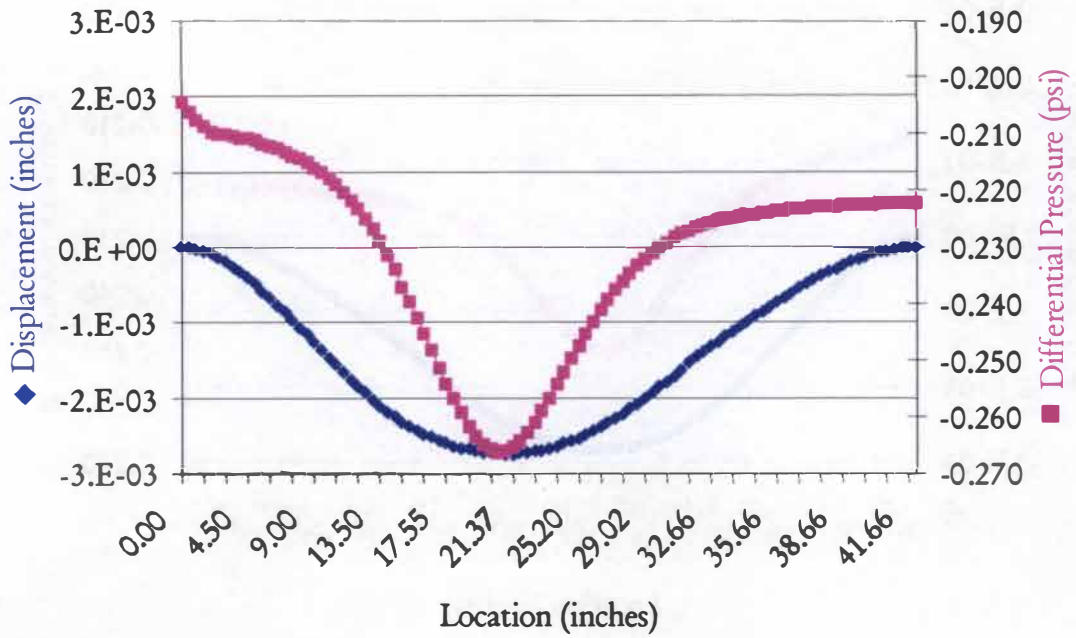


Figure E.6: 16-Degree, Wall AA, Predicted Displacement and Pressure vs. Wall Length  
 (Max Displacement =  $-2.75E-03$  in, Min Pressure =  $-0.266$  psi)

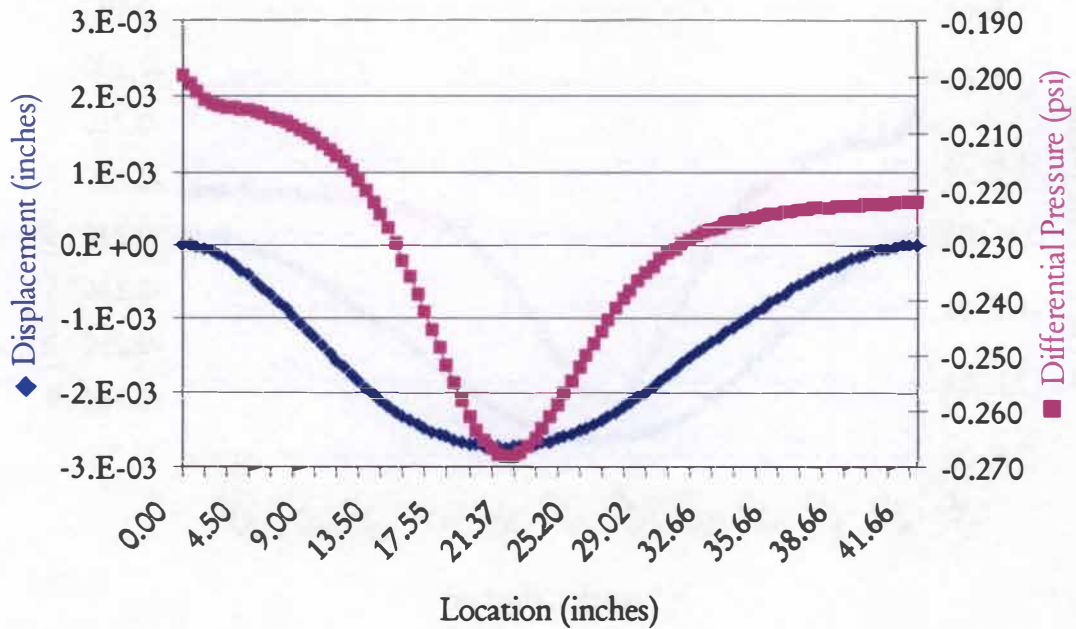


Figure E.7: 20-Degree, Wall AA, Predicted Displacement and Pressure vs. Wall Length  
 (Max Displacement =  $-2.75E-03$  in, Min Pressure =  $-0.268$  psi)

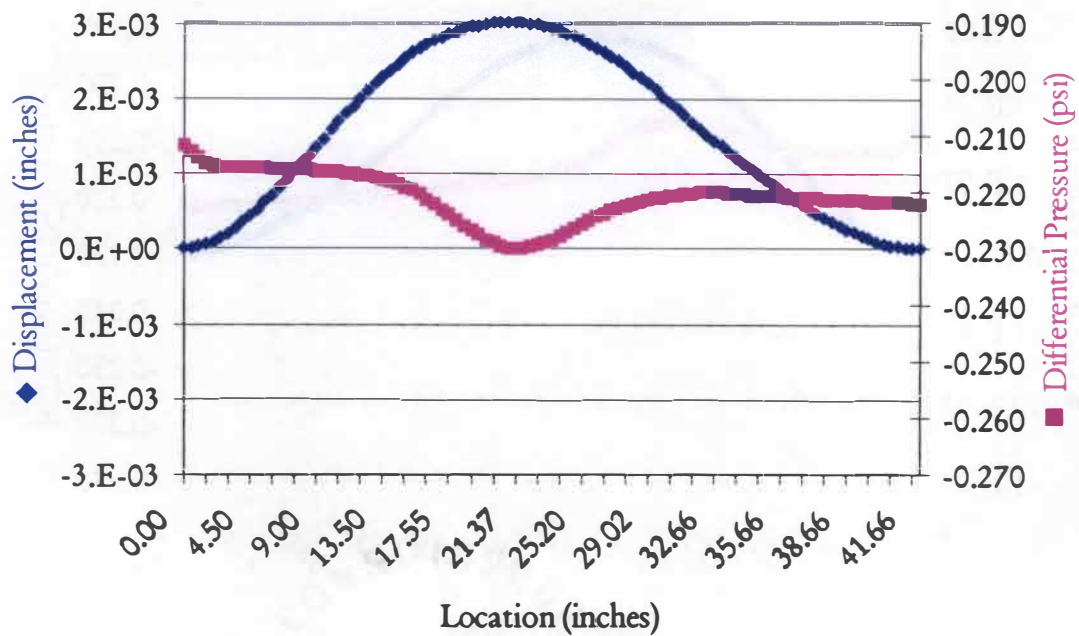


Figure E.8: 0-Degree, Wall BB, Predicted Displacement and Pressure vs. Wall Length  
 (Max Displacement = 3.02E-03 in, Max Pressure = -0.212 psi)

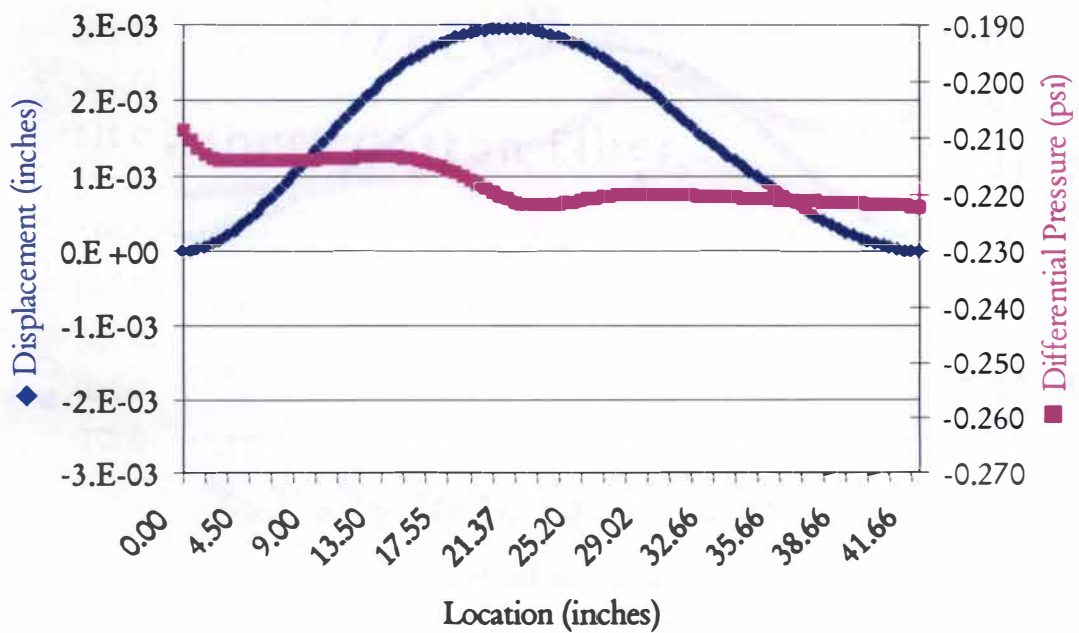


Figure E.9: 4-Degree, Wall BB, Predicted Displacement and Pressure vs. Wall Length  
 (Max Displacement = 2.95E-03 in, Max Pressure = -0.209 psi)

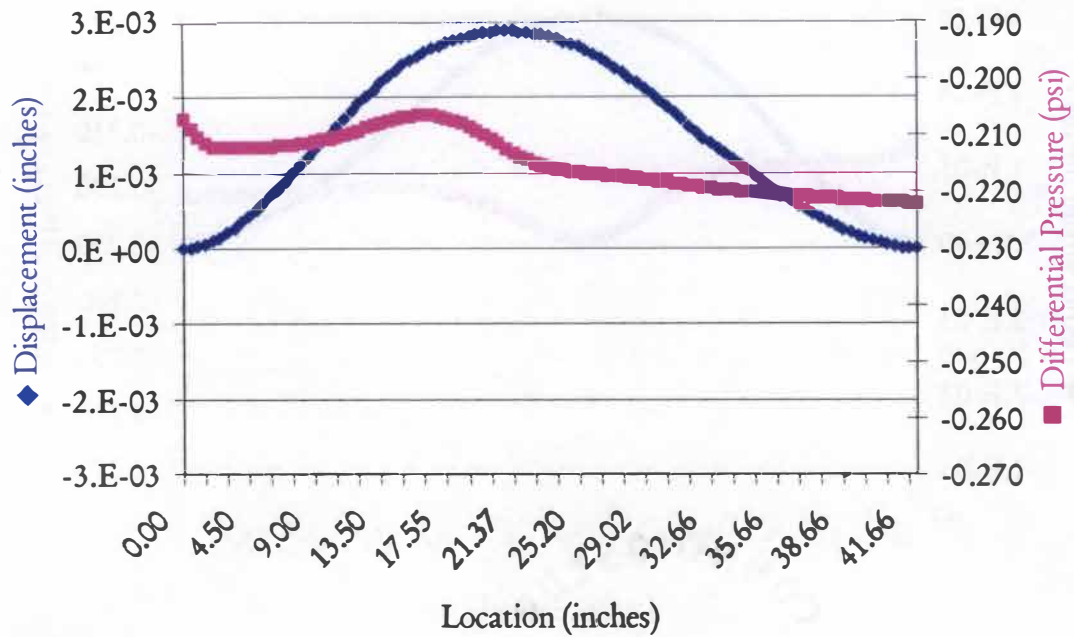


Figure E.10: 8-Degree, Wall BB, Predicted Displacement and Pressure vs. Wall Length  
 (Max Displacement = 2.89E-03 in, Max Pressure = -0.206 psi)

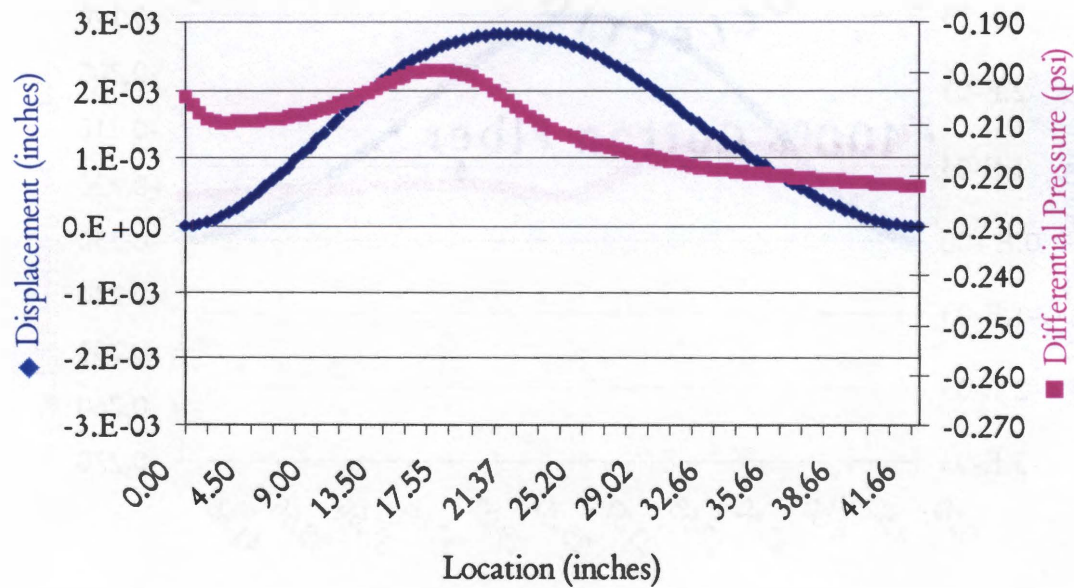


Figure E.11: 12-Degree, Wall BB, Predicted Displacement and Pressure vs. Wall Length  
 (Max Displacement = 2.83E-03 in, Max Pressure = -0.199 psi)

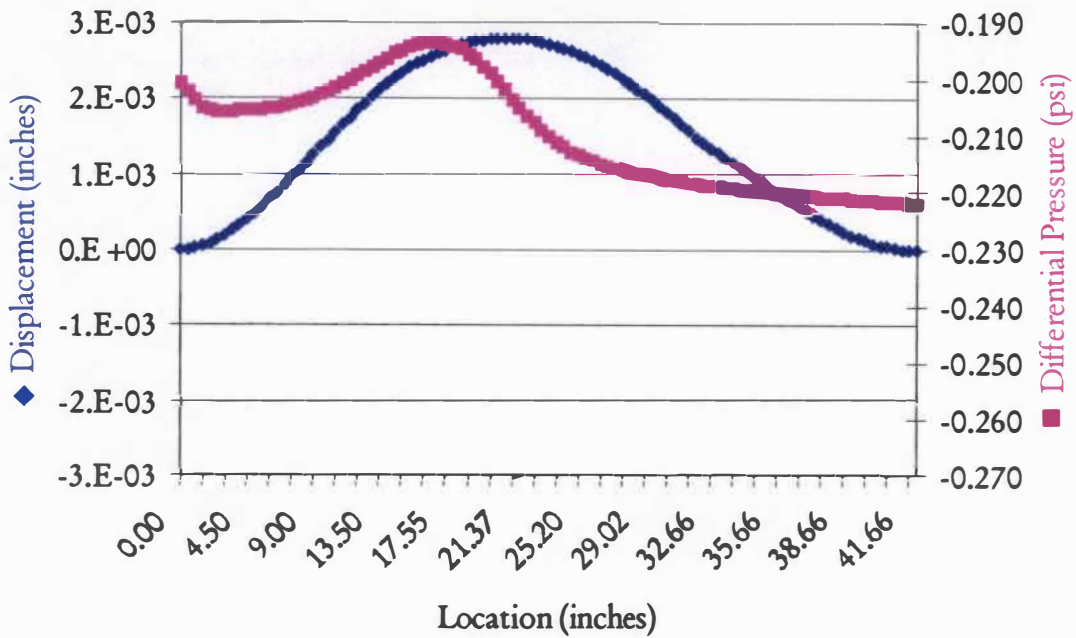


Figure E.12: 16-Degree, Wall BB, Predicted Displacement and Pressure vs. Wall Length  
 (Max Displacement = 2.79E-03 in, Max Pressure = -0.194 psi)

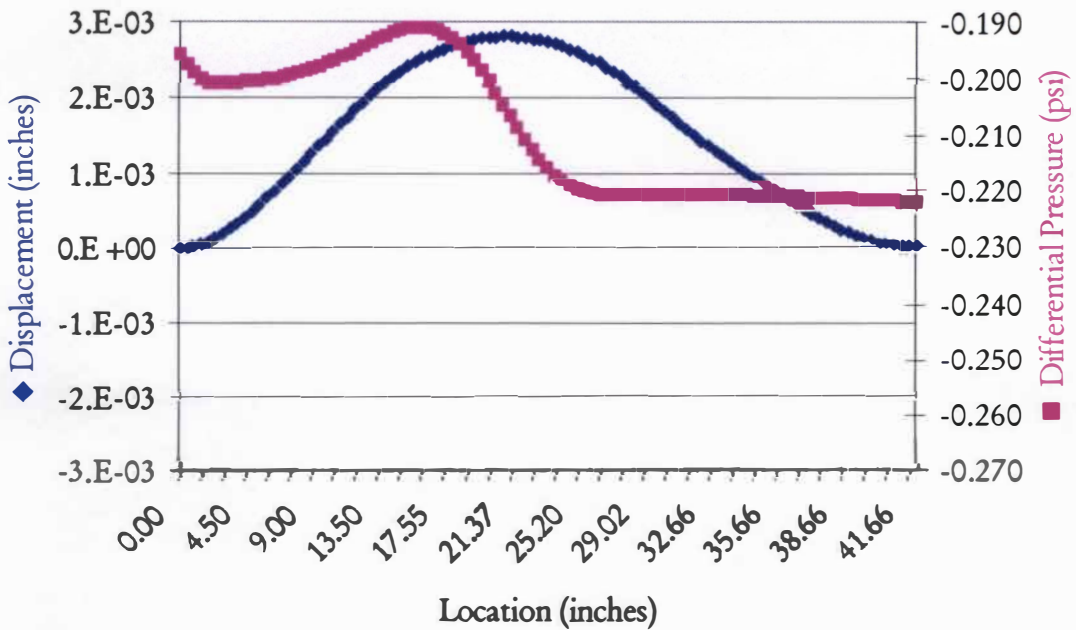


Figure E.13: 20-Degree, Wall BB, Predicted Displacement and Pressure vs. Wall Length  
 (Max Displacement = 2.80E-03 in, Max Pressure = -0.191 psi)

APPENDIX F: EXPERIMENTAL RESULTS

Table F.1: Experimental Test Conditions

| Property                         | Value                 |
|----------------------------------|-----------------------|
| Free Stream Velocity, $U$        | $0.15Ma, 2038.4m/sec$ |
| Atmospheric Pressure, $p_{ref}$  | $14.20164psi$         |
| Reference Temperature, $T_{ref}$ | $73.7113^{\circ}F$    |
| Oscillation Frequency, $f$       | $10Hz$                |
| Oscillation Magnitude            | $20\ degrees$         |

Table F.2: Experimental and Numerical Absolute Pressure Comparison

| Pitch Angle (degrees) | Experimental Pressure with Error (psi) | Numerical Pressure (psi) |
|-----------------------|--|--------------------------|
| <b>Ps-5, Wall AA</b>  |  |                          |
| 0                     | $13.9371 \pm 0.0052$                   | 13.9717                  |
| 4                     | $13.9419 \pm 0.0045$                   | 13.9608                  |
| 8                     | $13.9386 \pm 0.0053$                   | 13.9511                  |
| 12                    | $13.9359 \pm 0.0065$                   | 13.9419                  |
| 16                    | $13.9177 \pm 0.0062$                   | 13.9355                  |
| <b>Ps-10, Wall AA</b> |  |                          |
| 0                     | $13.9339 \pm 0.0044$                   | 13.9755                  |
| 4                     | $13.9379 \pm 0.0052$                   | 13.9689                  |
| 8                     | $13.9344 \pm 0.0027$                   | 13.9635                  |
| 12                    | $13.9341 \pm 0.0039$                   | 13.9580                  |
| 16                    | $13.9254 \pm 0.0053$                   | 13.9531                  |
| <b>Ps-5, Wall BB</b>  |  |                          |
| 0                     | $13.9371 \pm 0.0052$                   | 13.9718                  |
| 4                     | $13.9498 \pm 0.0057$                   | 13.9808                  |
| 8                     | $13.9368 \pm 0.0061$                   | 13.9893                  |
| 12                    | $13.9595 \pm 0.0045$                   | 13.9962                  |
| 16                    | $13.9590 \pm 0.0023$                   | 13.9997                  |
| <b>Ps-10, Wall BB</b> |  |                          |
| 0                     | $13.9339 \pm 0.0044$                   | 13.9756                  |
| 4                     | $13.9340 \pm 0.0066$                   | 13.9805                  |
| 8                     | $13.9315 \pm 0.0047$                   | 13.9852                  |
| 12                    | $13.9328 \pm 0.0074$                   | 13.9887                  |
| 16                    | $13.9307 \pm 0.0053$                   | 13.9886                  |

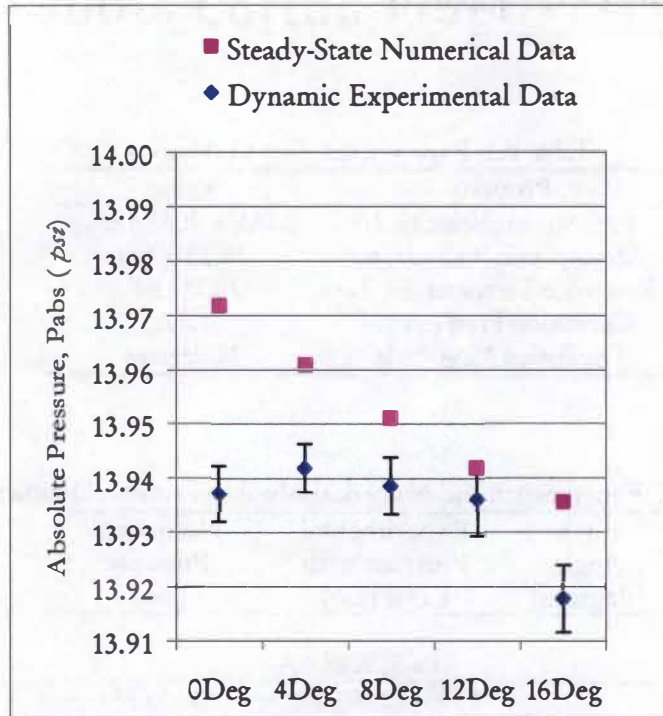


Figure F.1: Wall AA, Ps-5,  $p_{abs}$  vs. Pitch Angle

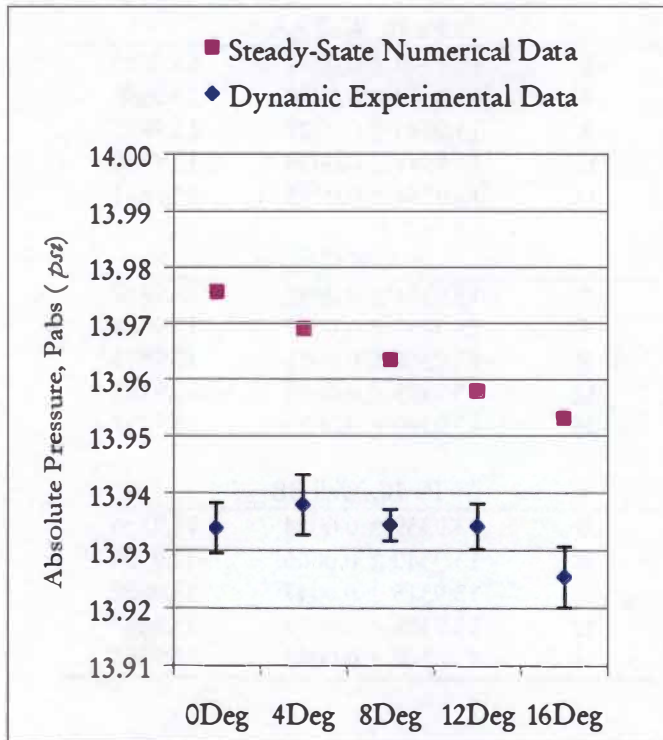


Figure F.2: Wall AA, Ps-10,  $p_{abs}$  vs. Pitch Angle



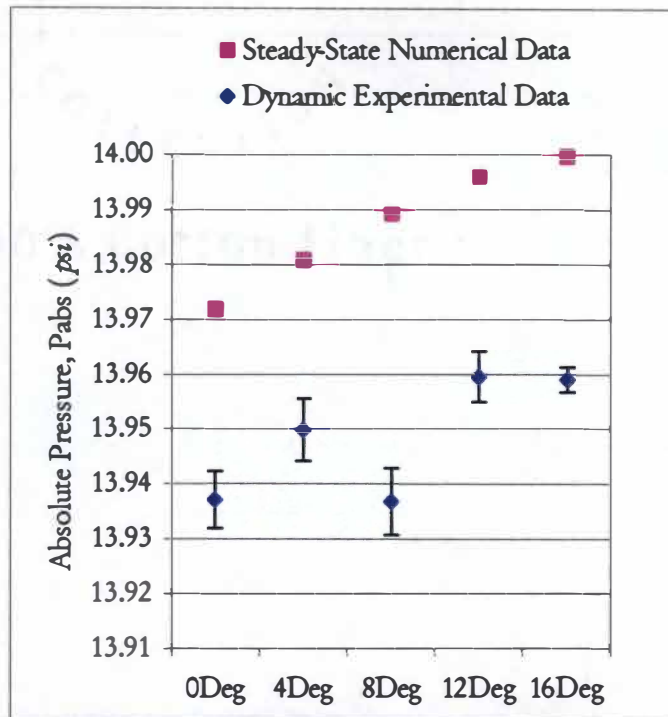


Figure F.3: Wall BB, Ps-5,  $p_{abs}$  vs. Pitch Angle

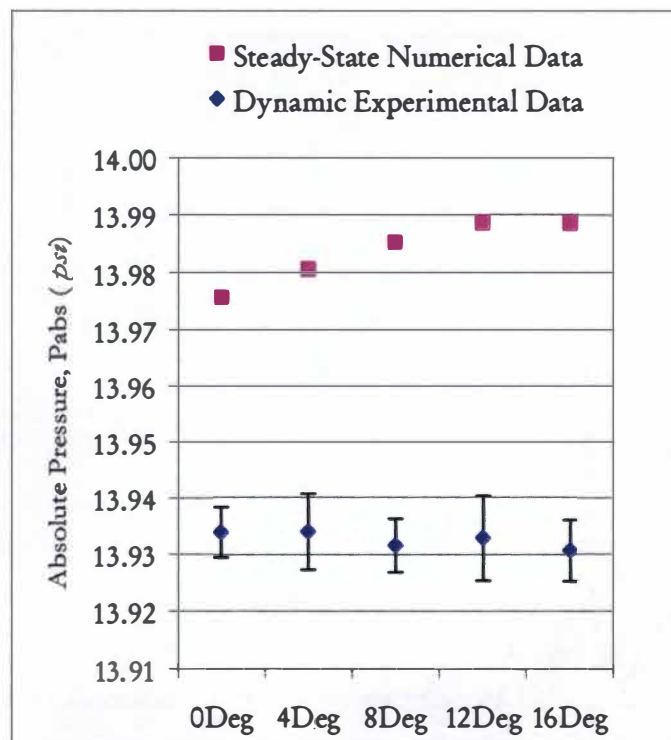


Figure F.4: Wall BB, Ps-10,  $p_{abs}$  vs. Pitch Angle

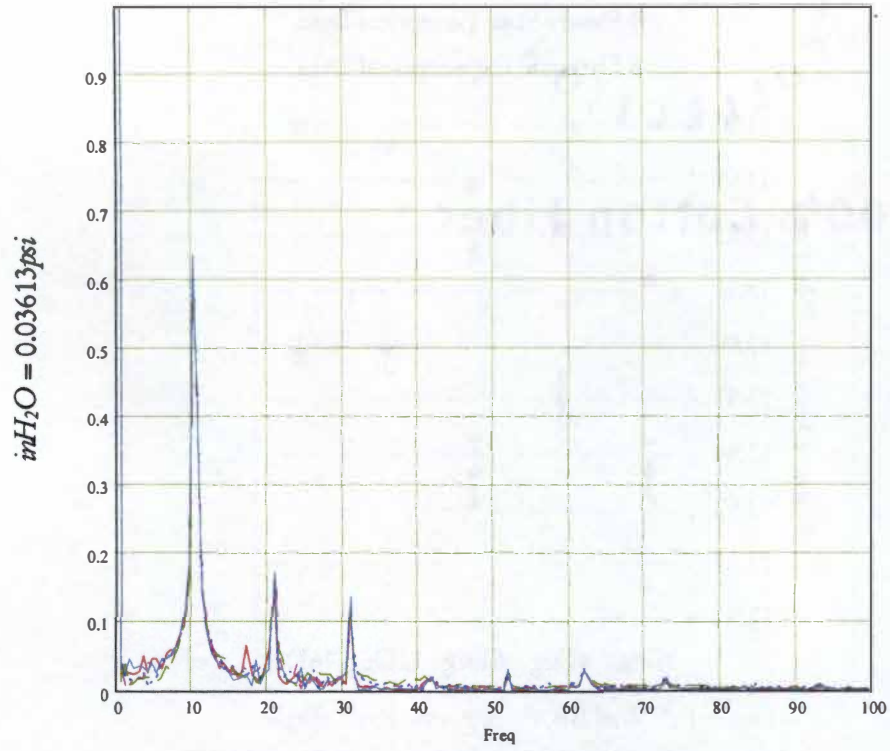


Figure F.5: Spectral Plot of Static Pressure at Ps-5

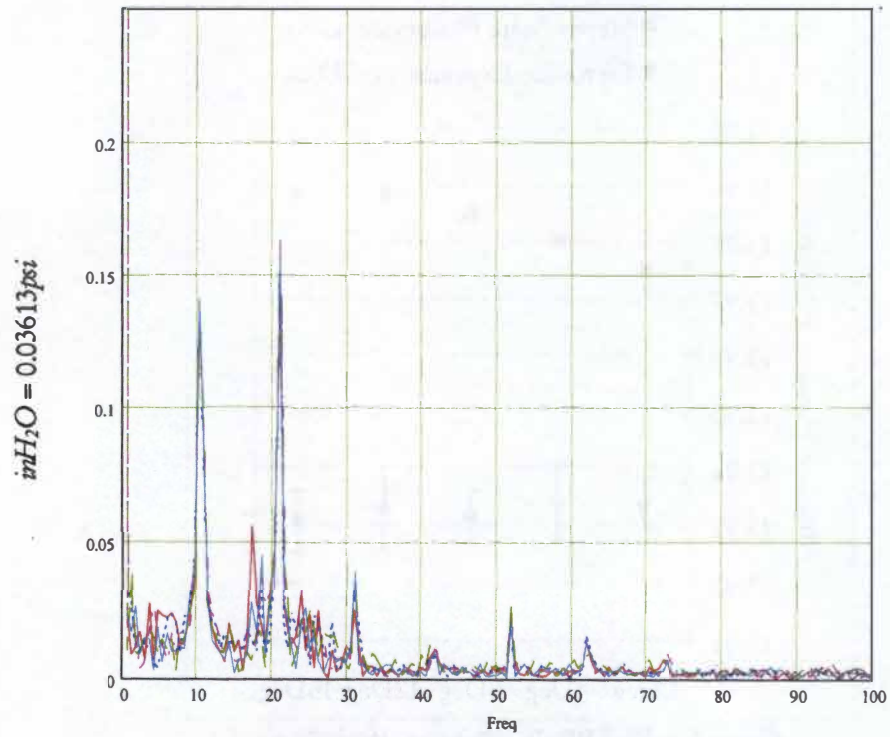


Figure F.6: Spectral Plot of Static Pressure at Ps-10

## VITA

---

Nicholas Martin Holland was born on 9 May 1978 in Birmingham, Alabama. He attended public schools in Jefferson and Shelby Counties. He was active in band, wrestling, and Boy Scouting. Nicholas earned the rank of Eagle Scout in 1994. He graduated Pelham High School in the spring of 1996 with an advanced diploma.

Nicholas studied Mechanical Engineering at Mississippi State University where he was active in the Reserve Officer Training Corps, various professional societies including ASME, and the University Christian Student Center. He graduated summa cum laude with a Bachelor's of Science Degree in the spring of 2001. Nicholas married the former Kristi Dianne Shearer in May 2000.

After commissioning in the United States Air Force, Nicholas served at the Arnold Engineering Development Center, Arnold Air Force Base, and studied Aerospace Engineering at the University of Tennessee Space Institute. He and his wife live in Tullahoma, Tennessee. Since moving to Tennessee, Nicholas has been involved with the Company Grade Officers Council, Special Olympics, and his local church congregation.